UNIVERSITY OF SOUTHAMPTON

FACULTY OF PHYSICAL AND APPLIED SCIENCES

OPTOELECTRONICS RESEARCH CENTRE

Table-top XUV Nanoscope

by

James Andrew Grant-Jacob

Thesis for the degree of Doctor of Philosophy

March 2011

UNIVERSITY OF SOUTHAMPTON

ABSTRACT

FACULTY OF PHYSICAL AND APPLIED SCIENCES
OPTOELECTRONICS RESEARCH CENTRE

Doctor of Philosophy

Table-top XUV Nanoscope

by James Andrew Grant-Jacob

This thesis documents the development of a table-top extreme-ultraviolet (XUV) nanoscope suitable for coherent diffractive imaging (CDI). Intense spatially coherent ultrashort XUV and X-ray pulses are desired for nanoscale biological and material imaging. Such radiation can be produced via high harmonic generation (HHG) by focusing a highly intense ultrashort laser pulse into gas. In order to obtain high flux XUV radiation suitable for CDI, various generation conditions are explored. By observing the fluorescence from an argon gas jet to position the laser focus into different regions within the jet, a fourfold variation in XUV yield is achieved. Maximum output flux is obtained for the 19^{th} harmonic when the laser is focused into the Mach disc of the jet. To further increase the XUV flux, HHG from a larger generation region (an argon-filled pipe) is also demonstrated. The most intense harmonic is nearly fifty times more intense and 10 nm shorter in wavelength compared with the most intense harmonic generated from an argon gas jet. Position for maximum generated XUV flux occurs when the laser focus is positioned after the pipe. In addition, a reduction in the number of harmonics in the output spectrum is also achieved by positioning the laser focus after the pipe. Using the high harmonics generated from the argon-filled pipe for XUV scattering, CDI is used to reveal the nanoscale structure of micron-sized objects. This thesis demonstrates the imaging of a 5 μm pinhole, a 7.5 μm FIB (focused ion beam) sample and a biological sample using the table-top XUV nanoscope. A maximum reconstructed object resolution of ~ 300 nm is achieved. The work described here will aid in the development of a table-top nanoscope capable of routine imaging.

Contents

List of Figures

List of Tables

DECLARATION OF AUTHORSHIP

I, James Andrew Grant-Jacob, declare that the thesis entitled *Table-top XUV Nanoscope* and the work presented in it are my own. I confirm that:

- this work was done wholly or mainly while in candidature for a research degree at this University;
- where any part of this thesis has previously been submitted for a degree or any other qualification at this University or any other institution, this has been clearly stated;
- where I have consulted the published work of others, this is always clearly attributed;
- where I have quoted from the work of others, the source is always given. With the exception of such quotations, this thesis is entirely my own work;
- I have acknowledged all main sources of help;
- where the thesis is based on work done by myself jointly with others, I have made clear exactly what was done by others and what I have contributed myself;
- parts of this work have been published as:
- J. Grant-Jacob, B. Mills, T. J. Butcher, R. T. Chapman, W. S. Brocklesby and J. G. Frey. *Gas jet structure influence on high harmonic generation.* Optics Express, **19**, 9801-9806 (2011).
- J. Grant-Jacob, B. Mills, T. J. Butcher, R. T. Chapman, W. S. Brocklesby and J. G. Frey. *Imaging an Argon Gas Jet Using a Femtosecond Laser*. In preparation.

Signed: …….

Date: …….

ACKNOWLEDGEMENTS

I would like to express my sincerest gratitude to all those who helped me complete my PhD.

1 Introduction

1.1 Motivation

The visualization of structures smaller than those visible with the human eye has been a motivating force in science for centuries. The optical microscope was the first microscope used to study such small objects. It was developed in the Netherlands in 1590 by Zaccharias Janssen and Hans Janssen, and further developments were made by Galileo Galilei who created a compound microscope in 1624. From Robert Hooke's 'Micrographia' on insects, plants and minerals, to Marcello Malpighi's work on kidneys and Antoni van Leeuwenhoek's discovery of red blood cells, microscopy is a technique that has significantly advanced science.

Optical microscopes have a resolution that is limited by diffraction to several hundred nanometres. Many materials and biological systems such as ceramics, proteins and structures in diatoms have important structures on length scales much shorter than that observable with visible light.

The resolution of optical microscopy can be extended through super resolution techniques such as scanning near-field optical microscopy (SNOM) [1], which involves the use of evanescent waves to obtain resolution beyond the diffraction limit. However, SNOM requires long scan times to obtain high resolution images and is limited to studying surfaces. Other techniques include stimulated emission depletion (STED) [2] and photo-activated localization microscopy (PALM) [3]. These techniques can achieve resolutions at one tenth of that obtained with ordinary microscopes but are complicated and most require fluorescent molecules within the sample for image contrast.

Current techniques available to study nanoscale objects without using visible light include scanning electron microscopes (SEMs) and transmission electron microscopes (TEMs) [4]. These electron-beam techniques can provide nanoscale resolution due to the short de Broglie wavelength of the electrons. Since their invention in the 1930s, electron microscopes have enabled imaging of an array of nanostructures in materials and biology. Although well-established, TEMs are restricted to thin samples due to the limited penetration of electrons and SEMs are generally limited to coated samples.

A new imaging technology similar to an SEM is a scanning helium ion

microscope (SHIM) [5]. Instead of an electron beam, a helium ion beam is used as the illumination radiation. SHIMs offer the ability to obtain sub-nanometre resolution images. However, SHIMs, just like SEMs, are limited to surface imaging.

Similarly, there are a number of other scanning probe techniques such as scanning tunnelling microscopy (STM) [6] and atomic force microscopy (AFM) [7]. These techniques also offer high resolution capabilities, but again they only image the surface of samples and sufficient sample preparation is needed before imaging.

X-ray crystallography is an imaging method that uses short wavelength light to obtain high resolution images [8,9]. It is already widely used in chemistry and biochemistry to determine the structures of a variety of molecules, including inorganic compounds and DNA. Although samples such as proteins have been studied using this diffraction technique [10], the main limitation with using such probes is the need to crystallise samples. The shape of the sample is often distorted during crystallisation and there are many samples that cannot be crystallised due to their tendency to aggregate [11].

A method of nanoscale imaging that is not limited in the same way as the techniques documented above would be beneficial to science.

1.2 An Alternative: an XUV/X-ray Nanoscope

Extreme-ultraviolet (XUV) (10-120 nm) or X-ray (0.01-10 nm) light enables higher resolution imaging of a variety of objects compared to visible light due to their shorter wavelength and greater material penetration. Indeed, X-ray microscopy uses X-rays instead of visible light to image nanoscale objects [12]. Due to the poor refraction and high absorption in most materials of X-rays, zone plates are commonly used to focus the X-rays [13]. Although many objects have been imaged using X-ray microscopy, zone plates reduce the flux of the incident radiation and have limited resolution.

Using short-pulsed spatially coherent XUV or X-ray light to scatter off samples is an alternative nanoscale imaging technique that allows high penetration and high resolution, as well as removing the need to use zone plates and crystallised samples. In order to obtain as high resolution images as possible, it is necessary to have high flux. However, this can cause ionization of inner electrons from atoms within a molecule. The repulsion between positively charged ions can cause a Coulomb explosion which results in irreversible sample damage [14]. The timescale of this damage is approximately 15 femtoseconds [15].

Neutze *et al.* [15] predicted that by using femtosecond high intensity X-ray pulses to scatter off non-crystalline samples before they are destroyed, it is possible to determine the corresponding structure from their recorded scattering image. This has been demonstrated experimentally by Chapman *et al.* [16]. As such, by extending this technique with the use of

radiation with a wavelength between 2.33 nm and 4.37 nm (the 'water-window' where the carbon in biological objects absorbs radiation strongly but the water does not), high contrast biological images are potentially producible.

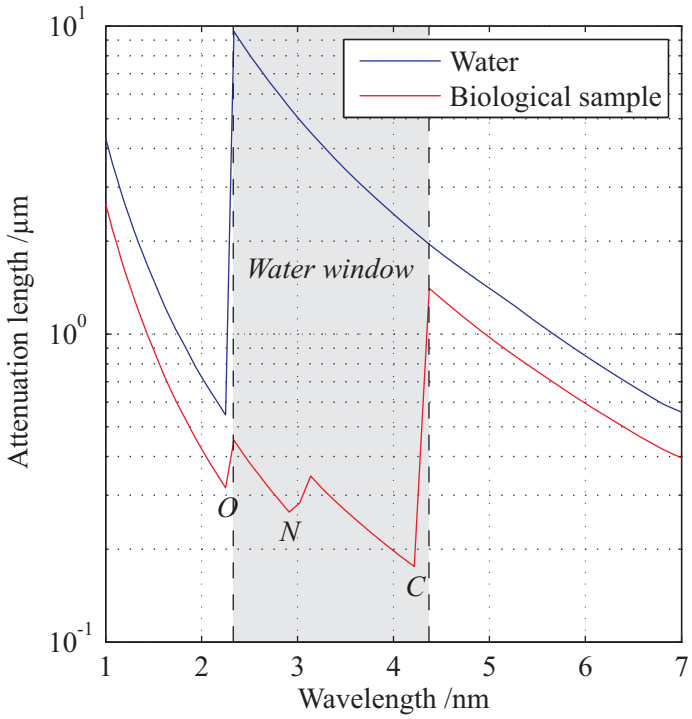

Figure 1.1: Absorption in the water-window. The symbols represent the absorption edges of the corresponding elements that are present in a simple biological sample. The data are taken from reference [17].

By using an XUV or X-ray pulse that is temporally short, a scattering image of nanostructures can be recorded on a camera before the sample is irreversibly damaged or destroyed [18]. Although a camera does not record any phase information, if the scattering image can be reliably inverted by computation, then XUV and X-ray scattering can be used to reveal the structure of nanoscale objects. Coherent diffractive imaging (CDI) is a method that solves such a problem. The technique uses a phase retrieval algorithm originally devised by Gerchberg and Fienup to allow image reconstruction of a sample from the observed scattering pattern [19,20].

The development of a source of short pulsed high flux XUV or X-ray radiation, along with an appropriate imaging setup, could potentially enable high spatial resolution images of nanoscale objects to be obtained.

1.3 Current XUV and X-ray Sources

To date, various sources exist for the generation of XUV and X-ray radiation (see Table 1.1 for a summary of source parameters). These include plasma sources, free-electron lasers (FELs), synchrotrons and high harmonic sources; all having their own advantages and disadvantages, and all in some way using accelerated electrons in the conversion process. Laser and electric discharge generation of hot and dense plasma can emit incoherent XUV and X-ray radiation [21,22]. Such a technique is available on the table-top scale and imaging of micron-sized objects has already been demonstrated using this source [23]. However, the need to aperture the beam to achieve spatial coherence reduces flux and the picoseconds pulse lengths of the generated radiation are too long for single-shot imaging.

Another source of short wavelength generation is synchrotrons. Radiation from a synchrotron can have wavelengths ranging from 0.01 nm to 1 μm [24] and pulse lengths ranging from 300 femtosecond to picoseconds [25]. Synchrotron radiation sources have many applications in scientific research [26]. However, the long pulse lengths and the need to aperture the beam to obtain spatial coherence means such sources are currently not suitable for single-shot imaging. Furthermore, the cost and scale of synchrotrons severely limits their wide spread use.

	HHG source	**Flash FEL**	**LCLS**	**Diamond synchrotron**
Spatial coherence	*High*	*High*	*High*	*Low*
Footprint	*~ 5 m^2*	*~ 10,000 m^2*	*~ 2,000 km^2*	*~ 45,000 m^2*
Cost	*~ £3m*	*~ €120m*	*~ $315m*	*~ £260m*
Pulse length	*0.13-60 fs*	*10-50 fs*	*1-500 fs*	*~ 1 ps*
Wavelength	*2.7-60 nm*	*6.5-47 nm*	*0.12-2.2 nm*	*0.01-15 nm*

Table 1.1: Comparison of the specifications of currently available high harmonic generation sources, the FLASH FEL at DESY in Hamburg, the LCLS in Stanford University and the UK Diamond Light Source. Flash specifications from [27]. LCLS specifications from [28]. Diamond specifications from [29].

In FELs, an ultrashort electron pulse is accelerated by an electric field to gigaelectronvolt energies resulting in the emission of short wavelength light via undulator radiation. The FLASH (Free-electron LASer in Hamburg) experiment, reported the first demonstration of ultrashort and extremely intense soft-X-ray scattering (Chapman *et al.* [16]). At the time of writing this thesis, the source was able to produce radiation with pulse

lengths of order tens of femtoseconds and wavelengths between 6.5 nm and 47 nm. Another FEL, the Linac Coherent Light Source (LCLS) based in Stanford, is currently able to generate femtosecond pulses with wavelengths between 0.12 nm and 2.2 nm at a brightness ten orders greater than current synchrotron radiation [28]. The source is therefore ideal for CDI. However, as with synchrotrons, such sources are not widely available. A technology available on the scale of a table-top would add substantial benefits to the scientific community by offering a financially and more technologically accessible device.

A table-top method to produce ultrashort XUV and X-ray pulses is the direct conversion of a laser pulse into shorter wavelengths by a nonlinear process called high-harmonic generation (HHG) [30]. By focusing an ultrashort intense laser into atoms or ions, femtosecond XUV and X-ray radiation can be generated [31]. The spectral range and intensity of the generated harmonics can be varied [32,33]. In addition, the generated light has a high degree of spatial coherence, which is needed for scattering based imaging. Indeed, successful imaging of objects with a resolution of ~ 90 nm has recently been achieved with a high harmonic source [23].

As specified in Table 1.1, HHG is a high spatially coherent, financially viable, table-top alternative to large expensive accelerator sources. For these reasons, HHG is the method of XUV generation described in this thesis, which documents the development of an XUV nanoscope.

1.4 Thesis Aims

In order to obtain high resolution images, it is necessary to have as high flux of high harmonics as possible and to have a scattering setup capable of CDI. Therefore, the aim of this work is to develop a source of high flux XUV radiation and then use the radiation to image nanostructured micron objects so that the development of a table-top XUV nanoscope can be realised.

1.5 Thesis Outline

The building of a table-top XUV nanoscope has several key aspects. This report concentrates on the theoretical and practical process of generating and optimizing high harmonics in an argon gas jet and argon-filled pipe, and details the experimental process of using the XUV light for CDI.

The outline of this thesis is as follows:

This thesis will begin by providing a background into the theory and experimental apparatus used to develop a high harmonic XUV radiation source. The process of HHG will be discussed, and details of the femtosecond laser system and vacuum system used to generate XUV radiation are also provided.

A discussion of the experimental work will begin by investigating the effect of the laser focus position within an argon gas jet on the high harmonic output. The chapter will examine both the output XUV spectrum as well as the fluorescence from the jet for various backing pressures and laser focus positions.

Next, the thesis will build on results obtained from the previous chapter to generate high flux XUV radiation suitable for CDI. Generation from an argon-filled pipe along the laser axis is analysed. Additional methods of maximising XUV output are also considered.

Finally, this work discusses experimental results obtained from CDI. By using XUV radiation from an argon-filled pipe to scatter off a 5 μm pinhole, a nanostructured FIB (focused ion beam) sample and a diatom, this thesis demonstrates the reconstruction of nanostructured micron-sized objects from their scattering pattern using phase retrieval algorithms.

2 XUV Generation

2.1 Introduction

A background into the science and experimental setup used to develop a source of short-pulsed spatially coherent extreme-ultraviolet (XUV) radiation is provided in this chapter. The process of high harmonic generation (HHG) used to produce the XUV radiation is introduced, including the phase matching constraints of the generated high harmonics. In addition, the limitations on harmonic output due to laser intensity and generation medium are discussed. Details of the femtosecond laser and vacuum setup used in the generation of high harmonics are also provided, as well as the diagnostic apparatus used during experimentation.

2.2 High Harmonic Generation

2.2.1 Introduction

When an electromagnetic wave propagates through a medium, it forces electrons in the medium to oscillate. These oscillations, in turn, generate a new electromagnetic wave. For small electron oscillations, the electron motion can be considered as harmonic within a potential well and the polarization of the medium is linear with electric field of the laser. The emitted electromagnetic wave has the same frequency as the incident electromagnetic wave. At higher laser intensities (when the strength of the electric field starts to become comparable to the strength of the atomic field), although the oscillations of the electrons in the medium remain small, the electrons oscillate in a potential well with a response that is nonlinear. The polarization is no longer proportional to the electric field, but proportional to higher order terms of the electric field. In this perturbative regime, the frequency of emitted electromagnetic wave can be modified. Indeed, harmonics of the original incident electromagnetic wave can be generated.

At even higher laser intensities, the polarization of the medium can no longer be treated as perturbative. This is the regime of HHG. The electric field of the laser is so strong that electrons can become ionized and then move freely within the oscillating electric field

of the laser. Upon moving freely within the oscillating field, the ionized electron may return to its parent ion and emit a photon with a frequency that is a much higher than the incident fundamental laser frequency. A model that accounts for such a process is the semi-classical recollision model, developed by Corkum *et al.* [34] and Lewenstein *et al.* [35].

2.2.2 Semi-Classical Model

The semi-classical model is based on the idea that generation proceeds via several steps, as shown in Fig. 2.1.

In the first step (Fig. 2.1 (a)), when an atom's potential is strongly perturbed by an electric field, the outer electron can undergo quantum mechanical tunnelling through the potential barrier that confines the electron and pass into a continuum of unbound states. This tunnelling is most likely to occur at the peak of the laser field when the distortion to the atomic potential is strongest. In the second step (Fig. 2.1 (b)), the electron is now in free space and its trajectory can be approximated as a particle using classical mechanics. The electron is accelerated away from the nucleus by the laser electric field. As the laser electric field reverses, the electron can be accelerated back towards the nucleus, gaining kinetic energy in the process. Finally (Fig. 2.1 (c)), if the electron recombines with the ion, a photon with frequency ω will be emitted. The energy of the emitted photon is equal to the kinetic energy gained by the electron in the electric field of the laser plus the ionization potential of the atom.

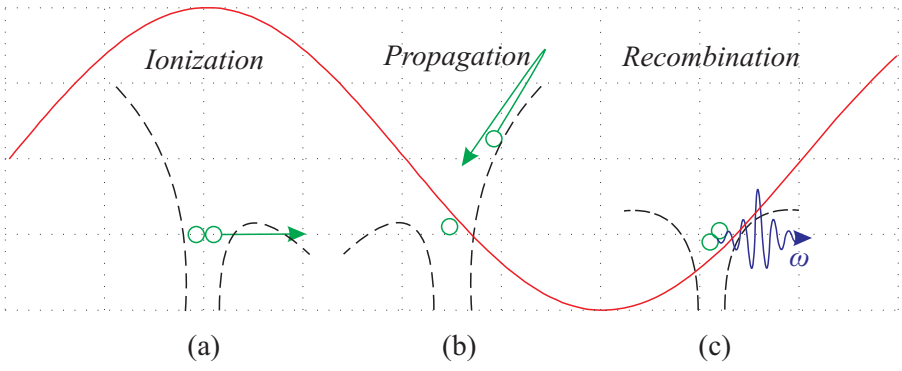

Figure 2.1: 1-dimensional representation of HHG via the semi-classical model, showing (a) tunnelling ionization, (b) electron propagation and (c) electron recombination with the emission of a photon with frequency ω. Adapted from reference [36].

The process described in the semi-classical model is repeated in the cycling electric field of the laser. Since tunnelling is most likely to occur at the peak of the electric field,

emission will occur twice per optical cycle. The subsequent interference between the emitted waves produces a harmonic spectrum [35]. However, because emission is occurring twice per optical cycle, only odd harmonics of the fundamental light are observed. This can be understood upon looking at Fig. 2.2. The plots show the interference of (a) odd harmonics and (b) even harmonics emitted twice per optical cycle. The black line represents the fundamental electric field, the blue dashed line represents the first harmonic emitted per optical cycle and the green circles represent the second harmonic emitted per optical cycle. Assuming that the emission is in phase with the fundamental electric field, if harmonics of odd integer are emitted twice per optical cycle then they interfere constructively, but when even harmonics interfere, they do so destructively.

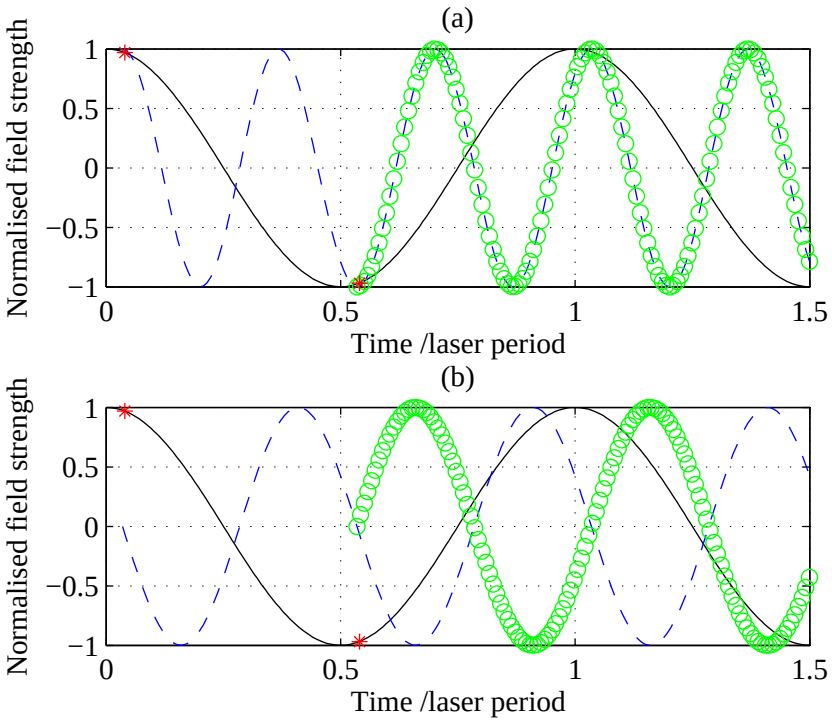

Figure 2.2: Interference of (a) odd harmonics and (b) even harmonics emitted twice per optical cycle. The red star indicates the points of emission, the black line the fundamental electric field, the blue dashed line the first emitted harmonic and the green circles the second emitted harmonic per optical cycle.

2.2.3 Free Space Motion

The trajectory of the electron and the subsequent photon emission upon return to the atom can be determined by solving the equation of motion of a free electron in an oscillating

electric field [35]. An oscillating electric field of amplitude E_0 linearly polarised in the x direction, can be written as,

$$E = E_0 \cos(\omega t) \tag{2.1}$$

where ω is the angular frequency of the laser. Here, the electron is assumed to move into the continuum (the region far away from the potential well) with zero velocity.

By determining the force on an electron due to the electric field of the laser, a classical position $x(t)$ and velocity $v(t)$ for the electron as a function of time can be obtained by integrating the classical equations of motion [37],

$$v(t) = v_0(\sin(\omega t_0) - \sin(\omega t)) \tag{2.2}$$

$$x(t) = x_0(\cos(\omega t_0) - \cos(\omega t)) - v_0 \sin(\omega t_0)\,(t - t_0) \tag{2.3}$$

where $v_0 = eE_0/m_e\omega$, $x_0 = eE_0/m_e\omega^2$ and t_0 is the tunnelling time. Here, the electron is assumed to tunnel into free space with at an initial position $x(t_0) = 0$ and initial velocity $v(t_0) = 0$. In order for HHG to occur, the electron must accelerate away from the nucleus, then return to its original position, $x = 0$ (the nucleus), so that recombination and photon emission can occur.

The paths of electrons for various tunnelling times are calculated from Equation 2.3 and illustrated in Fig. 2.3. As seen in the figure, the electron can pass the nucleus more than once. However, since the electron rarely passes the nucleus more than once for most tunnelling times, only the first return of the electron is considered

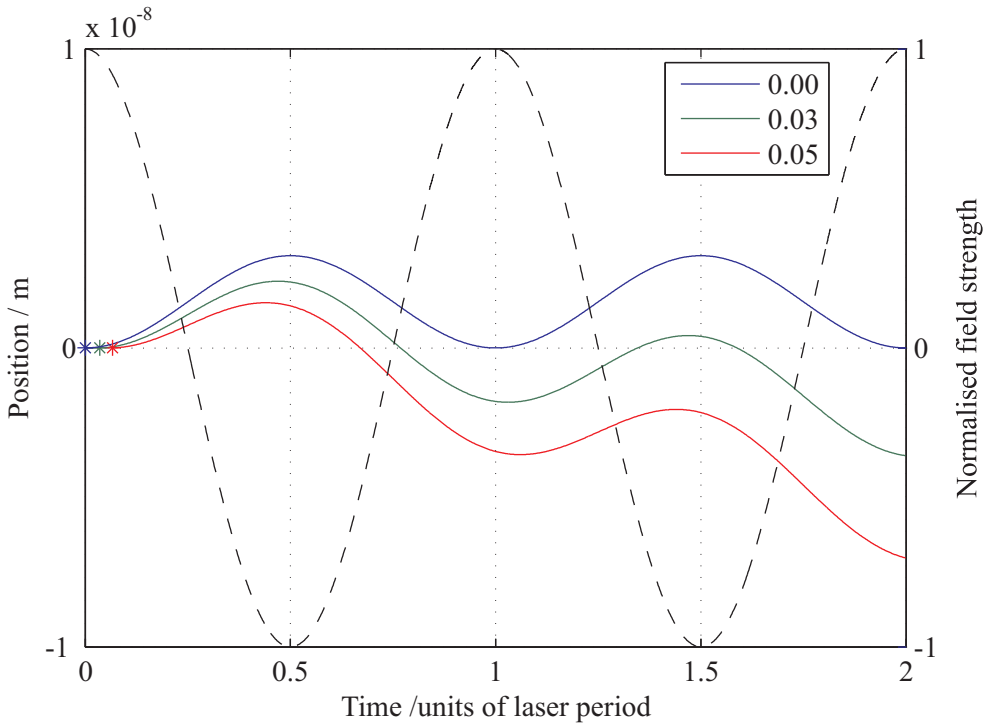

Figure 2.3: Electron position as a function of time for various tunnelling times in units of laser period. The black dashed line indicates the fundamental electric field. The data are calculated using Equation 2.3, with values of E_0 = 5 x 10^{10} V m^{-1} and λ_0 = 790 nm.

The photon energy of the highest harmonic has been predicted to be the sum of the ionization potential of the atom plus the maximum kinetic energy gained by the electron in the laser electric field upon recollision [34],

$$[\hbar\omega]_{max} = I_P + 3.17U_P \tag{2.4}$$

where I_p is the atomic ionization potential and U_p is the mean ponderomotive energy (i.e. the average kinetic energy of an electron moving in the laser electric field), such that,

$$U_p = \frac{e^2 {E_0}^2}{4m_e\omega_0^2} \tag{2.5}$$

where e is the charge of the electron, E_0 is the amplitude of the electric field, ω_0 is the laser frequency and m_e *is* the mass of the electron.

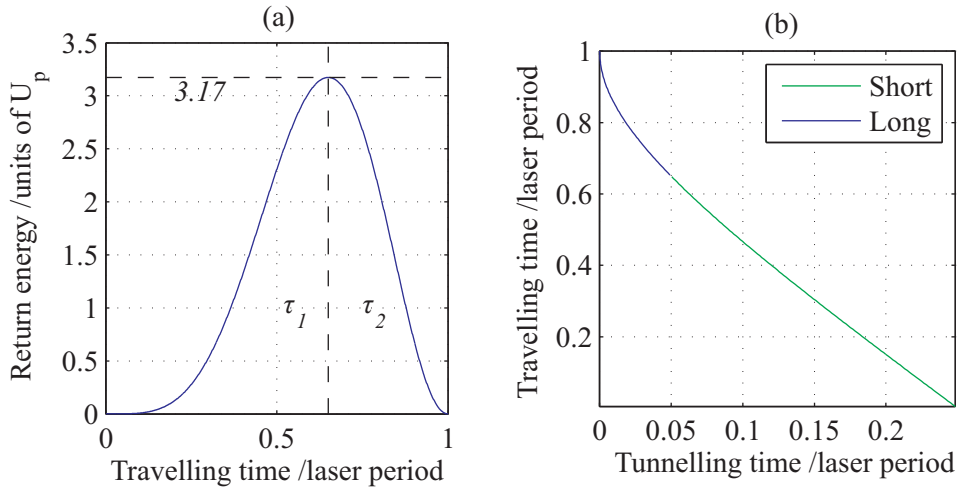

Figure 2.4: (a) Kinetic energy of the electron revisiting the ion core as a function of the travelling time, where τ_1 corresponds to short trajectories and τ_2 corresponds to long trajectories. The data are calculated using Equations 2.2 and 2.6, with values of E_0 = 5 x 10^{10} V m^{-1} and λ_0 = 790 nm. (b) Travelling time for the electron as a function of the tunnelling time. The data are calculated using Equation 2.6,

The time t_1, when the electron revisits the atom, can be determined by calculating the travelling time (the time spent in the continuum by the electron), $\tau = t_1 - t_0$ [38],

$$t_0 = \frac{1}{\omega}\arctan\left(\frac{1-\cos(\omega\tau)}{\omega\tau-\sin(\omega\tau)}\right) \tag{2.6}$$

Using Equation 2.6 to calculate t_0 and therefore the return time t_1 given $x(t_0) = 0$, the velocity in Equation 2.2 can be solved and the kinetic energy upon recollision determined. Figure 2.4 (a), shows the instantaneous kinetic energy of the returning electron as a function of the travelling time, while Fig. 2.4 (b) shows the relationship between the tunnelling time and the travelling time. Two solutions differing in travelling time exist for photon energies lower than the cut-off. As such, they are referred to as short (τ_1) and long (τ_2) trajectories [39]. It is evident from Fig. 2.4 (b) that the earlier an electron is emitted during a laser cycle, the more time it spends in the continuum.

2.2.4 High Harmonic Spectrum

Since monochromatic radiation is often preferred for nanoscale imaging, understanding the emission spectrum of the generated radiation is important. The result of the generation process described above is a spectrum containing a sequence of harmonics in a perturbative

regime, followed by a long plateau of higher order harmonics that ends with a sharp cut-off [40]. This sharp cut-off in the harmonic spectrum has been predicted by Krause *et al.* [41] and observed by L'Huillier *et al.* [42]. Figure 2.5 depicts a typical high harmonic spectrum.

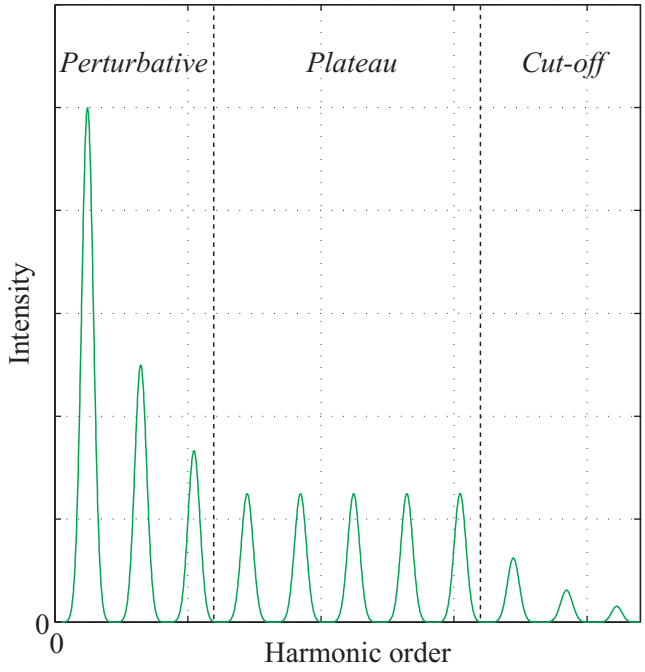

Figure 2.5: A typical high harmonic spectrum showing a perturbative region with harmonics of highest intensity. Following a rapid decrease in intensity is the plateau region – a region of approximately constant intensity. The spectrum ends in a cut-off region, which contains the shortest wavelength harmonics.

2.2.5 Cut-off Wavelength

Due to the diffraction limit, obtaining as a short cut-off wavelength (high cut-off energy) as possible is necessary for high resolution imaging. XUV radiation can be produced via HHG [43,44], commonly achieved by focusing a high energy ultrashort laser pulse into a gas or plasma [45,46]. Such generation typically occurs at laser intensities of the order of ~ 10^{14} W cm^{-2} or higher [42]. The plot in Fig. 2.6 demonstrates the highest possible harmonic photon energy that can be achieved in argon for various pulse lengths and pulse energy when using a 790 nm laser focused to a spot size of 55 μm. The cut-off can be shifted to higher energy by either increasing the pulse energy or by decreasing the pulse length.

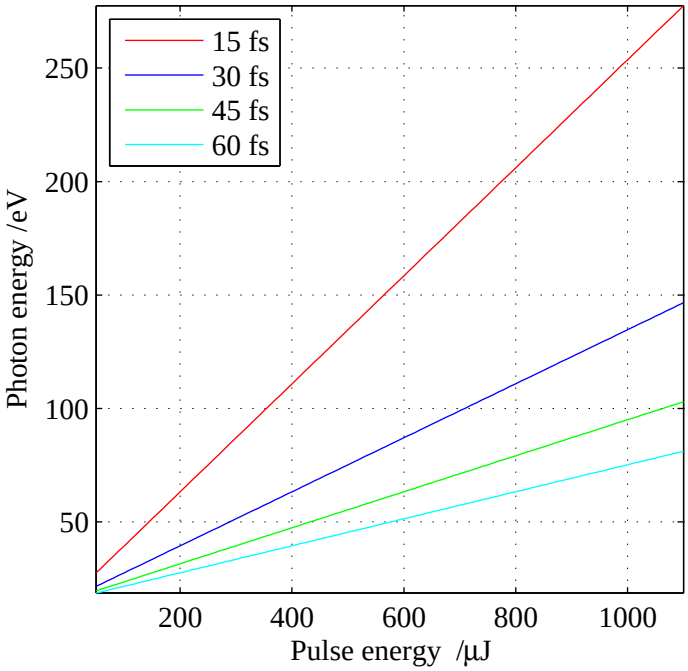

Figure 2.6: The highest photon energy obtainable in argon for laser pulses of wavelength 790 nm and pulse lengths 15, 30, 45 and 60 fs as a function of pulse energy. The data are calculated using Equation 2.4.

An increase in the cut-off energy can also be achieved by using an inert gas that has a higher ionization potential, such as helium [47], or ions which have even higher potentials [48]. Seres *et al.* [49] have been able to achieve photon energies as high as 1.3 keV by focusing a few-cycle laser pulse with a peak intensity of 1.4 x 10^{16} W cm^{-2} into a helium gas jet. By using a shorter focal length optic, higher peak laser intensities and therefore shorter cut-off wavelengths can also be obtained. Table 2.1 presents calculated values of the peak intensity at the laser focus for different focal length optics, including the corresponding ponderomotive energies and cut-off wavelength obtainable for different gases. Laser parameters of 1 W, 40 fs, 1 kHz and 790 nm were used in the calculation. As the focal length decreases and spot size decreases, the peak intensity and therefore ponderomotive energy increases. The ponderomotive energy is approximately 30 times greater for a 10 cm focal length optic than a 60 cm and as a consequence, the cut-off wavelength is an order of magnitude shorter. It is also evident that using helium instead of nitrogen will allow a cut-off wavelength 2 nm shorter when using a 60 cm focal length optic. However, these calculated values are for an ideal scenario. Due to various limitations discussed later, the actual

generated wavelength is generally less. Currently, radiation with wavelength of < 2.5 nm has been demonstrated [50].

Focal length (cm)	ω (μm)	I (W cm^{-2})	U_p(eV)	Cut-off (nm)			
				He	Ar	Ne	N_2
10	*10.99*	*1.07 x 10^{16}*	*618.96*	*0.6*	*0.6*	*0.6*	*0.6*
20	*21.97*	*2.92 x 10^{15}*	*169.83*	*2.2*	*2.2*	*2.2*	*2.2*
30	*32.96*	*1.32 x 10^{15}*	*76.87*	*4.6*	*4.8*	*4.7*	*4.8*
40	*43.95*	*7.49 x 10^{14}*	*43.52*	*7.6*	*8.1*	*7.8*	*8.2*
50	*54.93*	*4.81 x 10^{14}*	*27.94*	*11.0*	*11.9*	*11.2*	*12.1*
60	*65.92*	*3.34 x 10^{14}*	*19.43*	*14.4*	*16.1*	*14.9*	*16.3*

Table 2.1: Focal spot sizes and corresponding cut-off wavelengths for various gases. Laser parameters of 1 W, 40 fs, 1 kHz and 790 nm were used in the calculation. The data are calculated using Equation 2.4.

2.2.6 Quantum Mechanical Model

The semi-classical model of the single atom response to an intense laser electric field detailed so far can predict the cut-off energy and electron return times, but it does not explain processes such as recombination or quantum interference of electron trajectories. A fully quantum mechanical model of the single atom response is required for a complete understanding of experimental results obtained from HHG.

In a quantum mechanical model, at high laser electric field strength part of the electron wavefunction can undergo quantum mechanical tunnelling through the potential barrier that confines the electron and pass into free space. As the laser electric field reverses, the electron wavefunction reverses direction and heads back towards the ion. Having changed in energy and therefore shifted in frequency, if the electron returns to the ion, the electron wavefunction interferes with the part of the electron wavefunction that remained with the ion. The resultant interference produces a dipole oscillation which emits a photon at the beat frequency of the interference. By solving the time-dependent Schrödinger equation for a single atom in an intense laser electric field, the experimentally observed characteristics of HHG, such as the harmonic spectrum, can be predicted (see for example, [51,52]). Predictions made in the semi-classical model, which include electron return times, are also predicted in a quantum mechanical model [35]. Due to such demonstration of equivalence, only semi-classical modelling is considered necessary in this thesis.

2.3 Ionization

HHG from an atom can only occur when it is ionized. It is therefore important to understand the ionization at a given time during irradiation by a laser pulse. In the presence of a strong electric field, there are three regimes in which an atom can be ionized: multi-photon ionization (MPI), which dominates at lower intensities; tunnelling ionization, which dominates when the atomic potential is distorted such that quantum tunnelling can occur; above barrier ionization (ABI), which occurs when the atomic potential is distorted to an extent that the electron can pass over the top of the potential barrier. The intensity threshold for ABI is given by [53],

$$I_c = 4 \times 10^9 \left(\frac{I_p^4}{Z^2}\right) \tag{2.7}$$

where I_c is expressed in W cm^{-2}, Z is the residual charge on the ion after ionization and I_p is the ionization potential of the atom in eV. For argon, this intensity is 2.5 x 10^{14} W cm^{-2}.

To determine whether the dominant process is tunnelling or MPI, it is necessary to consider the value the Keldysh factor [54],

$$\gamma = \frac{1}{2K_0 F} \tag{2.8}$$

where $K_0 = I_p/\hbar\omega$ is the number of photons required for MPI, $F = E/\kappa^3 E_a$ is the reduced field such that $\kappa = (I_p/I_H)^{1/2}$, I_H is ionization potential of a hydrogen atom, ω is the laser frequency, E is the amplitude of the electric field, E_a = 5.14 x 10^{11} V m^{-1} is the atomic unit of electric field intensity and l and m are the angular momentum and magnetic quantum numbers of the atom respectively. If $\gamma \ll 1$, tunnelling ionization is dominant, whereas if $\gamma \gg 1$, MPI is dominant. For work described in this thesis, tunnelling ionization is more dominant than MPI. With knowledge of the Keldysh parameter, the rate of tunnelling ionization can be determined [55],

$$\omega_{TI} = \kappa^2 C_{\kappa l}^2 \sqrt{\frac{3}{\pi}} (2l+1) \frac{(l+m)!}{2^m m!\,(l-m)!} \\ 2^{2n^*-m} F^{m+1.5-2n^*} \exp\left[-\frac{2}{3F}\left(1-\frac{1}{10}\gamma^2\right)\right] \tag{2.9}$$

where $C_{\kappa l}$ is the dimensionless asymptotic coefficient of the atomic wavefunction away from the nucleus (see reference [55,56] for values), $n^* = Z/\kappa$ is the effective principal quantum number. From the ionization rate, the ionization fraction can be calculated,

$$\eta(t) = 1 - \int_0^t N_a(t')\omega_{TI}(t')dt' \tag{2.10}$$

where N_a is the number of atoms.

The ionization fraction given in Equation 2.10 for a specific gas is dependent on the laser pulse energy and pulse length. The final ionization fraction for different laser peak intensities and pulse lengths when generating using argon is shown in Fig. 2.7. It is clear that for a given peak laser intensity, the ionization fraction decreases as the pulse length decreases. The important role the ionization fraction plays in obtaining as high output flux as possible is due to its role in the phase matching between the fundamental light and the harmonics, which is discussed in the next section.

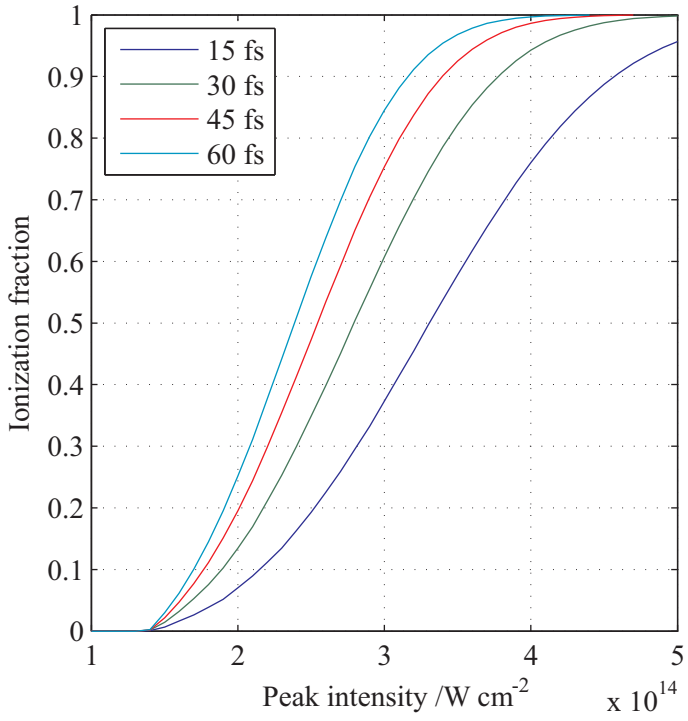

Figure 2.7: Final ionization fraction calculated for 15, 30, 45 and 60 fs pulses as a function of peak intensity when generating from argon. The data are calculated using Equations 2.9 and 2.10.

2.4 Phase Matching

To produce high output harmonic flux, phase matching between the fundamental and the harmonics is required. If waves are not phase-matched, then the generated harmonics will interfere destructively and so significant buildup of harmonic signal is not achieved. Figure 2.8 demonstrates the basic principles of phase matching for second harmonic generation. In order for the second harmonic flux to buildup over the length of the medium, harmonics generated from multiple points in the interaction region must interfere constructively. This is the case in Fig. 2.8 (a), where harmonic emitted from *P* is in phase with harmonic emitted from *Q*. In Fig. 2.8 (b), harmonics emitted from *P* and *Q* interfere destructively and so efficient buildup does not occur. As such, rather than obtaining a rapid increase in signal intensity over the length of the medium, only growth of harmonic signal over the coherence length is achieved. The coherence length is defined as,

$$L_{coh} = \frac{\pi}{|\Delta \boldsymbol{k}|} \tag{2.11}$$

where $\Delta \boldsymbol{k}$ is the spatially varying wavevector mismatch (phase mismatch),

$$\Delta \boldsymbol{k} = q\boldsymbol{k}_{laser} - \boldsymbol{k}_{harmonic} \tag{2.12}$$

Here, q is the harmonic number and phase matching occurs when $\Delta \boldsymbol{k} = 0$.

By reducing the phase mismatch, the coherence length can be increased and a longer buildup of harmonic signal can be achieved. The phase mismatch consists of contributions from the atomic phase contribution due to the delay in emission depending on electron trajectory, the geometrical wavevector contribution, which in this work is the Gouy phase shift (including the curvature of the wavefront)[1], the refractive indices of the gas at fundamental and harmonic wavelength, and the refractive index of the plasma created via ionization.

[1] Note that when generating using a gas-filled capillary, the geometrical wavevector contribution of the Gouy phase shift is replaced by the waveguide dispersion [57].

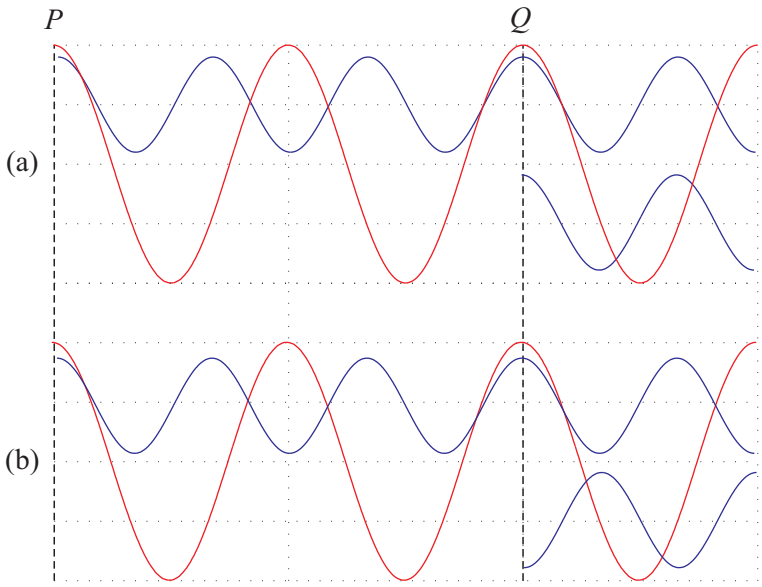

Figure 2.8: Schematic showing the principles of phase matching for second harmonic generation. The fundamental electric field (red line) generates a second harmonic component (blue line). (a) Harmonics emitted from P and Q are in phase and interfere constructively. (b) Harmonics emitted from P and Q are out of phase and interfere destructively.

The atomic phase contribution varies depending on the electron trajectory. The phase of the emitted radiation with respect to the fundamental is proportional to the quasi-classical action acquired by the electron along its trajectory [58]. The quasi-classical action is defined as,

$$S(p, t_0, t_1) = \int_{t_0}^{t_1} dt \left(\frac{p^2(t)}{2m_e} + I_p \right) \tag{2.13}$$

where t_0 is the tunnelling time, t_1 is the recombination time, m_e is the electron mass, p is the electron's classical momentum and I_p is the ionization potential of the atom. The harmonic phase is related to the quasi-classical action by,

$$\Phi_{at} = -\frac{S(p, t_0, t_1)}{\hbar} + q\omega t_1 \tag{2.14}$$

where q is the harmonic number and ω is the angular frequency of the laser.

It is evident from Fig. 2.9 that the phase of long trajectories has a stronger dependence on laser intensity than short trajectories. As a result, the phase will vary less with radius for short trajectories. The harmonics generated from short trajectories will therefore diverge less

than harmonics generated from long trajectories. The wavevector for the spatial dependence of the atomic phase is given by,

$$\boldsymbol{k}_{at}(r,z) = \nabla\Phi_{at}(r,z) \tag{2.15}$$

where r is the radial distance from the centre axis of the laser beam and z is the distance along the laser propagation axis. Such phase is only acquired by harmonics and so the atomic phase wavevector of the fundamental light is zero.

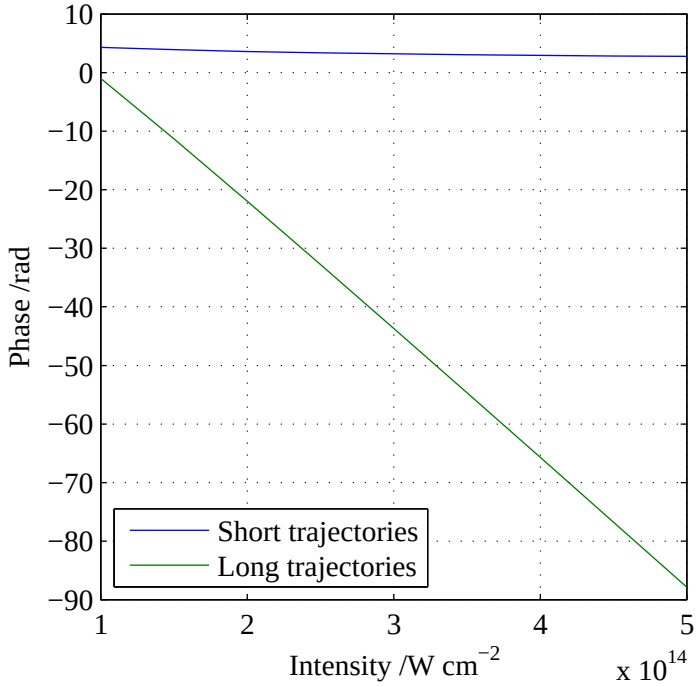

Figure 2.9: Phase acquired by an electron as a function of laser intensity for the 19th harmonic for short (τ_1) and long (τ_2) trajectories. The gas used is in the calculation is argon. The data are calculated using Equation 2.14.

When generating in a gas-filled cell/pipe or gas jet using a freely propagating focused laser beam, the Gouy phase shift (phase shift acquired by a Gaussian beam as it propagates through free space) also contributes to the phase matching process [59]. For a Gaussian beam, the Gouy phase (including the curvature of the wavefront) can be written as,

$$\Phi_{\text{Gouy}}(r,z) = \arg\left[\frac{1}{b+2iz}\exp\left(-\frac{\boldsymbol{k}_1 r^2}{b+2iz}\right)\right] \tag{2.16}$$

where b stands for the confocal parameter and $\boldsymbol{k}_1$ stands for the spatial dependence of the wavevector of the fundamental Gaussian beam in the z direction. Here, r is the radial distance from the centre axis of the laser beam and z is the distance along the laser propagation axis. The wavevector contribution due to the Gouy phase for the fundamental light is therefore,

$$\boldsymbol{k}_{Gouy}(r,z) = q\boldsymbol{k}_1 + q\,\nabla\arg\left[\frac{1}{b+2iz}\exp\left(-\frac{\boldsymbol{k}_1 r^2}{b+2iz}\right)\right] \tag{2.17}$$

Note that the wavevector contribution due to the Gouy phase for high order harmonics is small compared to that for the fundamental light.

In addition to the atomic and the Gouy phase mismatch, the phase mismatch due to the refractive index of neutral gas medium $\Delta\boldsymbol{k}_{neutral}$ and the free electrons $\Delta\boldsymbol{k}_{plasma}$ should also be considered. The neutral gas wavevector can be calculated using [60],

$$\boldsymbol{k}_{gas} = \frac{2\pi P(1-\eta)\delta(\lambda)}{\lambda} \tag{2.18}$$

where P is the pressure of the gas, η is ionization fraction and $\delta(\lambda)$ is the neutral gas dispersion. For the fundamental wavelength, $\delta(\lambda)$ is calculated using the Sellmeier formula [61], and for XUV wavelengths, $\delta(\lambda)$ is calculated from [17].

The wavevector for the plasma is significant for the fundamental beam but is negligible for the high harmonics [62]. It is defined as,

$$\boldsymbol{k}_{plasma} = \frac{q2\pi}{\lambda_0}\left(1-\frac{\omega_p^2}{\omega_0^2}\right)^{1/2} \tag{2.19}$$

where ω_p is the plasma frequency,

$$\omega_p = \left(\frac{\eta e^2 N_e}{m_e \epsilon_0}\right)^{1/2} \tag{2.20}$$

such that N_e is the electron number density, e is the charge of an electron, m_e is the mass of an electron and ε_0 is the permittivity of free space.

The total phase mismatch results from the vector sum of all of contributions,

$$\Delta\boldsymbol{k} = \Delta\boldsymbol{k}_{at} + \Delta\boldsymbol{k}_{Gouy} + \Delta\boldsymbol{k}_{gas} + \Delta\boldsymbol{k}_{plasma} \tag{2.21}$$

where $\Delta \boldsymbol{k}_{at}$ is the net modification due to the phase acquired by an electron after tunnelling, $\Delta \boldsymbol{k}_{Gouy}$ is the net modification from focusing and propagation, $\Delta \boldsymbol{k}_{gas}$ is the net modification due to the gas and $\Delta \boldsymbol{k}_{plasma}$ is the net modification due to the plasma.

Since the Gouy phase mismatch is anti-symmetric about the focus and the atomic, gas and plasma phase mismatch are symmetric for a constant gas density, the total phase mismatch can be reduced by altering the position of the generation medium with respect to the focus. The contribution of the gas phase mismatch can be reduced by operating at low gas pressures, while the plasma and atomic phase mismatch can be reduced by using lower laser intensities.

2.4.1 Quasi-Phase Matching

If the phase mismatch is so high that significant buildup of harmonic flux cannot be achieved, then a technique proposed by Armstrong *et al.* [63] known as quasi-phase matching (QPM) can be employed to increase the flux [64,65]. By using a generation medium with periodic structure to suppress signal when the fundamental and harmonics are out of phase and not when they are in phase, greater cumulative buildup of harmonic signal can be achieved. This is demonstrated in Fig. 2.10. In a phase-matched process (red line), the harmonic intensity increases proportionally to the square of the number of coherent emitters and hence the signal grows as the square of the propagation distance in a homogeneous medium (see next section). However, in a non-phase matched process (blue line), the output harmonic intensity modulates with a period that is twice the coherence length, L_{coh}. The effect of employing QPM is demonstrated by the green line in the figure. A generation region with a period of modulation that is equal to the coherence length allows cumulative buildup along the length of the medium by reducing the out of phase signal.

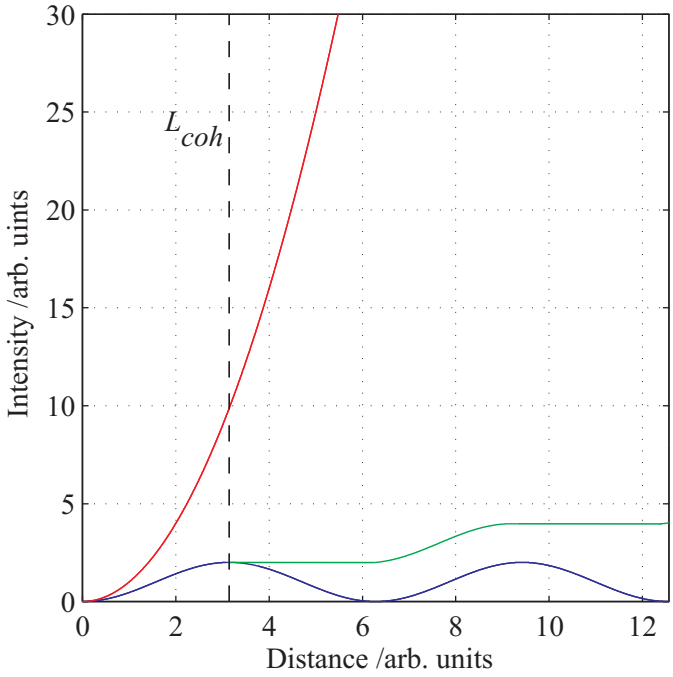

Figure 2.10: Growth of harmonic intensity with phase matching (red), without phase matching (blue) and with quasi-phase matching (green).

Since HHG is a highly sensitive process, even a small change in the density of the gas could be enough to allow QPM to operate [66,65]. There are several ways to achieve QPM using a density modulation. Seres *et al.* [67] demonstrated QPM by using two gas-filled pipes to create a modulated density along the laser axis. The two pipes were translated away from each other and the output high harmonic flux was recorded. A peak in the output flux was recorded when the pipes were at a distance that created a suitable period of modulation for QPM to occur. In another paper (Pirri *et al.* [68]), an increase in high harmonic flux was achieved by modulating the generation medium using multiple gas jets.

2.5 Absorption

In order to maximise the XUV flux, the effect of absorption needs to be considered. The absorption of light by a material varies depending on the material's density and the wavelength of the light. Using data tabulated by Henke *et al.* [17], Fig. 2.11 shows transmission as a function of photon wavelength for XUV radiation through 1 cm of argon, helium, neon and nitrogen gas at a pressure of 10 mbar. Generally, longer XUV wavelengths are less transmissive, though absorption is relatively low across all wavelengths for helium and neon.

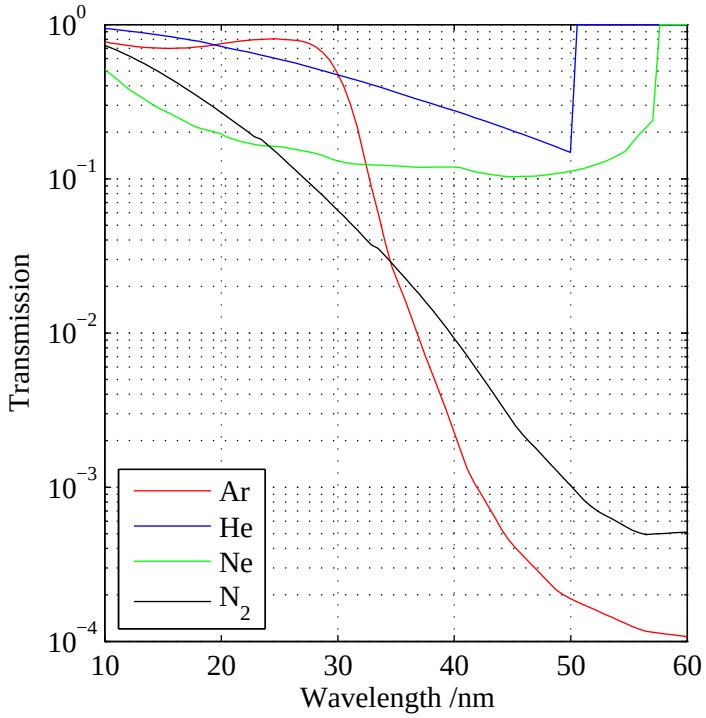

Figure 2.11: Transmission through 1 cm of argon, helium, neon and nitrogen at 10 mbar for XUV radiation between 10 and 60 nm. The data are displayed on a $\log_{10}$ scale and taken from reference [17].

Although the output flux will increase with increasing gas pressure due to a higher number of atoms to generate from, the absorption will also increase. In the presence of absorption, the output intensity of the q^{th} harmonic can be written as [60],

$$\left|E_q\right|^2 \approx N^2 \left|\chi_{eff}^{(q)} E_0^s\right|^2 \left(\frac{1 + e^{-2\alpha L} - 2e^{-\alpha L} cos\Delta \boldsymbol{k} L}{\alpha^2 + \Delta \boldsymbol{k}^2}\right) \tag{2.22}$$

where N is the number density of atoms, $\chi^{(q)}_{eff}$ is the effective nonlinear susceptibility of the q^{th} harmonic, E_0 is the input electric field, s is the effective order of the nonlinearity (~ 5) [69], α is the absorption coefficient and $\Delta \boldsymbol{k}$ is the total wavevector mismatch. The terms in the round brackets describes the contribution of phase matching to the output intensity of the q^{th} harmonic in the presence of absorption. From the equation, it is evident that the intensity of the harmonic signal increases quadratically with the number density of the atoms, as long as there is no change in the coherence length or absorption. The length of the buildup of high harmonic signal is limited by the shorter of the absorption length, $L_{abs} = 1/2\alpha$ (the distance in which the intensity of light drops to 1/e in a material) and the coherence length, $L_{coh} = \pi/|\Delta \boldsymbol{k}|$.

If the absorption length is shorter than the coherence length, then the output flux will be limited by absorption and not the phase mismatch.

The output intensity of the q^{th} harmonic as a function of medium length for various coherence lengths is plotted in Fig. 2.12. For a phase-matched process, the output harmonic intensity in the absence of absorption is proportional to the square density and therefore square of length of the medium. However, in the presence of absorption, the high harmonic signal saturates when the length of the medium is longer than several absorption lengths, even for an infinite coherence length [70]. The harmonic output saturates at a lower intensity as the coherence length decreases for a given absorption length. As the absorption length decreases for a given coherence length, the harmonic emission will saturate at even smaller values. It is therefore desirable to generate under conditions where the coherence length is as long as possible and the absorption is as low as possible in order to maximise XUV flux.

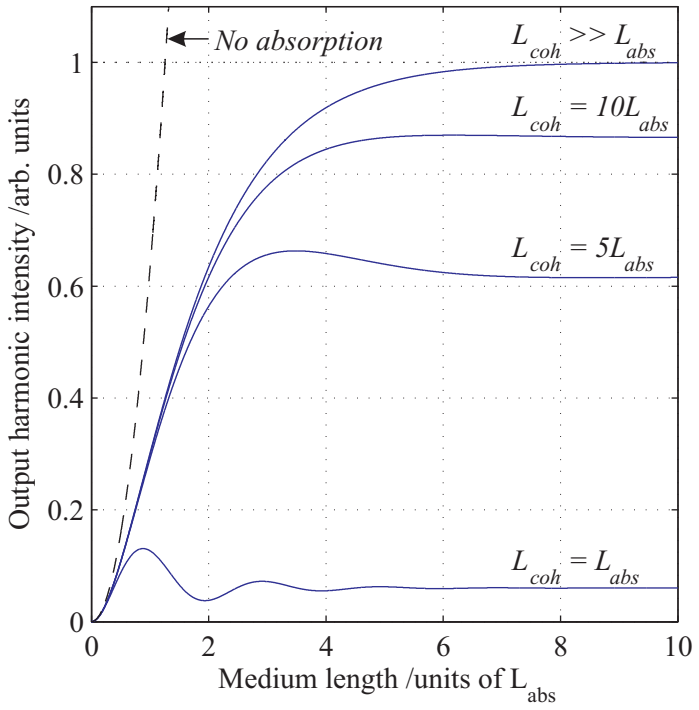

Figure 2.12: Output intensity of the q^{th} harmonic (arbitrary units) as a function of medium length (in units of absorption length) for different ratios of the absorption length L_{abs} to the coherence length L_{coh}. The dotted line corresponds to the case of zero absorption. Adapted from reference [70].

2.6 Experimental Setup

2.6.1 Femtosecond Laser System

It is necessary to create a pulse that is as short in time as possible to obtain high cut-off energy and high flux of the generated harmonics [71]. The femtosecond laser system used in this project is designed to produce 790 nm, 40 fs, 3 mJ pulses at a 1 kHz repetition rate. The setup is shown as a block diagram in Fig. 2.13. The purpose of the first part of the system is to produce short pulses, while the purpose of the second part the system is to amplify the pulses.

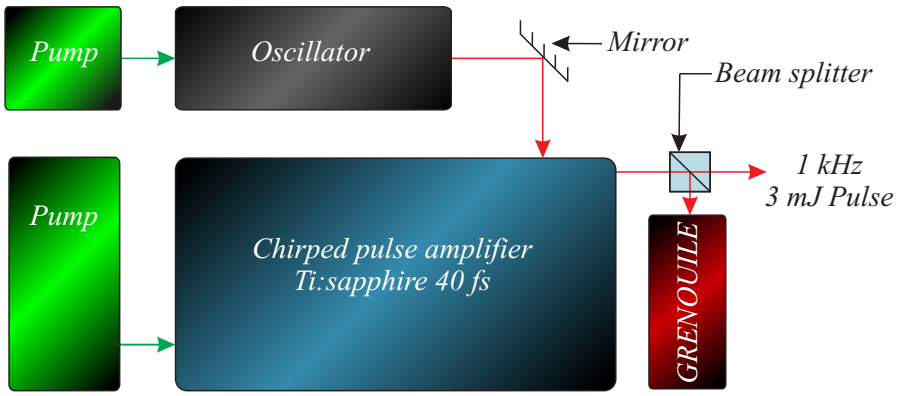

Figure 2.13: Block diagram of femtosecond laser system.

2.6.1.1 Ti:sapphire Oscillator

A mode-locked Ti:sapphire laser cavity is used as the seed laser [72,62], which is pumped by a 4.5 W Spectra Physics Millennia diode pumped laser operating at 532 nm. In this setup, the pump laser beam enters a cavity that contains mirrors, prisms and a Ti:sapphire crystal (see Fig. 2.14 for schematic of setup). The crystal is the gain medium and also allows a technique known as Kerr lens mode-locking (KLM) to occur, in which pulsed light is more focused than continuous [73]. Pulsed light is favoured in the cavity by the presence of concave mirrors, while a slit allows tuning of the pulse wavelength. The prisms act as a dispersion compensator to aid in the production of short pulses. Once mode-locked, the Tsunami oscillator produces 25 fs pulses at 500 mW, with a repetition rate of 82 MHz. These pulses are then directed into the amplifier along with a pump laser beam, which is provided by a diode pumped, frequency doubled Q-switched Nd:YLF laser (Positive Light Evolution 30) operating at 20 W, 527 nm and 1 kHz repetition rate.

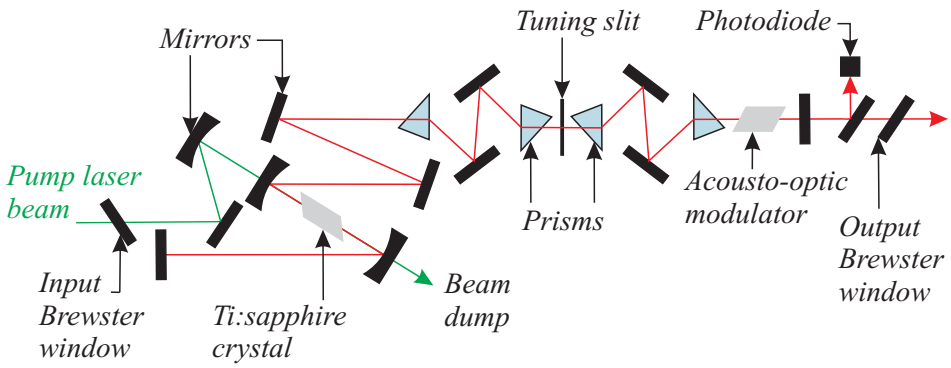

Figure 2.14: Schematic of the optical configuration of the Ti:sapphire oscillator.

2.6.1.2 Chirped Pulse Amplifier

Chirped pulse amplification (CPA) is a system that uses an amplifier to amplify ultrashort laser pulses [74]. In the CPA system used in experiments documented in this thesis (Newport Spitfire Pro, shown schematically in Fig. 2.15), a laser pulse is initially stretched out in time using a grating so that the low frequency components travel a shorter distance than the high frequency components (pulse becomes positively chirped). Once a pulse has been chirped, its peak intensity is low enough for it to pass into a regenerative amplifier without suffering from significant nonlinear effects or causing damage to the gain medium. The regenerative amplifier is a cavity that consists of mirrors and a gain medium (Ti:sapphire crystal) that is pumped by a separate laser. The stretched pulse is passed into this cavity via a Pockel's cell (an electro-optic switch) where it can make many round trips, gaining energy in the process. The timing of the Pockel's cells switching is optimized so that a minimum number of passes through the medium are made in order to use up all the gain but minimise dispersion effects. Once all the gain is used up, the pulse is released from the resonator by the Pockel's cell. Finally, the pulse is compressed in a similar way in which it was stretched. This time in the grating setup, the low frequency components travel a longer distance than the high frequency components, thus causing the pulse to compress. The resultant laser pulses have an average energy of 3 mJ with a FWHM of 40 fs.

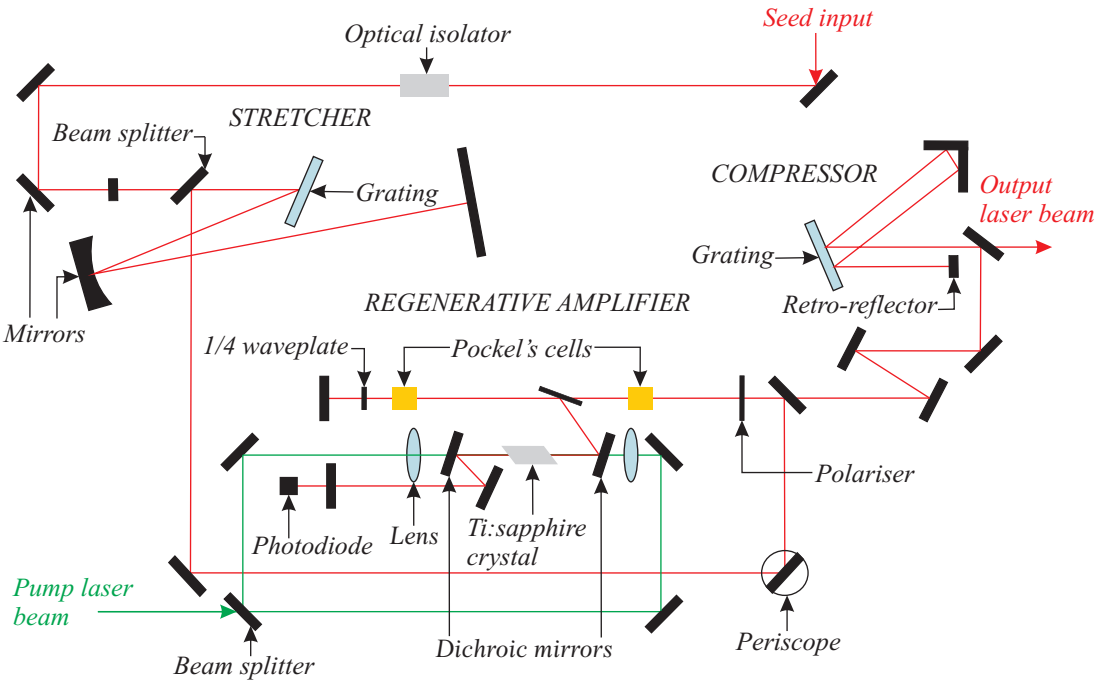

Figure 2.15: Schematic of the CPA system.

2.6.1.3 GRENOUILLE

It is important to measure the temporal length of the laser pulses during experiments since small fluctuations will change the peak intensity of the laser and thus affect the generated XUV radiation. A device to measure the temporal length of an ultrashort pulse is a GRENOUILE (gating-eliminated no-nonsense observation of ultrafast incident laser electric fields). A GRENOUILE is essentially a slim-line version of a FROG (frequency resolved optical gating) [75] and determines the length and phase of pulses as short as 20 fs [76]. One (a FROG 8-20-125) is inserted into the beam line after the laser amplifier with the use of a 96:4 beam splitter to allow continuous monitoring of the laser pulses. Figure 2.16 displays a GRENOUILE trace of a 44 fs pulse from the CPA system used in this work.

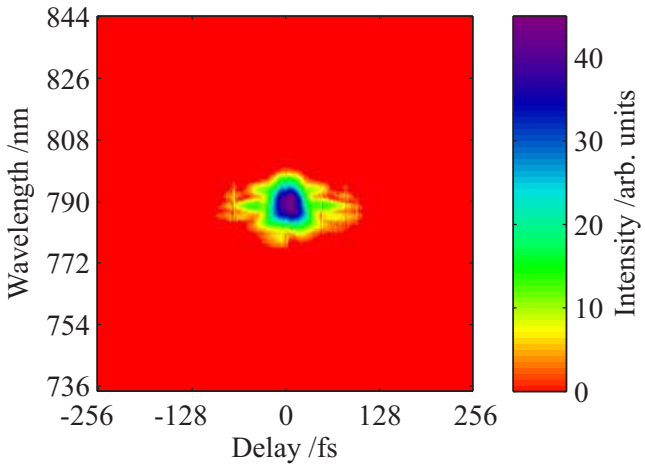

Figure 2.16: GRENOUILE trace of a 44 fs pulse from the CPA system.

2.6.1.4 Laser Beam Quality Factor

The laser beam quality factor, also known as the M^2 parameter, quantifies the difference between the divergence of a real beam and that of a diffraction limited Gaussian beam with the same wavelength [77]. The M^2 will affect the focal spot size and thus the peak intensity of the focused laser beam. As such, knowledge of the M^2 of the laser beam allows appropriate choice of focusing optics used to focus the laser beam in the HHG setup. Assuming a monochromatic source, the M^2 can be determined from spatial intensity measurements of the laser through the focus and by using [78],

$$w(z) = w_0 \sqrt{1 + \left(\frac{M^2 \lambda z}{\pi {w_0}^2}\right)^2} \tag{2.23}$$

where $w(z)$ is the $1/e^2$ half-width of the spatial intensity of the beam, w_0 is the $1/e^2$ half-width of the spatial intensity of the beam at the focus and z is the distance from the focus along the laser propagation axis. Work done by Butcher [79] gave an M^2 of 1.38 in x and 1.80 in y for the laser beam used in experiments discussed in this thesis. The laser focus is therefore 1.38 times larger in the x-direction and 1.80 times larger in the y-direction than that of a diffraction limited Gaussian beam.

2.6.2 Vacuum Setup

Following amplification, the laser has the option of being sent into two separate vacuum setups by a beam splitter. Both setups consist of their own XUV generation systems. The

vacuum setup used in the experiments documented in this thesis is shown schematically in Fig. 2.17.

The vacuum setup is designed to reduce the amount of gas outside the HHG region and therefore reduce absorption from non-generating gas. To remove the gas, two pumping towers that are approximately 15 cm in diameter and 30 cm high are placed either side of the HHG setup (gas jet or gas-filled pipe). Each tower has a turbomolecular pump (Leybold TW300) placed on top and both are connected to a backing pump. These pumps enable pressures as low as 10^{-6} mbar to be obtained inside the pumping towers. There is also an additional smaller pump (Leybold TW70) on the end of an XUV spectrometer[2] (Schulz Scientific Instruments LPS-VUV-NG1), which is also connected to a backing pump. The gas used in the generation of high harmonics is passed into the HHG setup through a 6 mm outer diameter pipe and can be maintained at a constant pressure using a TESCOM ER-3000 controller.

The laser is focused into the vacuum setup and toward a gas jet or gas-filled pipe by a 50 cm plano-convex lens. The lens was chosen as a balance between confocal length (and thus potential length of generation region) and potential cut-off wavelength. Approximately 40 cm along from the XUV source is a filter holder that is mounted on a linear push/pull feed-through. It consists of a train of four 1 cm diameter holes: one is open to allow gas to flow between chambers during pumping down, while the other holes each contain a 200 nm thick aluminium filter. These filters are designed to block the fundamental laser but allow significant transmission of XUV. In this way, a beam consisting of only XUV radiation can be used for scattering.

[2] For more information on the XUV spectrometer, see Appendix A.

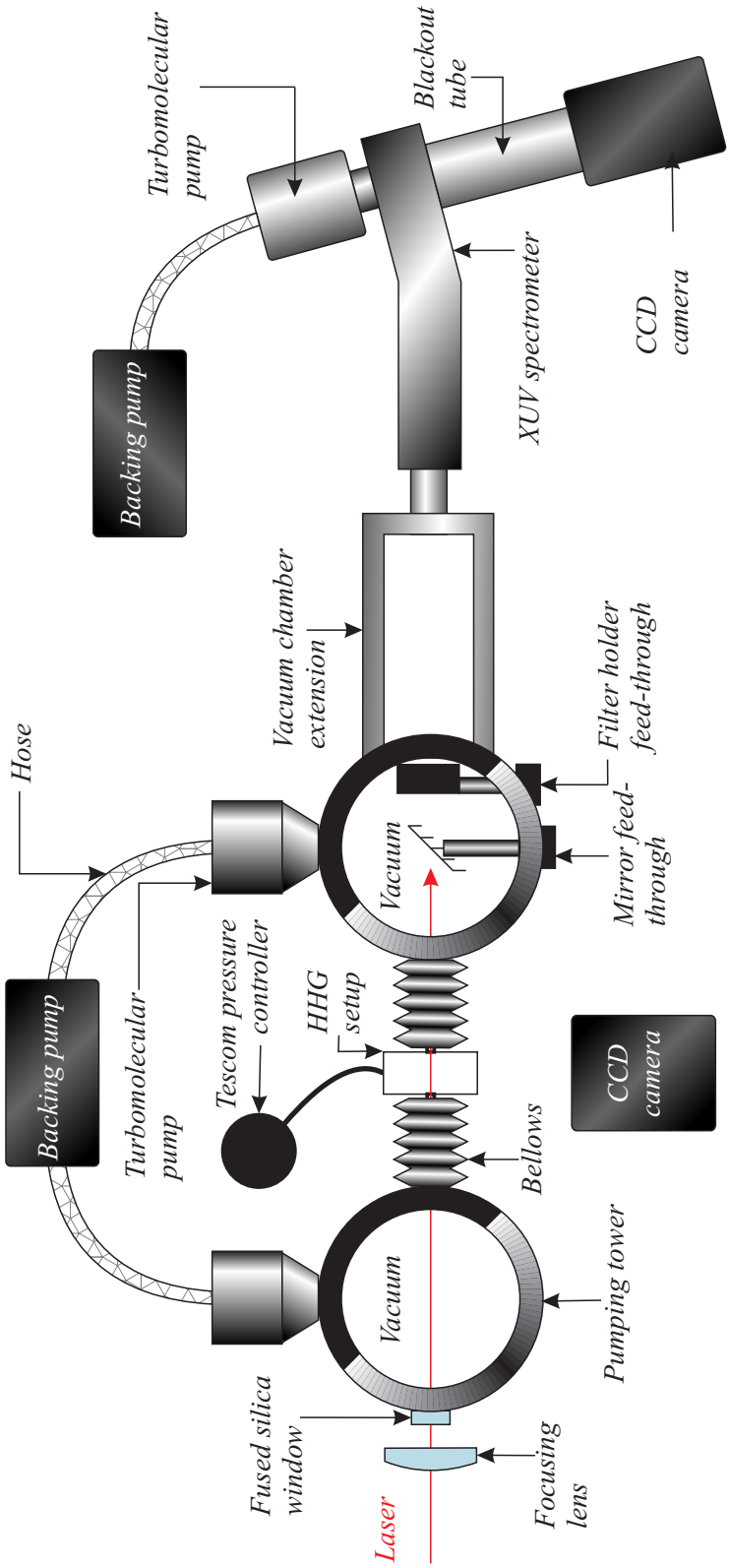

Figure 2.17: Top view schematic of the vacuum setup showing the generation setup and XUV spectrometer.

The output spectrum of the generated radiation can be recorded using the microchannel plate XUV spectrometer that is placed further along the setup and the spatial variation in the intensity of the XUV beam can be recorded using a 1024 x 1024 pixel XUV charged coupled device (CCD) camera (Andor DX-434) that can be placed into the beam line in the extension chamber shown in Fig. 2.17. Further push/pull feed-through systems include a mirror that can be used to monitor the laser beam and aid in the alignment of the laser beam through the HHG setup.

Additional diagnostic apparatus includes a 1024 x 1024 pixel visible light CCD camera (Pixis 400) and photomultiplier tube (PMT) placed perpendicular to the generation region and laser axis in order to spatially resolve and temporally resolve any fluorescence emitted from the generation region during HHG.

2.6.2.1 Filters

Depending on the wavelength of harmonics to be used for scattering and analysis using the spectrometer and CCD camera, the correct material and thickness of filter needs to be chosen. Different metals have different absorption lengths. For example, compared to zirconium and gold, aluminium is very transmissive in the wavelength range ~ 20-60 nm (see Fig. 2.18). However, at around 10 nm the transmission of gold and zirconium is much better than aluminium. Therefore to enable high transmission of XUV radiation between 20 and 60 nm, 200 nm aluminium filters are used. Such filters allow a transmission of ~ 10 % of XUV radiation and reduce the transmission of the fundamental wavelength (790 nm) by a factor of 10^8.

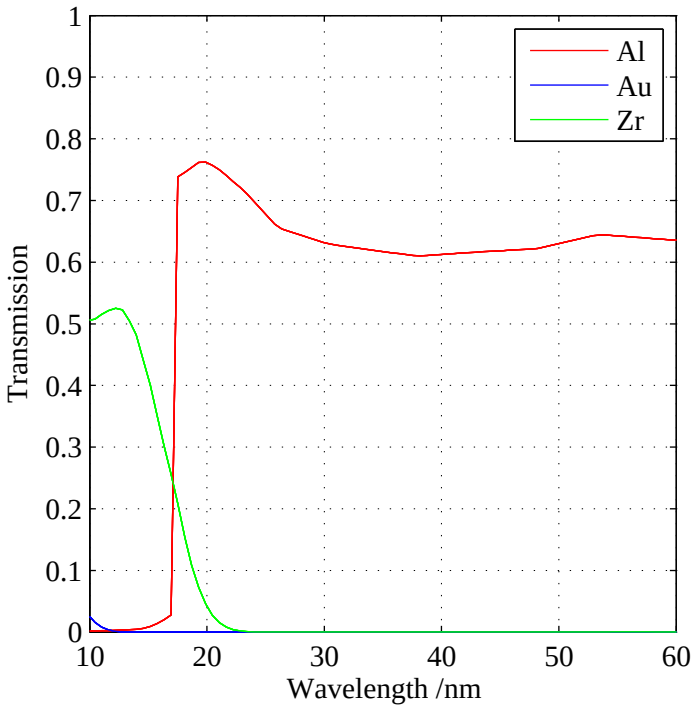

Figure 2.18: Transmission through 200 nm of aluminium, gold and zirconium for XUV radiation between 10 and 60 nm. The data are taken from reference [17].

2.6.2.2 Photomultiplier Tube Setup

To determine the temporal variation of any fluorescence observed from excited atoms and ions created by the intense laser in the HHG region, a PMT that contains a GaAs photocathode is used to record the visible fluorescence. The PMT is thermoelectrically cooled in order to reduce the thermal noise and thus improve the signal-to-noise ratio. The PMT is powered by a high voltage Brandenberg photomultiplier power supply set at 1500 V (see Fig. 2.19 for block diagram of setup). The output signal collected from the PMT is amplified by a SR445 amplifier and sent to a SR400 gated photon counter that has a maximum resolution of 5 ns. The counter is triggered in synchronization with the laser pulses.

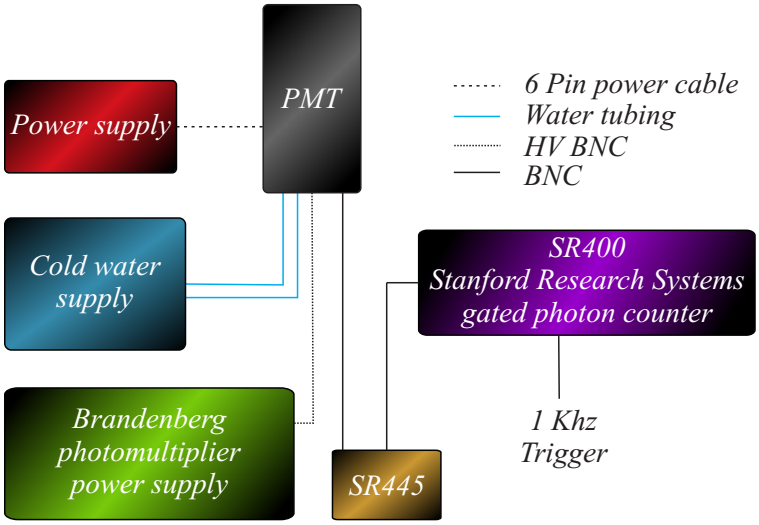

Figure 2.19: Block diagram of the configuration of the photomultiplier tube setup.

2.7 Summary

A background into the science and experimental apparatus used in the development of a table-top XUV source has been provided. The process of HHG has been discussed, along with the limitations on output harmonic flux due to phase matching and gas absorption. A balance of generation conditions is necessary to produce high flux short wavelength XUV radiation suitable for nanoscale imaging. The influence of gas jet structure on HHG with the aim of maximising XUV flux from an argon gas jet is discussed in the next chapter.

3 Influence of Gas Jet Structure on XUV Generation

3.1 Introduction

As discussed in the background chapter, the generated harmonic flux is limited by a phase mismatch between the fundamental and generated harmonics, as well the density of nonlinear material present – both of which are dependent on the gas geometry. To date, high harmonic generation (HHG) using a gas jet has been shown to be dependent on the position of the jet with respect to the focus along the laser axis [59]. This chapter discusses the result of focusing a highly intense ultrashort pulse laser at different points along the jet flow axis of an argon gas jet.

3.1.1 Motivation

In order to increase the extreme-ultraviolet (XUV) flux needed for successful imaging, it is necessary to understand the structure of the gas region from which HHG is occurring. Gas jets used as sources for the generation of high harmonics have a complex 3-dimensional density and velocity profile [80,81]. Due to the dependence of HHG on the density of the gas, the harmonic output will therefore be different depending on the position of the focus within the jet. In addition, the variation in the density of the jet structure could potentially enable a versatile method of quasi-phase matching to increase the harmonic flux.

Many experiments have been done using light to study gas jets. These include experiments using laser induced fluorescence [82], Thomson and Rayleigh scattering [83], and linear Raman spectroscopy [84] to develop temperature and density maps of free jet expansion. In the work described here, the properties of an argon gas jet are determined by focusing a highly intense ultrashort pulsed laser into various regions within the jet and imaging the emitted fluorescence from the gas. In doing so, an understanding of the jet's structure enables work in exploring its influence on XUV output and allows the maximisation of XUV flux from the source.

3.2 Investigating an Argon Gas Jet using a Femtosecond Laser

3.2.1 Free Jet Expansion

When gas in a nozzle is at a pressure higher than the background into which it is expanding, the jet expands rapidly, creating a shock wave known as the Mach disc. As such, regions of high and low velocities are present within the jet, with velocities of *Mach number* (M) $\gg 1$ present after the exit in a region known as the zone of silence and velocities $M < 1$ present at the Mach disc shock wave (see Fig. 3.1). The Mach disc is the densest region of the jet, while the zone of silence is the least dense region. There is also a barrel shock present around the zone of silence, which is created when the expanding gas collides with the background gas. In this region, the velocities of the gas particles are $M > 1$. The position of the Mach disc along the centreline (the axis along the centre of the nozzle and jet flow) for a circular nozzle is determined by,

$$X_M = 0.67d(P_0/P_b)^{1/2} \tag{3.1}$$

where d is the diameter of the jet nozzle, P_0 is the input pressure in the nozzle and P_b is the ambient background pressure around the jet [80]. If the ratio of the input pressure and background pressure is high enough, additional expansion and compression regions may be formed further down the jet.

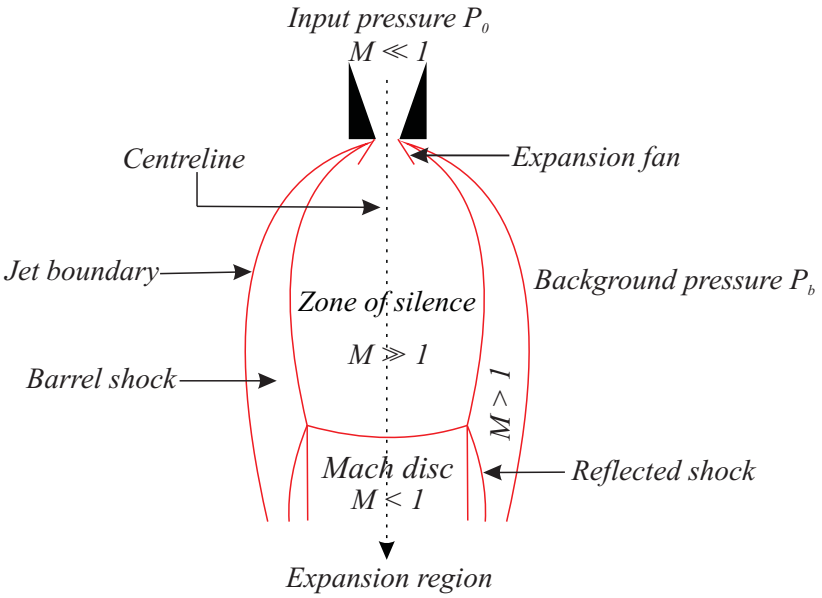

Figure 3.1: Diagram of free jet expansion from a nozzle.

Much work has gone into studying free jets [85], with solutions able to predict the general form of boundaries and other structures; though due to the complexity of jets, only approximate solutions exist. The dynamics of the jet are sensitive to pressure, as well as the type of gas (i.e. monotonic or diatomic etc.) and temperature. Several important parameters of the jet, such as the Mach disc to jet nozzle distance and the velocity of the gas in the zone of silence, can be calculated.

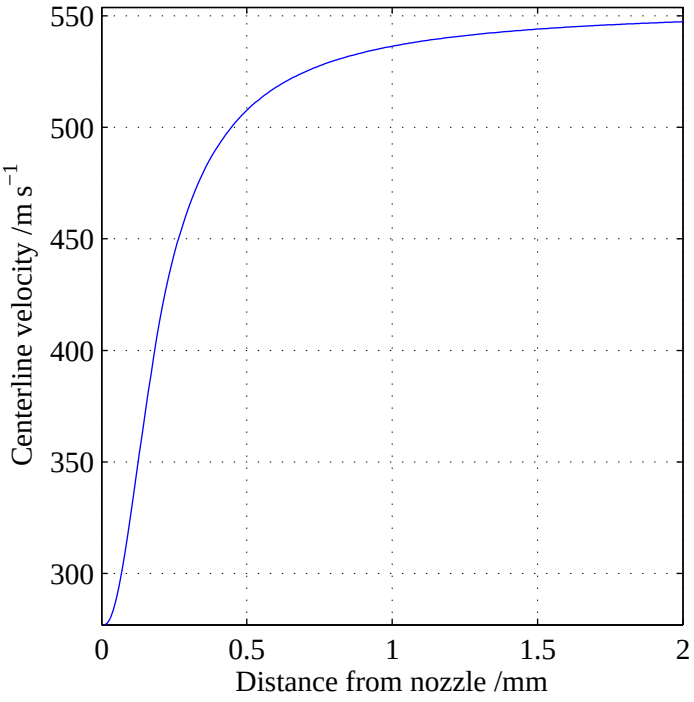

Figure 3.2: Centreline velocity of gas particles in an argon gas jet as a function of distance from a 300 μm diameter nozzle. The presence of the Mach disc is not taken into account in the calculation. The data are calculated using Equation 3.2.

The velocity as a function of distance from the jet nozzle along the centreline can be determined by [86],

$$V = M\sqrt{\frac{\gamma R T_0}{W}}\left(1+\frac{\gamma-1}{2}M^2\right)^{-\frac{1}{2}} \tag{3.2}$$

where W is the molar average molecular weight of the gas, R the gas constant, T_0 is the temperature of the gas, γ is a constant dependent on the type of gas species used and M, as mentioned already, is the Mach number. The Mach number is calculated using [86],

$$M = \left(\frac{x}{d}\right)^{(\gamma-1)/j}\left[C_1 + \frac{C_2}{\left(\frac{x}{d}\right)} + \frac{C_3}{\left(\frac{x}{d}\right)^2} + \frac{C_4}{\left(\frac{x}{d}\right)^3}\right];\quad \frac{x}{d} > 0.5$$

$$M = 1.0 + A\left(\frac{x}{d}\right)^2 + B\left(\frac{x}{d}\right)^3;\quad 0 < \frac{x}{d} < 1.0; \tag{3.3}$$

Here, *A*, *B*, *C* and *D* are all constants depending on the type of gas species used and *j* is an integer that depends on the number of spatial dimensions considered (see Scoles [86] for values).

As seen in Fig. 3.2, for free jet expansion of argon gas from a 300 μm diameter hole, the velocity of the gas within the zone of silence can increase to over 500 m s^{-1}. Note that the position and effect of the Mach disc at the end of the zone of silence is not taken into account in the calculation, and so the velocity is always increasing with distance. The maximum velocity achieved will be limited by the presence of the Mach disc and is therefore dependent on the input pressure – since input pressure affects the position of the Mach disc.

In the work described in this thesis, the important properties of a gas jet are the Mach disc and zone of silence. Since the Mach disc and zone of silence are significantly different in density, when the laser is focused into these regions, they will have a different effect on the density dependent HHG. The velocity of the particles is important when viewing the geometry. This is because the observed spatial position of any fluorescence created during HHG will vary depending on the initial and subsequent velocity of the fluorescing atoms and ions within the jet.

3.2.2 Experimental Setup

In the experimental setup, a 790 nm, 1 mJ, 1 kHz, 40 fs pulsed laser is focused using a 50 cm lens into an aluminium cubed cell with sides 2 cm in length. Figure 3.3 is a photograph of the cell used to create an argon gas jet, while Fig. 3.4 is a schematic showing the way in which the cell is designed to work. Two sides of the cell are made of colourless acrylic to allow observation of the generation region. Argon gas was used as the nonlinear medium for HHG since strong visible emission lines from excited argon atoms and ions enable observation of the generation region. A 1024 x 1024 pixel charged coupled device (CCD) camera is used to image the geometry. The argon gas, supplied into the top of the cell, is passed out the base of the cell through a 300 μm diameter hole in a 1.5 cm square, 2 mm

thick aluminium plate to create a gas jet. The base of the plate is 250 μm above the laser axis so that the laser focus passes through the jet and generates high harmonics.

The entrance and exit holes for the laser beam are 500 μm in diameter – large enough to avoid clipping of the beam but small enough to restrict gas flow and avoid overloading of the turbomolecular pumps at high input pressures.

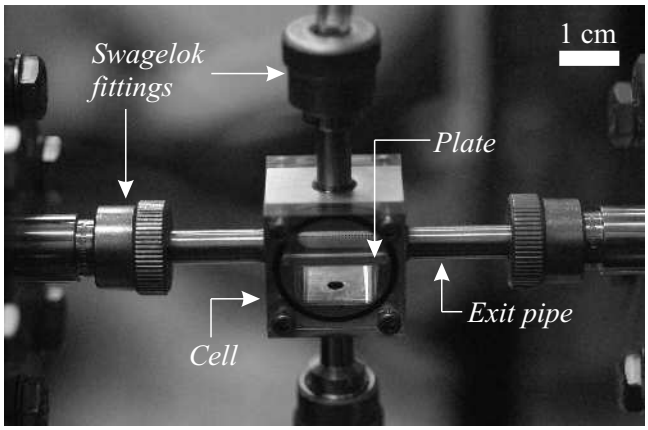

Figure 3.3: Photograph of cell in vacuum setup.

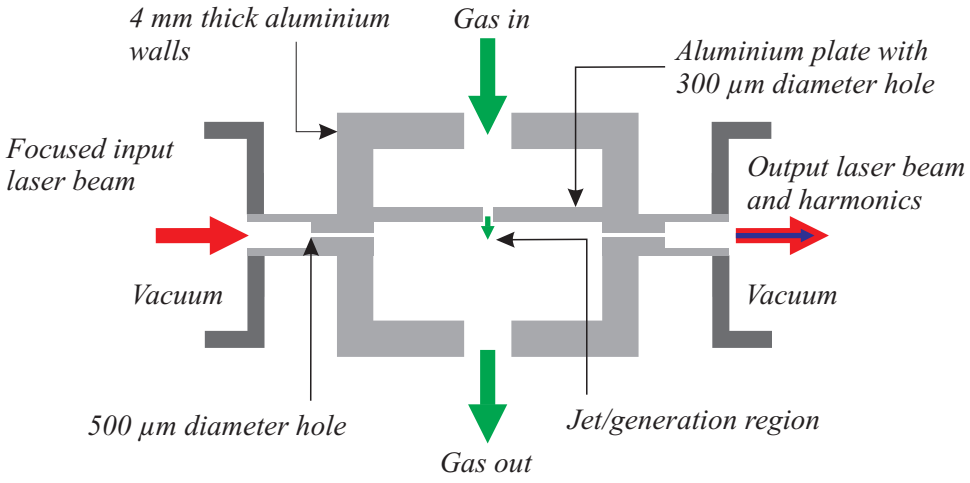

Figure 3.4: Side cross-section schematic of the configuration of the cell used in the generation of XUV radiation. Gas is pumped through a 300 μm hole in a plate to produce a gas jet. Laser is focused into the jet using a 50 cm focal length lens.

3.2.3 Spatial Distribution of Fluorescence

When an intense ultrashort pulsed laser is focused into a gas, highly excited states of atoms and ions can be created. A photon will be emitted when the excited electron undergoes

transition to a lower energy state. Depending on the gas and states created, fluorescence of different lifetimes and wavelengths will be observed. In the case of excited neutral and ionized argon, emitted wavelengths include 420 nm and 488 nm which have lifetimes ranging from microseconds down to nanoseconds, respectively.

Figure 3.5 shows the spatial distribution of the fluorescence inside the cell viewed side-on (perpendicular to the laser axis and jet flow axis) when the input pressure of gas is 200 mbar. The image was captured using a CCD camera with a 488 nm band-pass filter and a 600 nm short-pass filter. The integration time was 5 seconds and the laser is focused from the left into the centre of the cell. The 0 mm height in this image and subsequent images of the jet throughout this chapter represents the level of the nozzle exit. This image and other images of the generation region throughout this thesis are displayed using a false colourmap.

Fluorescence is present along the laser axis and extends several millimetres below the nozzle exit. Due to movement of the fluorescing atoms and ions within the jet, structure of the jet is observed. Evident from Fig. 3.5 is the Mach disc and barrel shock – visible as regions of high intensity which surround a region of low intensity corresponding to the zone of silence. The fluorescence along the laser axis either side of the jet is the result of excitation and ionization of gas that is not removed from the cell because of a low pumping throughput.

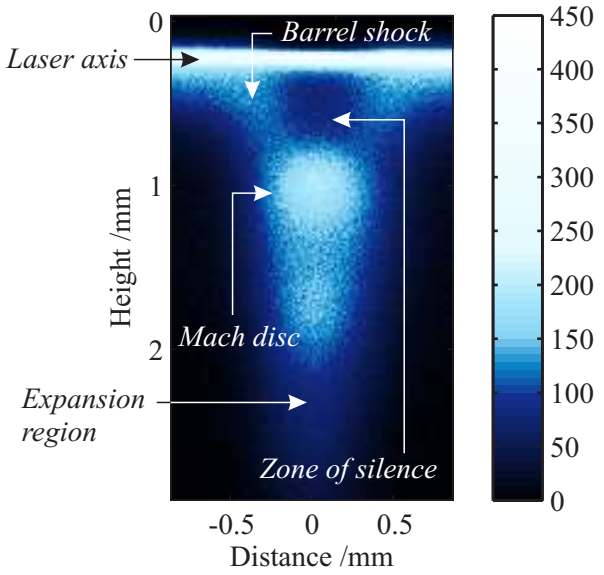

Figure 3.5: Spatial intensity of the fluorescence inside the cell viewed side-on using a 488 nm band-pass filter and a 600 nm short-pass filter for a gas input pressure of 200 mbar. The integration time of the image is 5 seconds. The colour scale is saturated to aid in viewing of the jet structure.

Images of the jet taken at other pressures are shown in Fig. 3.6. From the images, it can be seen that as the pressure increases, the Mach disc moves further away from the jet nozzle. This is as expected from the theoretical model of a gas jet.

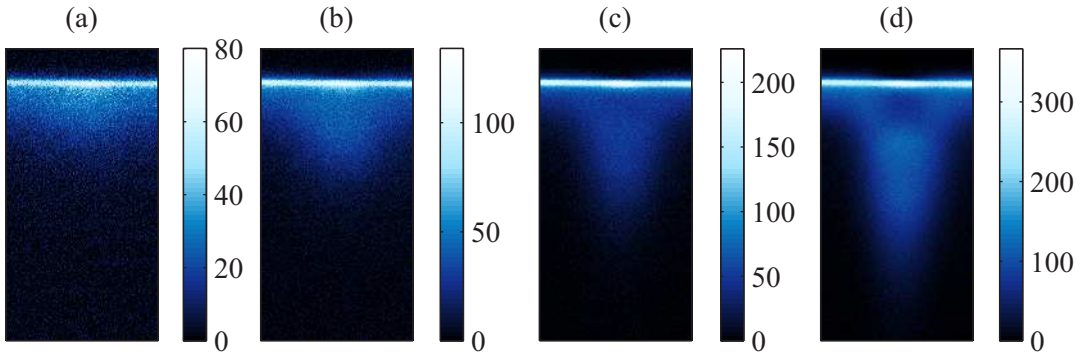

Figure 3.6: Spatial intensity of the fluorescence inside the cell viewed side-on using a 488 nm band-pass filter and a 600 nm short-pass filter for gas input pressures of (a) 10 mbar, (b) 50 mbar, (c) 75 mbar and (d) 100 mbar. The integration time for each image is 5 seconds.

The variation in the structure of the jet along its centreline is apparent in Fig. 3.7. The plots are a single pixel slice of the intensity of fluorescence down the centreline of the jet at an input pressure of 10, 50, 100 and 200 mbar.

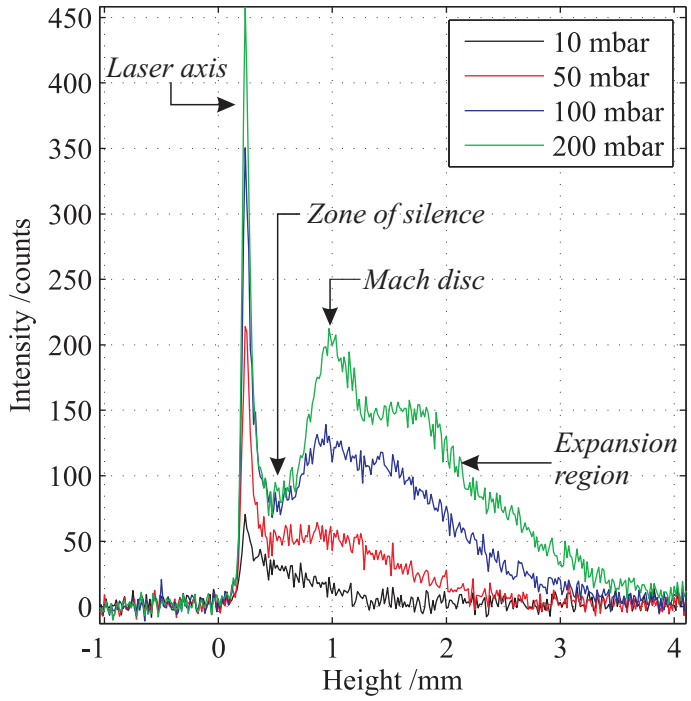

Figure 3.7: Single pixel slice of the intensity of fluorescence along the centreline of the jet for gas input pressures of 10, 50, 100 and 200 mbar.

Labelled on the figure are regions corresponding to the laser axis, zone of silence, Mach disc and expansion region. The peak of the intensity of fluorescence is along the laser axis, indicating that the dominant fluorescence is short lived since the atom and ions have not travelled significantly far during fluorescence, even though are moving at high velocity (~ 500 m s^{-1}). Since fluorescence is also observed several millimetres down the jet, the observed fluorescence must also include emission from atoms or ions in longer lived excited states.

To further understand the fluorescence and jet structure, the laser was focused at two other positions along the centreline of the jet so that initial gas velocity and density conditions were different. Figure 3.8 shows the observed fluorescence when focusing the laser 950 µm and 1650 µm directly below the exit of the jet nozzle. For comparison, the 250 µm image is also displayed in the figure. Labelled on this image using dashed lines are the two other heights that the laser is focused (Fig. 3.8 (a)). In Fig. 3.8, the laser is exciting atoms and ions in different regions of the jet and so the subsequent fluorescence intensity is different for all three images. At a height of 250 µm, the laser is focused into the zone of silence, however at 950 µm, the laser is focused into the Mach disc and at 1650 µm, the laser is focused into the expansion region.

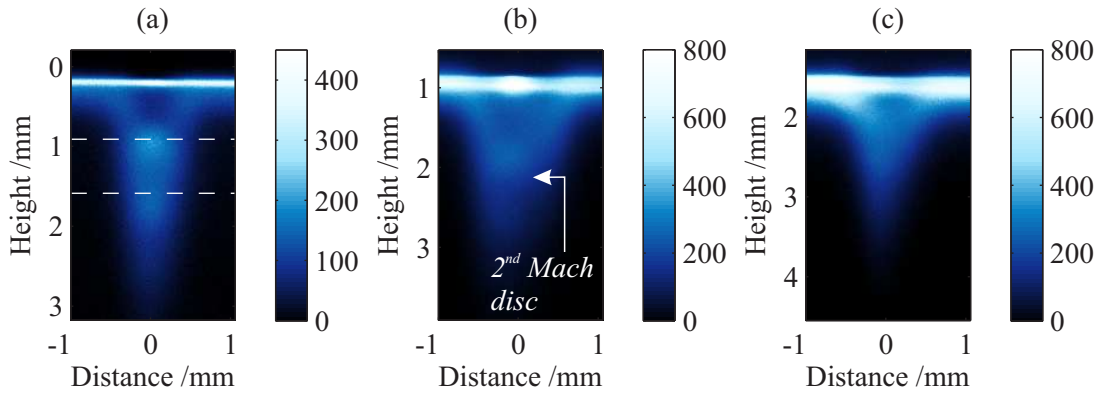

Figure 3.8: Spatial intensity of the fluorescence inside the cell viewed side-on using a 488 nm band-pass filter and a 600 nm short-pass filter for jet nozzle-laser separations of (a) 250 µm, (b) 950 µm and (c) 1650 µm and gas input pressure of 200 mbar. The dashed lines in (a) represent the two other heights, (b) and (c), that the laser is focused. The integration time for each image is 5 seconds.

A single pixel slice of intensity of the fluorescence along the jet's centreline for the three heights is displayed in Fig. 3.9. The peak fluorescence for an input pressure 200 mbar occurs at 950 µm, since at this pressure and distance the laser is focused into the Mach disc where there is a high particle density. It is also possible to see a secondary shock at 2 mm in

Fig. 3.8 (b) – demonstrating the complexity of structure the gas jet. From Fig. 3.8, it is evident that the intensity of fluorescence is greater when the laser is focused into the expansion region than when it is focused into the zone of silence. This indicates a higher particle density in the expansion region than the zone of silence in this geometry and demonstrates the variation in density of the jet along its centreline.

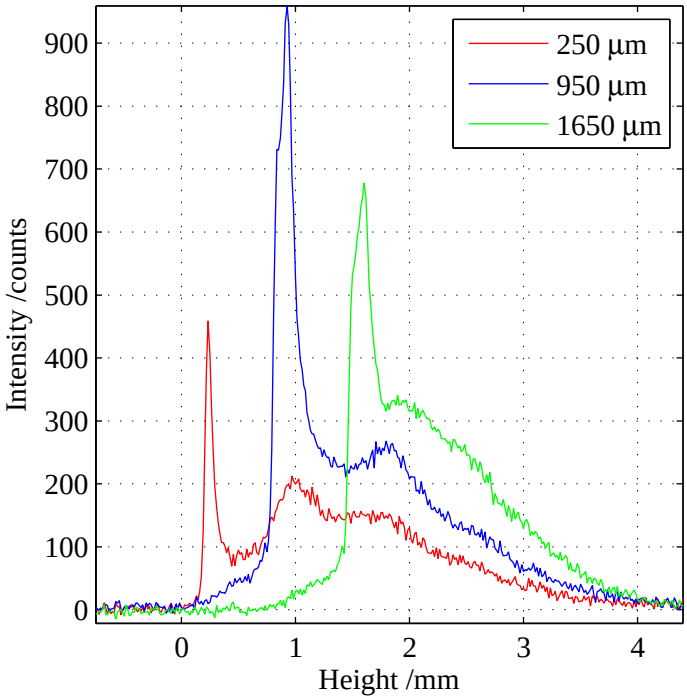

Figure 3.9: Single pixel slice of the intensity of fluorescence along the centreline of the jet for a gas input pressure of 200 mbar and jet nozzle-laser separation of 250, 950 and 1650 µm.

Although the jet structure is visible when using a 488 nm band-pass filter, by using a filter with a different band-pass wavelength, fluorescence that has different lifetimes will be observed. By observing fluorescence dominated by a longer decay, regions further away from the laser axis should be more visible and will thus aid in the understanding of the generation region. Figure 3.10 displays the observed spatial intensity of fluorescence when using a 420 nm band-pass filter instead of a 488 nm band-pass filter[3]. The image was taken when the input pressure of gas was 200 mbar and the jet nozzle-laser separation was 250 µm. In this image, the Mach disc is much more visible and there is a dip in the intensity of the fluorescence along the laser axis. This dip is not observed when using a 488 nm band-pass filter (see Fig. 3.5). This suggests that by the time the majority of atoms and ions have

[3] Note that a 600 nm short-pass filter was not used with the 420 nm band-pass filter.

fluoresced, they have already moved further down the jet. The observed fluorescence along the laser axis is also much broader spatially due to the atoms and ions having diffused further by the time they have fluoresced.

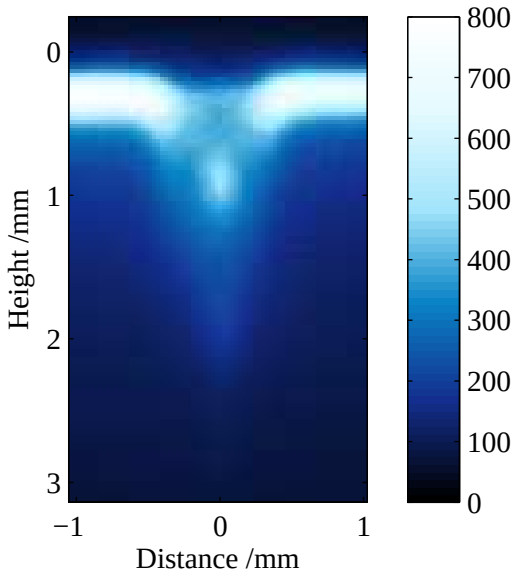

Figure 3.10: Spatial intensity of the fluorescence inside the cell viewed side-on using a 420 nm band-pass filter for a gas input pressure of 200 mbar. The integration time for the image is 5 seconds.

On comparing the fluorescence recorded using a 420 nm band-pass filter (Fig 3.10) to that recorded using a 488 nm band-pass filter (Fig. 3.8 (a)), the Mach disc is in the same position – confirming that what is being observed is structure of the jet.

3.2.4 Temporal Distribution of Fluorescence

To verify that the observed emission consists of fluorescence with different lifetimes, the fluorescence from the jet as a function of time was recorded. Figure 3.11 (a) shows the fluorescence as a function of time over a period of 10 μs for gas input pressures of 1, 10, 50, 100 and 200 mbar. The nozzle exit was 250 μm above the laser axis. The filter used in front of the photomultiplier was a 488 nm band-pass filter while the signal collection was gated for a period of 100 ns and integrated over 1000 shots. It is evident from the plots, that the fluorescence is not just a simple exponential decay but has multiple rates of decay.

Indeed, from Fig. 3.11 (b), which shows the fluorescence at 1 mbar input pressure over a period of 1 μs using a 5 ns gating period (for higher temporal resolution to determine shorter decays), a ~ 10 ns decay is observed before the fluorescence intensity increases again

due to the decay of longer lived states. These results indicate that many transitions must be occurring to produce the temporal distribution of fluorescence that is observed.

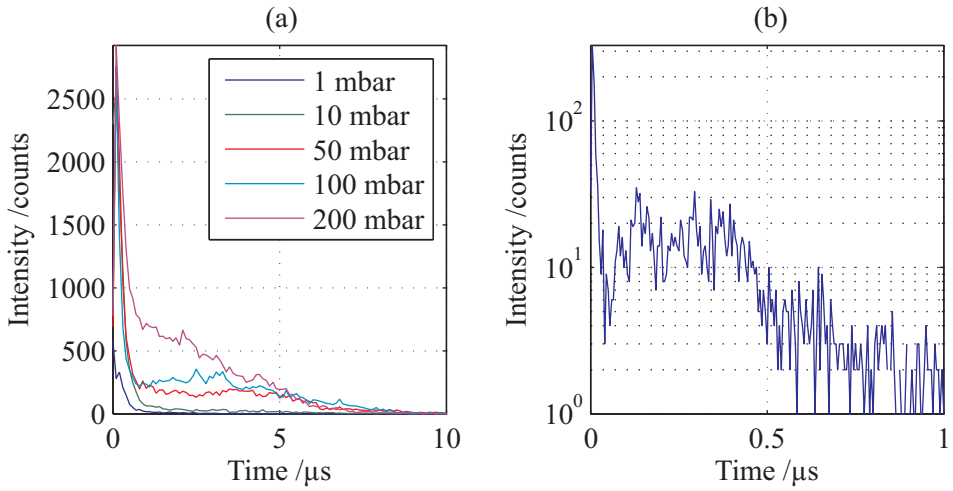

Figure 3.11: (a) Intensity of fluorescence as a function of time over a period of 10 μs for gas input pressures of 1, 10, 50, 100 and 200 mbar. (b) Intensity of fluorescence as a function of time over a period of 1 μs for a gas input pressure of 1 mbar. The data are displayed on a log_{10} scale.

3.2.5 Mechanism of Fluorescence

The multi-photon excitation and tunnelling ionization of the argon in the high intensity laser field will create a population of excited states of argon atoms and ions (Ar* and Ar^+*). States with energy just below that of the first ionization potential of argon (15.8 eV), as well as those which converge on ionizations are likely to be created,

$$Ar + h\nu \rightarrow Ar^*, Ar^{+}* \text{ or } Ar^{**} \text{ (metastable highly excited Ar)} \quad (3.4)$$

Many of the excited states will decay via fast radiative processes. In the case of Ar^+, some decays are relatively short,

$$Ar^{+}* (4p) \rightarrow Ar^{+}* (4s) + h\nu \text{ (488 nm)}, \tau \sim 10 \text{ ns} \quad (3.5)$$

This 4s-4p emission is observed in the experiment as the ~ 10 ns decay seen in Fig. 3.11 (b) and is the dominant observed fluorescence when using a 488 nm band-pass filter. The short decay time of the fluorescence means that the ions will travel only ~ 5 μm during fluorescence within the zone of silence.

The dominant observed fluorescence when using a 420 nm band-pass filter results from emission of Ar*,

$$Ar^* (5p) \rightarrow Ar^* (4s) + h\nu\ (420\ nm),\ \tau \sim 1\ \mu s \tag{3.6}$$

As discussed, in Fig. 3.10 there is a dip in the intensity of fluorescence observed at the centre of the jet along the laser axis and the fluorescence intensity is greater further down the jet. This is due to the state of Ar* (4s-5p) with a lifetime of ~ 1 μs being the most dominant; by the time the majority of the excited atoms have fluoresced, they have travelled to the Mach disc.

Although the 420 nm (4s-5p) and 488 nm (4s-4p) emission lines are the most dominant [87], the filters have a FWHM band-pass of ~ 10 nm and so fluorescence from other transitions will also be recorded on the images. For example, long-lived states ($\gtrsim$ 1 μs) such as 4p-3d at 490 nm will contribute to the overall fluorescence observed when using the 488 nm band-pass filter. This is why fluorescence is observed both along the laser line and at the Mach disc of the jet when using a 488 nm band-pass filter. Likewise, other states, including short-lived states emitting at around 420 nm, will also contribute to the observed fluorescence when using the 420 nm band-pass filter.

In addition to the states described so far, the promotion of electrons to states other than the outer result in Rydberg states with an excited core configuration. Any of these Rydberg states which have a high orbital angular momentum can be very long-lived, with lifetimes reaching 10 μs [87]. At higher pressures, long-lived doubly-excited argon Rydberg states can also undergo Penning ionization [88]. In this process, metastable Ar** can collide with argon atoms in the jet (particularly in the regions of higher density) and produce Ar^+*,

$$Ar^{**} + Ar \rightarrow Ar^{+*} + Ar + e^- \tag{3.7}$$

The Ar^+* will eventually decay to produce the 488 nm emission. This effect can be observed in the fluorescence decay at 200 mbar in Fig. 3.11 (a). The structure of the decay over the first 2 μs is slightly different compared to that at other pressures, since at this pressure, the jet structure is more prominent and the number of collisions has increased. Some of the Ar** can also be produced from long-lived doubly excited argon Rydberg states undergoing autoionization [89],

$$Ar^{**} \rightarrow Ar^{+*} + e^- \tag{3.8}$$

This process is spontaneous and can occur at both high and low pressures.

3.2.6 Discussion

Since the atoms and ions fluoresce after moving within the jet, the images are a convolution of the particle density, particle velocity, fluorescence lifetime and rate constant for decay from excited ion to excited atom. The intensity dependence of the fluorescence on the particle number means that the data obtained can be used to estimate the pressure in the jet. Using a method proposed by Hirakawa *et al.* [90], the pressure is estimated by comparing the intensity of fluorescence from the argon gas jet to that of an argon-filled cell at known pressure. At 200 mbar input pressure, the pressure of the Mach disc is estimated to be ~ 13 mbar, while the pressure in the zone of silence is estimated to be ~ 6 mbar.

The observed FWHM thickness of the Mach disc from Fig. 3.10 is ~ 300 μm, which is in agreement to the calculated value of ~ 375 μm, given by 0.5 X_M ± 25 % [86]. In addition, the peak velocity in the zone of silence (estimated from the dominant decay time and X_M) for an input pressure of 200 mbar is estimated to be 420 m s^{-1}, which is comparable to a calculated value of ~ 500 m s^{-1}.

Variation in the gas jet structure should also be observed when using other gases as well as gas mixtures. Due to the variation in gas jet structure, the conditions in which HHG is occurring will therefore vary depending on where the laser is focused within the jet. The output XUV signal from focusing the laser into various points along the centerline of an argon gas jet is discussed in the next section.

3.3 XUV Signal from an Argon Gas Jet

In order to understand HHG from different points along the centreline of the jet so that output XUV flux can be maximised, it is necessary to improve the setup so that the features of the jet are more prominent and clearer to interpret. A nozzle with a greater diameter was therefore created so that a larger gas jet could be produced. In addition, a larger chamber suitable for high pumping throughput was constructed to reduce stagnant gas that will, through both absorption and contribution of XUV signal, reduce any potential variation in the observed harmonic spectrum whilst varying the position of the laser focus within the jet.

3.3.1 Experimental Setup

Using a 50 cm focal length lens, the laser beam is focused into a small chamber that is 4 cm in diameter and 15 cm high (see Fig. 3.12). A 4 cm diameter, 1 mm thick, fused silica viewing window is attached to the side of the chamber so that the jet nozzle and the generation region can be monitored. Argon gas is passed through a 500 μm inner diameter

glass nozzle that is suspended inside the chamber. The nozzle can be moved vertically so that the position of the laser focus along the centreline of the jet can be varied.

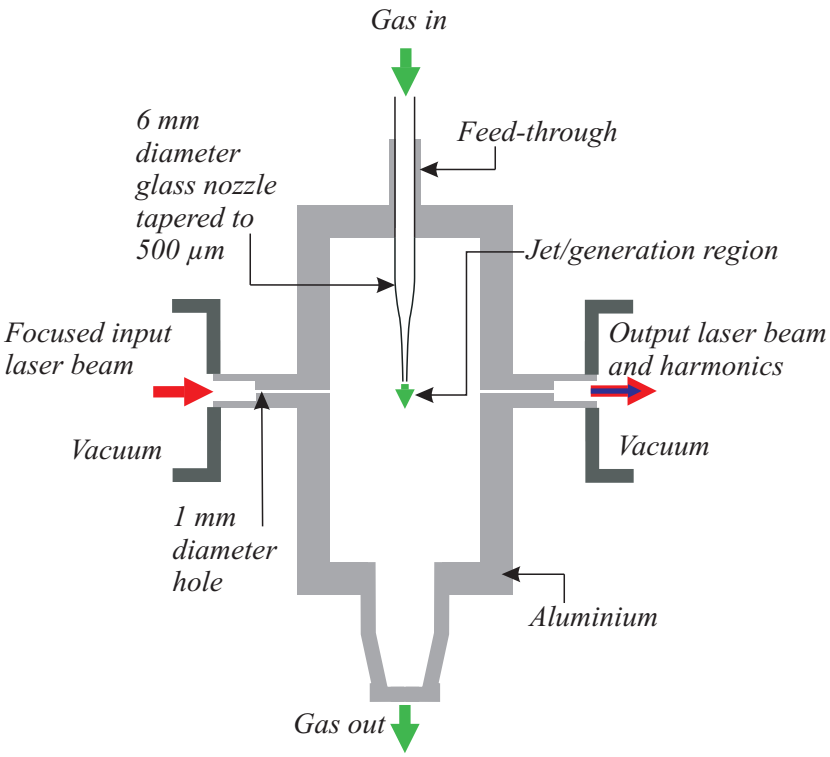

Figure 3.12: Side cross-section schematic of the configuration of the generation setup. The jet nozzle has a diameter of 500 µm. Using a 50 cm focal length lens, the laser is focused into a region below the exit of the nozzle where a gas jet is formed.

Since the nozzle is larger than that in the previous section, the throughput of gas is greater for the same input pressure. In order to not to overload the turbomolecular pumps, it was not possible to achieve as high input pressure as before. The maximum input pressure used was 125 mbar. For reference, the end of the jet nozzle, pulled to an inner diameter of 500 µm and outer diameter of 900 µm, is shown in the photograph in Fig. 3.13. The end is circular and so a cylindrically symmetric jet profile observed in the previous section can be expected from the jet expansion of gas from the nozzle.

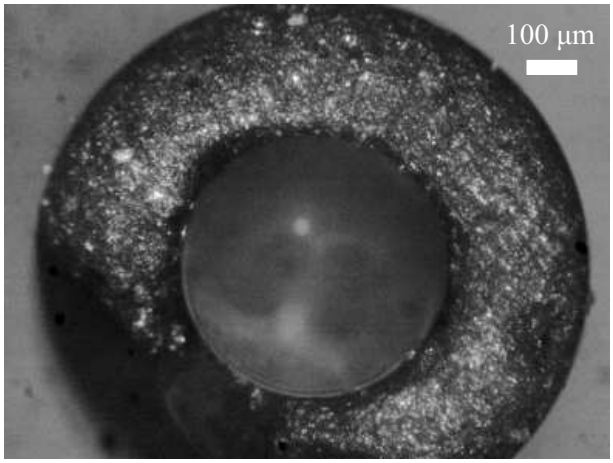

Figure 3.13: Photograph of the glass nozzle exit.

3.3.2 Spatial Distribution of Fluorescence

To determine the region along the centreline of the jet that produces the maximum output XUV flux, the generation region needs to be monitored. By observing the fluorescence emitted when the laser is focused into the jet, the density profile of the generation region can be observed and the position of the laser focus with respect to the jet can be established.

Figure 3.14 shows the spatial intensity of the fluorescence from an argon gas jet at an input pressure of 100 mbar. This image was taken over an integration time of 5 seconds using a CCD camera with a 420 nm band-pass filter. The reason for using this filter was that, as demonstrated previously, the structure of the jet is more visible due to the longer decay time of the dominant fluorescence. Again, the dominant emission is produced from excited argon (Ar* (4s-5p)). In the image, the axis of the jet flow is vertically downward and the laser is propagating from left to right with the laser focus set at 1 mm below the nozzle exit.

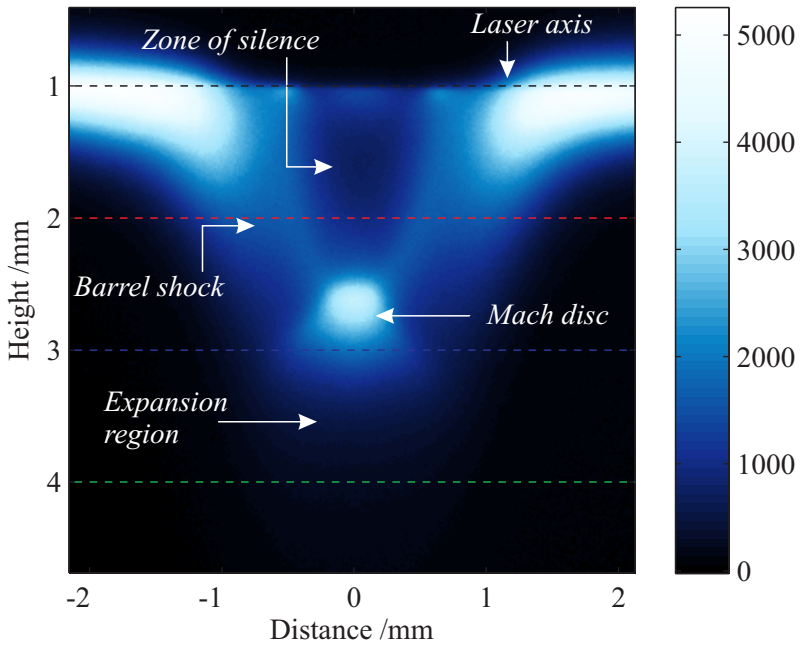

Figure 3.14: Spatial intensity of the fluorescence inside the chamber viewed side-on using a 420 nm band-pass filter for a gas input pressure of 100 mbar. The dashed lines indicate the four jet nozzle-laser distances. The integration time for the image is 5 seconds.

Upon looking at Fig. 3.14, it is clear that the jet structure is much more visible than with the previous setup. As expected, the Mach disc is further from the nozzle for the same input pressure.

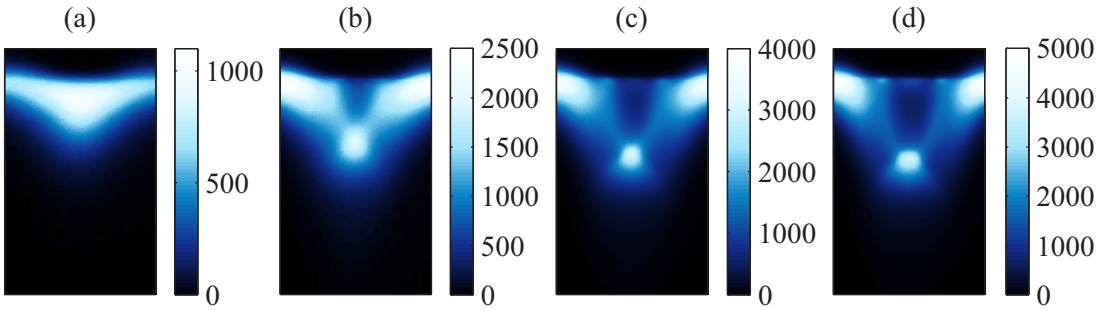

Figure 3.15: Spatial intensity of the fluorescence inside the chamber viewed side-on at (a) 25 mbar, (b) 50 mbar, (c) 75 mbar and (d) 100 mbar gas input pressure using a 420 nm band-pass filter. The integration time for each image is 5 seconds.

Again, as the input pressure is increased, the jet structure becomes more prominent and the Mach disc moves further away from the jet nozzle (see Fig. 3.15).

At input pressures of 50 mbar or higher, it is clear that by varying the position of the jet nozzle with respect to the laser over a distance of ~ 3 mm, the focused laser will be encountering a significantly different region of gas density. At 100 mbar (see Fig. 3.14), when the laser is focused at both 1 mm and 2 mm below the nozzle exit, the laser focus passes through the zone of silence. In this region, the gas has a high velocity ($M \gg 1$) and low density. At 3 mm below the nozzle, the laser focus passes through the Mach disc shock which is a region of low velocity ($M < 1$) and high particle concentration. At 4 mm, the laser passes through the expansion region where the particles have velocities of $M > 1$. As seen from the side image, the fluorescence in regions with higher velocity and low density is less intense.

The consequence on the spatial intensity of fluorescence when focusing at the other heights is presented in Fig. 3.16. When the laser is focused at different points along the jet flow axis, not only is the observed fluorescence different along the laser axis (where HHG occurs), but so is the fluorescence further down the jet. This is because the initial conditions (gas velocity and density) for the excitation and ionization are different. For jet nozzle-laser distances of 1 mm and 2 mm, the laser is focused into the zone of silence where the density is low and so there is a dip in intensity of florescence along the laser axis. The difference in the scale and shape of the dip is due to the complex profile of the zone of silence.

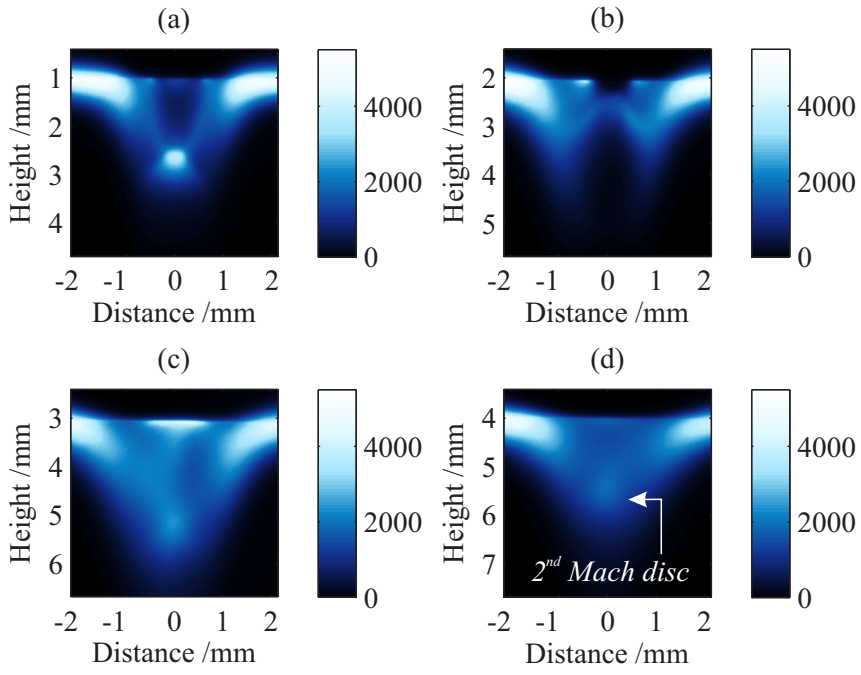

Figure 3.16: Spatial intensity of the fluorescence inside the chamber viewed side on at 100 mbar input pressure for four jet nozzle-laser distances of (a) 1 mm, (b) 2 mm, (c) 3 mm and (d) 4 mm. The integration time for each image is 5 seconds.

At 3 mm, because the laser is focused into the Mach disc where the density is relatively high compared to other regions, the fluorescence intensity along the laser axis is high. The fluorescence from the Mach disc is approximately four times greater than the zone of silence. Again, the pressure in the argon gas jet is estimated by comparing the intensity of fluorescence from the argon gas jet to that of an argon-filled cell at known pressure. At 100 mbar input pressure, the pressure in the Mach disc is estimated to be ~ 25 mbar, while the pressure in the zone of silence is estimated to be ~ 6 mbar. From Fig. 3.16 (d), the intensity of fluorescence and therefore density along the laser axis at 4 mm (the expansion region) is at least half that observed from the Mach disc. As a point of note, a potential secondary Mach disc is seen at ~ 5.5 mm in both Fig. 3.16 (c) and Fig. 3.16 (d).

From the observed fluorescence, it is clear that by focusing the laser into these four different levels of the jet, HHG will occur from regions of different density

3.3.3 XUV Spectrum

Figure 3.17 shows the spectra at four different jet nozzle-laser distances for input pressures of 0-125 mbar. The spectra were recorded using an XUV spectrometer. Although the spectrometer will record the spatial variation in the spectrum (radial variation if beam is centred on slit, as in this work), in this instance, the spectrum has been spatially binned for ease of comparison. The integration time for obtaining each spectrum was 300 seconds (though the data in the plots have been normalised to 1 second for ease of quantifying). In all the plots, there is a similar number of harmonics. In addition, the intensity of the harmonics increases with pressure – suggesting that the generation is not limited by phase matching for gas pressures used here. The highest flux attainable for all pressures is at a jet nozzle-laser distance of 3 mm.

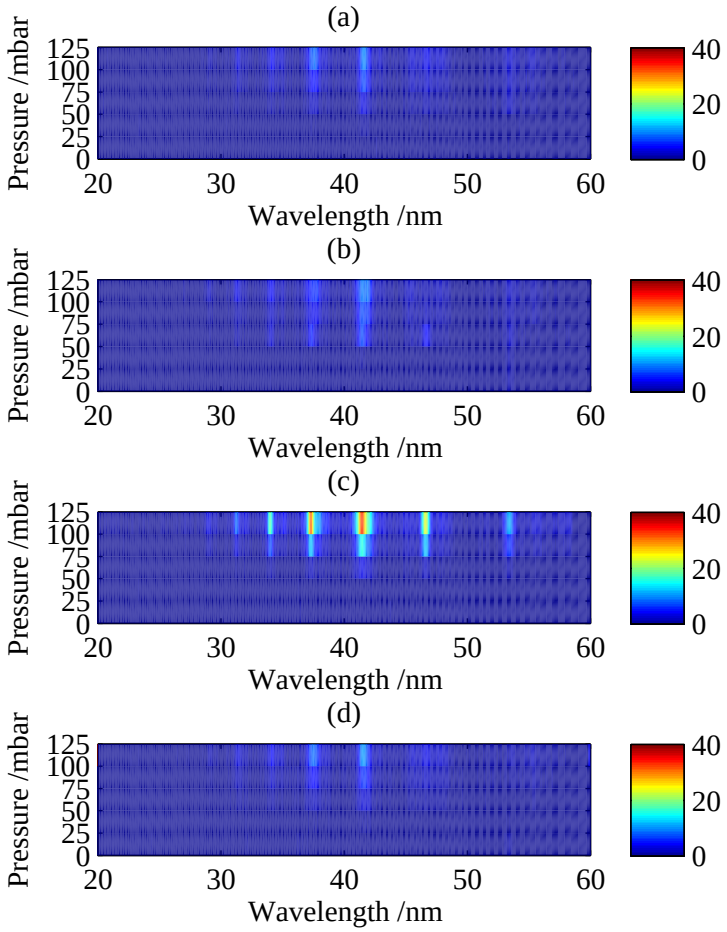

Figure 3.17: Intensity of the harmonic spectrum between 20 and 60 nm for four jet nozzle-laser distances (a) 1 mm, (b) 2 mm, (c) 3 mm and (d) 4 mm as a function of input pressure. The data have been normalised to 1 second.

Figure 3.18 compares the XUV spectrum obtained for a gas input pressure of 100 mbar when the jet nozzle-laser distance is 1, 2, 3 and 4 mm. For most harmonics, the intensity at 3 mm compared with the other positions is about four times greater. It is at this jet nozzle-laser distance that the laser is focused into the Mach disc.

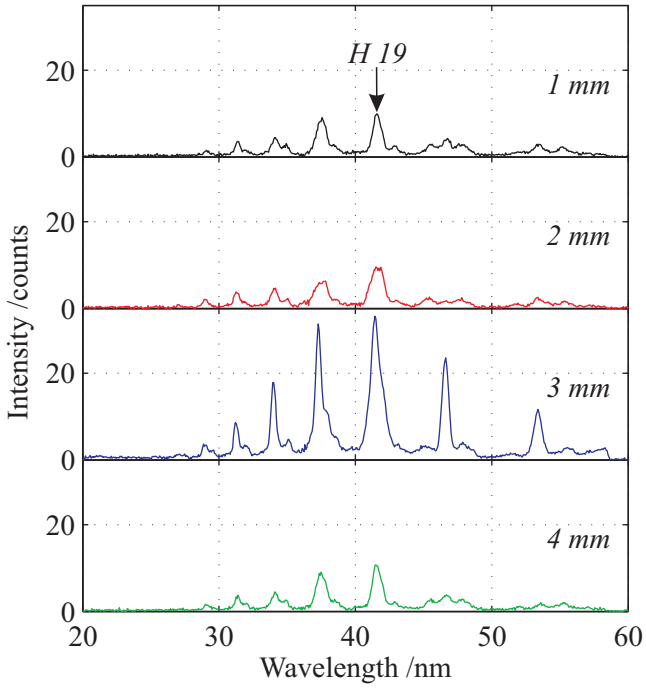

Figure 3.18: Intensity of the harmonic spectrum between 20 and 60 nm at 100 mbar for four jet nozzle-laser distances 1, 2, 3 and 4 mm. The data have been normalised to 1 second.

The harmonic with highest intensity at all jet nozzle-laser distances is the 19th harmonic (H 19). The yield for this harmonic is plotted in Fig. 3.19 as a function of pressure for all four jet nozzle-laser distances. The difference in intensity of the harmonic between the 3 mm jet nozzle-laser distance and the other distances is greater at higher input pressures when the jet structure is significantly formed. It is apparent from both theoretical calculation and experimental observation, that the Mach disc is not at a distance of 3 mm from the nozzle until the input pressure is at least 75 mbar. Not only is the Mach disc present at 3 mm for an input pressure of 100 mbar, but due to the higher input pressure, the density of the Mach disc is greater. Due to the dependence of HHG on gas density, the harmonic yield is greatest when the laser is focused into the Mach disc.

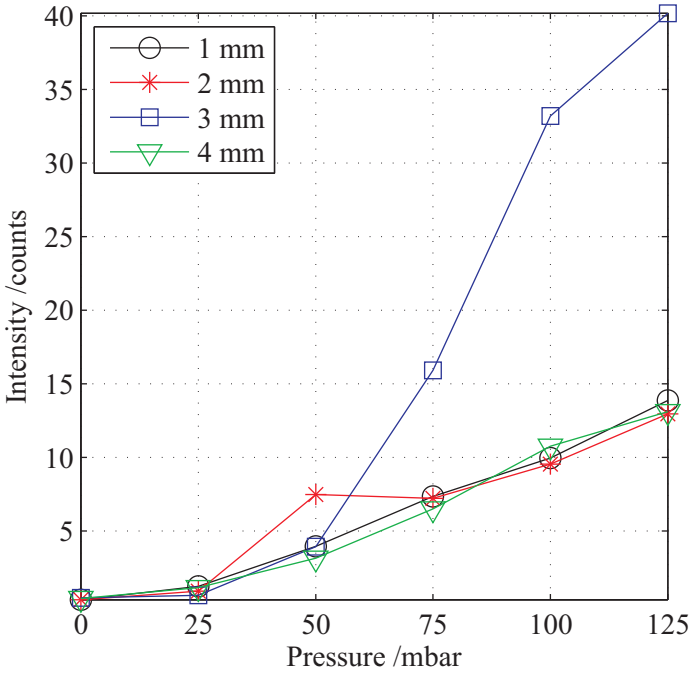

Figure 3.19: Peak intensity of the 19th harmonic as a function of pressure at jet nozzle-laser distances 1 mm (circle), 2 mm (star), 3 mm (square) and 4 mm (triangle). The data have been normalised to 1 second.

It is also evident from Fig. 3.19 that the intensity of the 19th harmonic is higher at 50 mbar than 75 mbar for a jet nozzle-laser separation of 2 mm. At 2 mm, the Mach disc is present at an input pressure of 50 mbar, but not at an input pressure of 75 mbar. This can be seen from the fluorescence images in Fig. 3.20 which show predominantly the short-lived 488 nm emission from the jet at (a) 50 mbar and (b) 75 mbar for the 2 mm jet nozzle-laser separation. There is a visible drop in fluorescence along the laser axis at 75 mbar compared to 50 mbar, indicating a region of less dense gas. Indeed, at 50 mbar the laser is focused into the Mach disc. However, at 75 mbar the laser is focused into the zone of silence and so the harmonic yield is less than at 50 mbar.

HHG will not only occur at the very focus, but either side of the jet along the laser axis within the cut-off region (the region in which the laser intensity is high enough to generate high harmonics). As such, although there is a dip in the fluorescence and therefore density at the zone of silence along the laser axis, the high density region around it, due to the barrel shock, will still contribute to the output XUV flux. Due to a similar total density in the generation region, the harmonic output from the zone of silence and expansion region is similar.

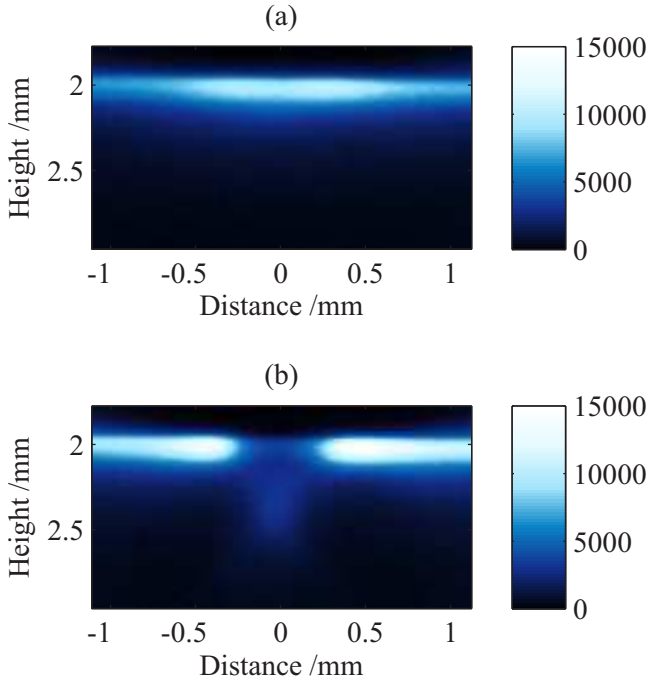

Figure 3.20: Spatial intensity of the fluorescence viewed side-on using a 488 nm band-pass filter and 600 nm short-pass filter at a jet nozzle-laser separation of 2 mm for gas input pressures of (a) 50 mbar and (b) 75 mbar. The integration time of the image is 5 seconds.

3.3.4 Phase Matching Considerations and Analysis

As long as the coherence length and the absorption length is longer than the generation region of the jet, higher intensity harmonics will be produced in regions of higher density. As discussed in Chapter 2, the buildup of the nonlinear signal through the length of the medium is determined by the phase matching between the fundamental laser and generated harmonics. The phase matching has contributions from the Gouy shift through the laser focus, the atomic phase and the refractive indices of the gas and plasma. Each of these terms contributes a wavevector mismatch, $\Delta \boldsymbol{k}$, between the fundamental and the harmonics, which leads to a coherence length, $L_{coh} = \pi/|\Delta \boldsymbol{k}|$, over which buildup of high harmonic signal will occur.

The intensity of the output of the q^{th} harmonic can be written generally as [60],

$$\left|E_q\right|^2 \approx N^2 \left|\chi_{eff}^{(q)} E_0^s\right|^2 \left(\frac{1 + e^{-2\alpha L} - 2e^{-\alpha L} cos\,\Delta \boldsymbol{k} L}{\alpha^2 + \Delta \boldsymbol{k}^2}\right) \tag{3.9}$$

where N is the number density of atoms, $\chi^{(q)}_{eff}$ is the effective nonlinear susceptibility of the q^{th} harmonic, E_0 is the input electric field, s is the effective order of the nonlinearity (~ 5), α

is the absorption coefficient and $\Delta \boldsymbol{k}$ is the total wavevector mismatch. The final bracketed term describes the contribution of phase matching to the output intensity of the q^{th} harmonic in the presence of absorption. This term reduces to $\mathrm{sinc}^2(\Delta \boldsymbol{k}L/2)$ if α is zero.

The coherence length of the 19th harmonic for long and short trajectory phase components at a pressure of 25 mbar (the pressure of the Mach disc at 100 mbar input pressure) is plotted in Fig. 3.21. The phase matching is dominated by the plasma at a beam radius of < 30 μm due to the high level of ionization occurring at the laser focus. The coherence length at the centre of the beam focus is therefore small for both long and short trajectories (see Fig. 3.21 (a) and (b), respectively), and HHG from this region will contribute almost no signal to the overall XUV yield.

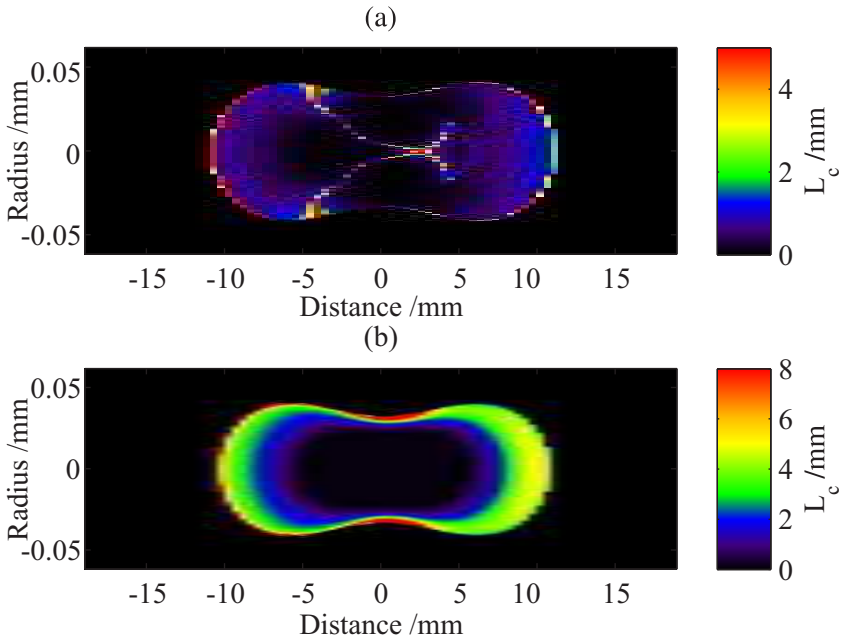

Figure 3.21: Coherence length of the 19th harmonic as a function of radius and distance along the laser propagation axis for (a) long trajectories and (b) short trajectories at a pressure of 25 mbar. The data are calculated using Equation 2.21.

When the ionization fraction is < 0.02, the contribution from the plasma index is significantly less and the gas index, atomic and Gouy phases become significant. This is the case at the laser focus for beam radii > 30 μm. For short trajectories at such radii, the coherence length for the 19th harmonic is ≥ 1 mm, which is longer than the dimensions of the Mach disc. For long trajectories, the coherence length is very short (≪ 1 mm) for the majority of the focus and will contribute significantly less high harmonic signal than short trajectories.

Since the Mach disc has a maximum dimension less than the coherence length of the short trajectories and the absorption length (L_{abs} > 1 mm at 25 mbar for H 19), the buildup of harmonic signal is not limited by the phase matching term or the absorption term in Equation 3.9 at pressures used in this work. Instead, the harmonic signal is limited by the density of gas (and also the length of the medium). This is confirmed in Fig. 3.22, which displays the intensity for the 19th harmonic as a function of pressure with a quadratic curve fitted using the 1 mm data. In regions where the jet's spatial structure does not change rapidly with pressure (i.e. at low pressures or either close to the nozzle or beyond the Mach disc), the overall quadratic dependence of harmonic output does not deviate with pressure. For regions where there is a dip in the density (and thus harmonic signal) due to the zone of silence, there is a contribution from the barrel shock and so the quadratic behaviour is maintained.

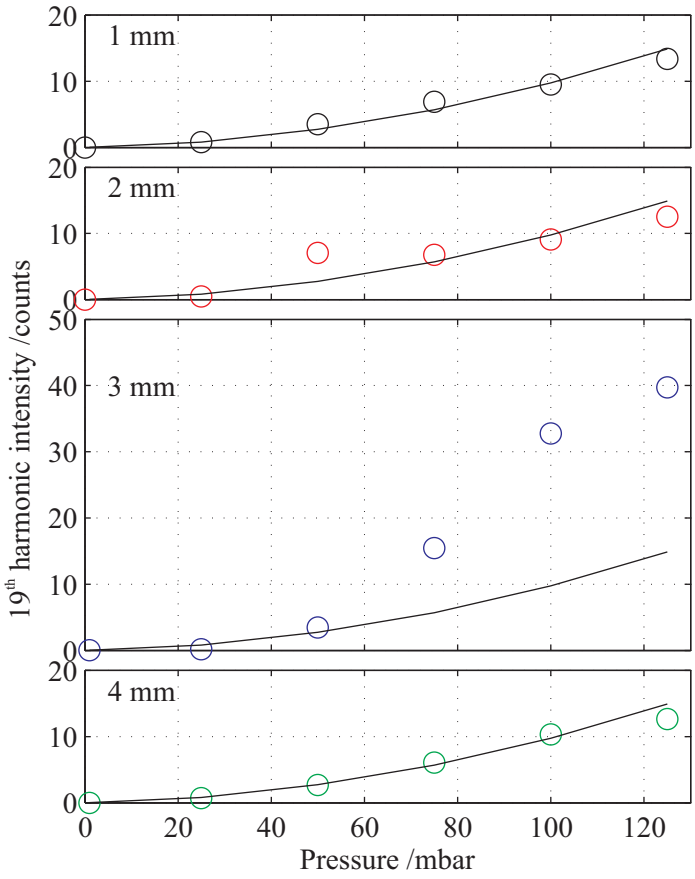

Figure 3.22: Peak intensity of the 19th harmonic as a function of pressure for different jet nozzle-laser separations, showing deviation from quadratic at 2 mm (at 50 mbar) and 3 mm (around 100 mbar).

The quadratic behaviour breaks down significantly when the Mach disc is at the laser focus (at 50 mbar for a height of 2 mm and at around 100 mbar for a height of 3 mm). This

is due to the formation of the high density Mach disc, which contributes further signal without being limited by phase matching. For reference, Figure 3.23 shows the predicted position of the Mach disc as a function of input pressure, using Equation 3.1. The background pressure used in the calculation is estimated from the fluorescence images to be ~ 1.5 mbar. Although there may be a contribution to the overall harmonic flux from the stagnant gas, its density is low and approximately the same for all jet nozzle-laser separations.

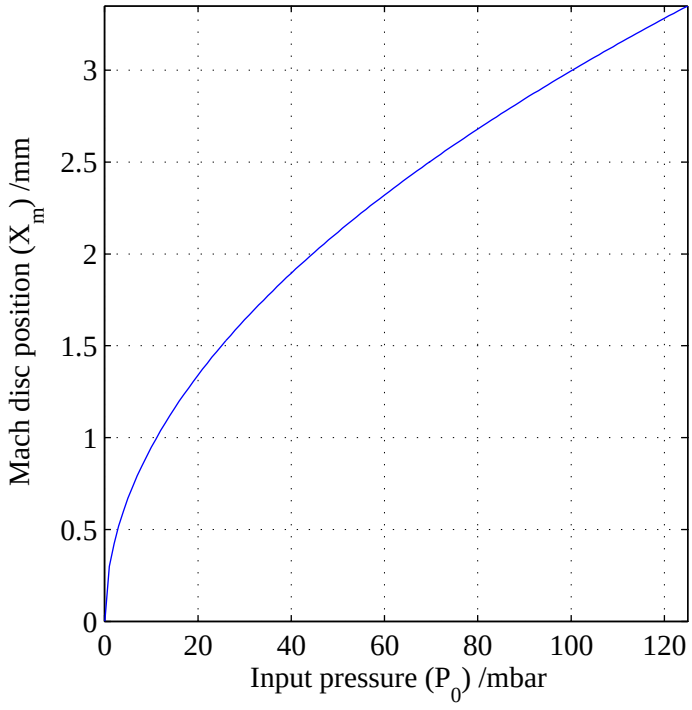

Figure 3.23: Estimated Mach disc position as a function of input pressure. The data are calculated using Equation 3.1 with a background pressure of 1.5 mbar.

The variation in XUV signal seen in the experiment is thus attributable to the density structure of the gas jet rather than phase matching. Since the coherence length is longer than the Mach disc, the limiting factor in harmonic flux is not the phase matching. The absorption length of argon at 25 mbar for the 19th harmonic of the laser is ~ 1 mm and so generation is not absorption-limited for a 500 μm Mach disc width at pressures used in this work. Note that for wavelengths close to 20 nm, the Cooper minimum present in the photoionization cross-section of argon [91] limits the output XUV flux [92,93].

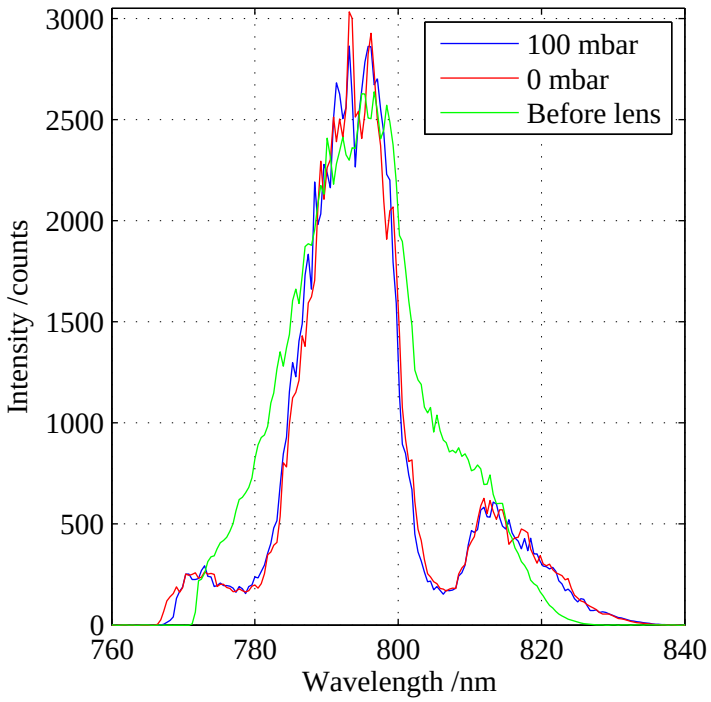

Figure 3.24: Fundamental spectrum taken at 100 mbar (blue), 0 mbar (red) and before the lens (green).

Since HHG is occurring from a relatively short, low pressure region, the nonlinear propagation effects are negligible. Indeed, Fig. 3.24 shows that there is negligible change in the fundamental spectrum from when the laser is focused into the Mach disc at an input pressure of 100 mbar to when there is no gas present. For reference, the spectrum before the focusing lens is also plotted. The spectra were recorded after the generation setup using an Ocean Optics HR2000CG spectrometer. The small difference in the spectrum in going through the lens is due to nonlinear propagation through the fused silica lens and windows of the vacuum chamber. The spatial intensity of the beam was also monitored after the generation setup and there were no visible signs of nonlinear propagation changing the spatial structure.

3.3.5 Discussion

Although the position for maximising harmonic signal from along the centreline of the argon gas jet has been determined, the flux needs to be increased further for HHG to be a source of XUV radiation suitable for nanoscale imaging. With integration times of 300 seconds required to obtain each spectrum, the recorded flux from HHG using an argon gas jet under

the experimental conditions described in this work is relatively low compared with generating using an argon-filled capillary under similar experimental conditions [32]. To further increase the XUV signal, the density and/or length of the generation region also needs to be increased. In the next chapter, the result of generating harmonics from a larger and denser volume of gas is documented. In addition, by scanning the laser focus through the gas, the position for maximising harmonic signal along the laser axis is established.

3.4 Summary

The determination of the structure of an argon gas jet using a loosely focused, highly intense femtosecond laser has been demonstrated. By using the observed fluorescence from the jet during HHG to position the jet with respect to the laser focus, the variation in harmonic output along the centreline axis of the jet has been established. At an input pressure of 100 mbar, an increase in XUV yield of ~ 350 % was achieved by focusing the laser into the Mach disc of the gas jet. As such, the position of the laser focus with respect to the centreline axis of the jet flow is an important parameter in the generation of harmonics.

4 Optimization of XUV Source

4.1 Introduction

In the previous chapter, high harmonic generation (HHG) from an argon gas jet was achieved. Variation in output extreme-ultraviolet (XUV) flux along the jet flow axis at the laser focus was demonstrated, with maximum output flux being obtained when focusing the laser into the Mach disc of the jet. However, the very centre of the laser focus is not necessarily the best location along the laser axis to position the gas in order to obtain maximum output flux. Depending on the gas density profile of the generation region and the phase matching, the optimum position of the gas region along the laser axis for maximising flux will vary for different harmonics. For regions of good phase matching (coherence length > length of generation region), a longer or denser region should allow a greater coherent buildup of harmonic flux. The absorption length, which is different for each harmonic, decreases with increasing pressure. At gas pressures when the absorption length becomes shorter than the coherence length, the absorption will limit the generation. This chapter discusses HHG from an argon-filled pipe at various positions along the laser axis. The region of gas within the pipe is longer and denser than the argon gas jet used in experiments in the previous chapter

4.1.1 Motivation

A high flux XUV source is desired for coherent diffractive imaging (CDI) of nanoscale objects. By using high flux radiation, a high signal-to-noise can be obtained and a high resolution of imaging can be achieved. The most intense harmonic observed using an argon gas jet was the 19^{th} harmonic. Since imaging resolution is limited by the wavelength of light used, it is necessary to develop a source with a peak harmonic wavelength much shorter for higher resolution imaging. Another goal is to generate monochromatic radiation. Such radiation will also increase the imaging resolution (see Chapter 5 for further discussion). The minimum number of harmonics observed via generation in an argon gas jet in the previous chapter was six. The number of harmonics therefore needs to be reduced. Although apparatus such as an XUV mirror can be used to single out harmonics for scattering, such

mirrors attenuate the radiation and are usually optimized to work for a specific wavelength only [94,95]. An alternative method of monochromating the spectrum is preferred. By translating the laser focus through the argon-filled pipe, an understanding of the generation region along the laser axis can be gained and the position to obtain maximum flux can be determined. The results will lead to methods using modulated gas regions for quasi-phase matching (QPM) (such as multiple gas pipes or jets) to generate high flux short wavelength monochromatic XUV light.

As discussed in the literature, the position of the generation medium along the laser axis for maximum output flux varies depending on the experimental conditions (due to the different scale of the contributions to phase matching). For example, Balcou *et al.* [96] discuss the generation of the 13^{th} harmonic from a 1 mm wide xenon gas jet at a pressure of 10 mbar, for peak laser focus intensities between 1.1×10^{13} W cm^{-2} and 6.4×10^{13} W cm^{-2}, and a confocal length of 3 mm. Highest harmonic yield is achieved when the laser is focused before the generating medium at low laser intensities but after the medium at high laser intensities[4]. Lindner *et al.* [39] discuss phase matching of the 25^{th} harmonic in argon at 10 mbar where both the generation region and confocal length are 100 μm long, and the peak intensity of the laser beam is 3×10^{14} W cm^{-2}. From both theory and experimental results, highest harmonic flux is obtained when the gas medium is positioned after the focus.

The conditions described in the literature for HHG using a gas pipe or jet are different compared to that used in this project – the confocal length and generation region is generally shorter, and the ionization fraction is usually lower. Furthermore, the absorption of the harmonics is usually neglected due to the low pressure and short length of generation region, and the complex density profile of jets has not been discussed. The density profile and absorption of the gas within and expanding from an argon-filled pipe at high pressures must be considered when the length of the generation medium is longer than the absorption lengths of the harmonics. This is the case at high pressures used in experiments discussed in this chapter. Since the conditions in this work are different from that documented in the literature, it is necessary to investigate the optimum position along the laser axis of the argon-filled pipe in order to develop a source suitable for nanoscale CDI.

4.2 XUV Generation using an Argon-Filled Pipe

It has been shown that when focusing an intense ultrashort pulsed laser into an argon gas jet, an increase in output harmonic flux is observed when focusing into a denser region of the jet (the Mach disc). Since the coherence length is longer than the Mach disc in the experimental

[4] Note that the fundamental laser wavelength was 1064 nm.

conditions used, using a longer or denser region of gas will increase the flux as long as the absorption length and coherence length do not decrease significantly. Limitations in the pumping system mean that a significantly larger jet nozzle cannot be used because the gas throughput would be too high at high input pressures. It is therefore necessary to use a gas geometry such as a gas-filled pipe that could accommodate a large volume of gas and restrict the gas flow.

By using an argon-filled pipe as the generation medium instead of an argon gas jet, gas flow can be restricted by having relatively small entrance and exit holes for the laser to pass through, and a longer generation region can be obtained. A longer region of gas will enable a longer cumulative buildup of high harmonic flux. In addition, by increasing the pressure within the region, a greater number of atoms will undergo HHG and the output flux should therefore increase. However, due to the variation in the phase matching throughout the focus, the generation will vary along the laser axis. In this section, the laser focus is translated through the argon-filled pipe to understand HHG along the laser axis and determine the position to obtain maximum flux. Although the high levels of ionization at the centre of the focus limit the output harmonic flux, the focusing conditions remain the same so that a comparison of HHG using an argon-filled pipe and an argon gas jet can be made.

4.2.1 Experimental Setup

The experimental setup is similar to that described in the previous chapter. A 790 nm, 1.1 mJ, 1 kHz, 40 fs pulsed laser from a Ti:sapphire system is focused using a 50 cm lens to give a confocal length of 1.3 cm inside a cross-piece vacuum chamber. On this occasion however, the chamber houses an argon-filled pipe with 500 μm holes drilled through it. Figure 4.1 displays a photograph of the of the vacuum chamber and gas pipe used in the generation setup, while Fig. 4.2 shows the corresponding schematic.

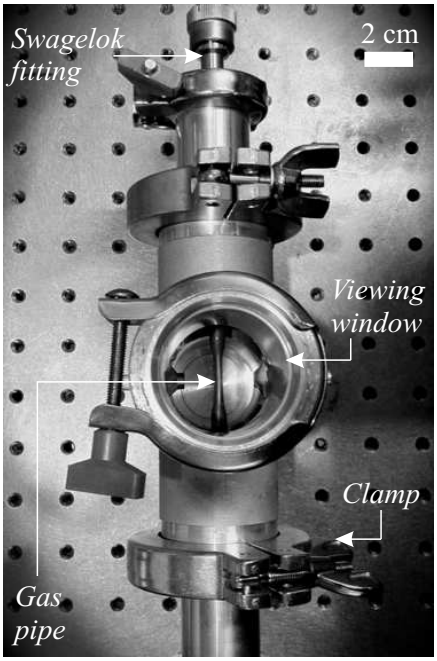

Figure 4.1: Photograph of generation setup consisting of a vacuum chamber containing a gas pipe.

The chamber is attached between adjustable bellows to allow alignment of the laser through the argon-filled pipe. The pipes at the side of the chamber have been replaced with pipes with a larger inner diameter to allow higher pumping throughput and enable a lower background pressure within the chamber. The width of the argon-filled pipe at the laser focus is 3 mm. Argon gas is passed through the pipe and out through 500 μm diameter holes that allow the laser to pass through, so that HHG can occur from the argon gas. The gas is then passed out the base of the chamber through a 16 mm pipe to a backing line.

Although the input pressure used in the experiment is less than that in the previous chapter, the actual pressure of the gas in the generation region is higher. The pressure in the pipe is estimated to be approximately the same as the input. In this work, the input pressure is 40 mbar.

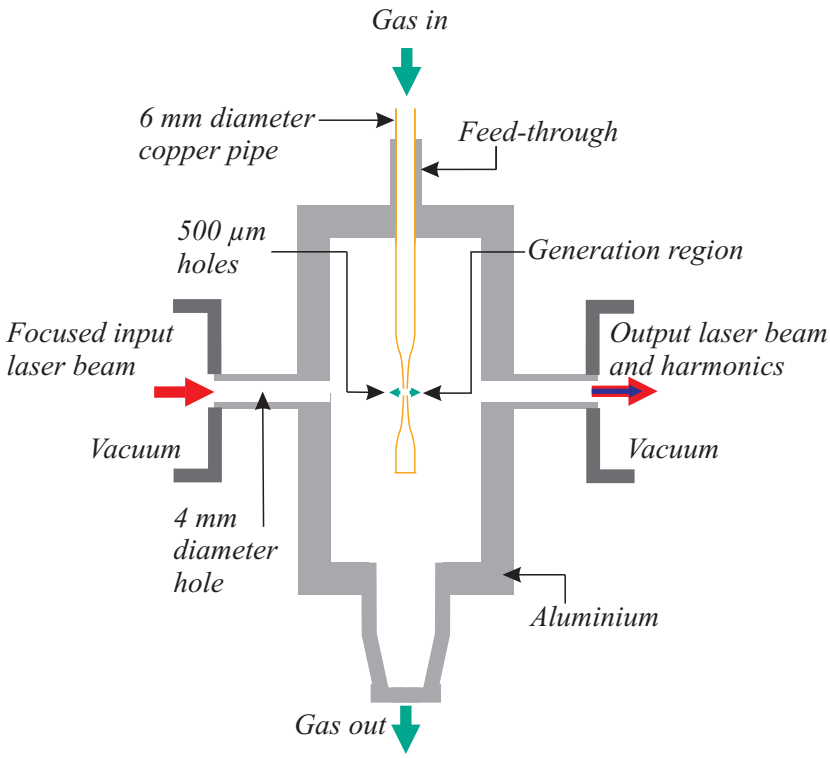

Figure 4.2: Side cross-section schematic of the configuration of the generation setup. Laser is focused using a 50 cm focal length lens through an argon-filled pipe.

The position of the laser focus with respect to the argon-filled pipe is varied by translating the lens. A 1.5 mm silica window at the side of the chamber (perpendicular to the laser axis and jet flow axis) allows observation of the geometry. The spatial distribution of the fluorescence and the output harmonic spectra from the argon gas were recorded every 1 mm translation of the laser focus through the pipe for a total of 38 mm (20 mm before and 18 mm after the argon-filled pipe). The fluorescence images are recorded to allow accurate determination of the laser focus with respect to the argon-filled pipe.

4.2.2 Spatial Distribution of Fluorescence

As observed in the previous chapter, fluorescence emission occurs from highly excited argon atoms and ions created when a very intense laser is focused into argon gas. The observed spatial distribution of the intensity of fluorescence inside the chamber (viewed perpendicular to the laser and pipe axes) when the argon-filled pipe is positioned at the laser focus is shown in Fig. 4.3. The input pressure in the pipe is 40 mbar. The observed fluorescence is recorded using a 1024 x 1024 pixel charged coupled device (CCD) camera. A 420 nm band pass filter is used in front of the CCD camera to allow imaging of fluorescence from long-lived (~ 1 µs) excited argon atoms. Again, a false colourmap is used in all the fluorescence

images presented in this work. The laser is focused from left to right in the image at a height of 0 mm and is centred at a distance of 0 mm. The pipe is vertical in the image and is also centred at a distance of 0 mm.

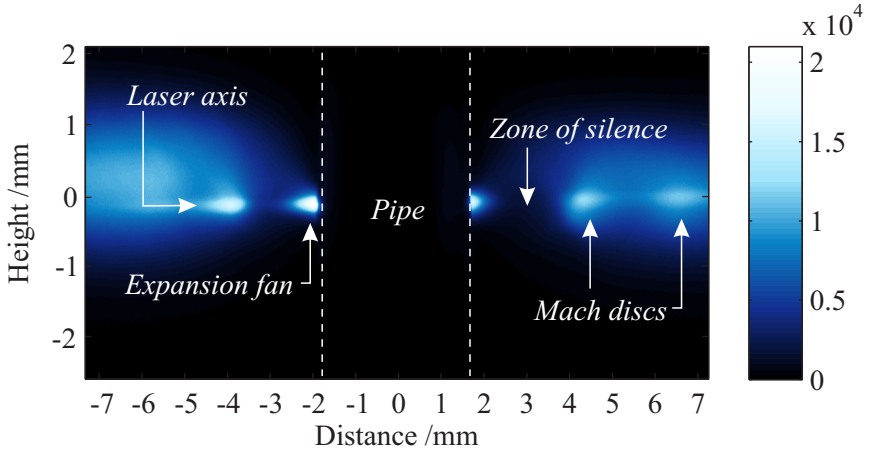

Figure 4.3: Spatial intensity of the fluorescence inside the chamber viewed perpendicular to the laser and pipe axes for an input pressure of 40 mbar, when the argon-filled pipe is at the laser focus. The image is recorded using a 420 nm band-pass filter.

The dip in fluorescence intensity at the centre of the image is because the walls of the pipe block any fluorescence emitted from argon gas inside the pipe from view. Although the largest high pressure region is in the pipe, from the fluorescence it is evident that significant gas is present either side of the pipe along the laser axis. Even though a gas pipe is used, the entrance and exit holes where the laser passes through act like nozzles and so gas jets are produced when gas is passed through the pipe. In this instance, the gas jets are parallel to the laser axis. Evident from the images on both sides of the pipe are zones of silence and Mach discs.

The fluorescence intensity profile from the jet expansion is made clearer by taking single pixel slices of the intensity of fluorescence along the laser axis, as displayed in Fig. 4.4. The peak in the fluorescence intensity at 1.5 mm either side of the pipe is emission from excited atoms and ions in the initial expansion fan. The zones of silence and Mach discs can be seen at 3 mm and 4 mm respectively either side of the pipe. Also, a secondary zone of silence is formed further along the laser axis on both sides of the pipe. This can be seen at -6 mm and 6 mm with respect to the centre of the pipe. However, the second zone of silence is much denser than the first and is shorter in length. A second Mach disc follows the second zone of silence. Due to the limitations of the data and setup, it is not possible to observe the rest of the fluorescence from the jet expansion either side of the pipe.

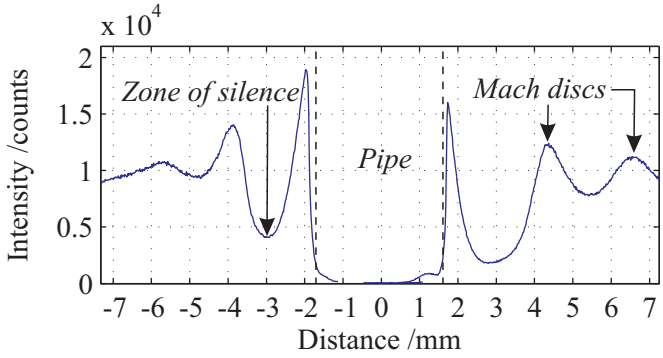

Figure 4.4: Single pixel slice of intensity of fluorescence along the laser axis at the laser focus using a 420 nm band-pass filter for an input pressure of 40 mbar, when the argon-filled pipe is at the laser focus.

Estimates of the pressure in the Mach discs and the background are important in understanding the generation and absorption in the experiment. Although the jet structure is visible when observing the fluorescence of the 420 nm emission, estimates of the gas pressure in the generation region are made from the spatial intensity of fluorescence of the 488 nm emission. This is due to short decay (~ 10 ns) of the dominant 488 nm Ar^{+}* (4s-4p) emission allowing observation of a more instantaneous density profile of the generation region. For reference, Fig 4.5 displays spatial intensity of fluorescence from the initial expansion, zone of silence and the Mach disc after the argon-filled pipe when using a 420 nm band-pass filter (top half) and a 488 nm band-pass filter (bottom half). The 420 nm fluorescence is much broader spatially than the 488 nm fluorescence due to the atoms and ions having diffused further by the time they have fluoresced.

Comparing the intensity of fluorescence of the 488 nm emission at 40 mbar with that at known pressure, the peak pressure in the Mach disc is estimated to be ~ 10 mbar, while the pressure in the zone of silence is estimated to be ~ 2 mbar. Using the equation to calculate the position of the Mach disc [80],

$$X_M = 0.67 d (P_0/P_b)^{1/2} \tag{4.1}$$

where d is the diameter of the jet nozzle and P_0 is the input pressure in the nozzle, the ambient background pressure P_b in the chamber can be calculated. At an input pressure of 40 mbar, the background pressure in the chamber is estimated to be 0.5 mbar.

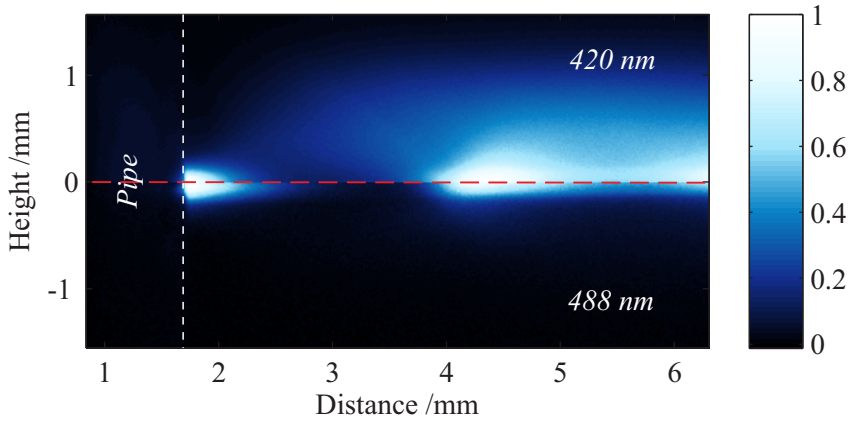

Figure 4.5: Section of the spatial intensity of the fluorescence after the pipe for an input pressure of 40 mbar, when the argon-filled pipe is at the laser focus. The top half of the image is recorded using a 420 nm band-pass filter, while the bottom half is recorded using a 488 nm band-pass filter. The data have been normalized to 1 count.

For reference, Fig. 4.6 displays a simple plot of the relative position of the pipe with respect to the laser propagation axis. The position of the pipe 5 mm after the focus is represented in purple, whereas the position of the pipe 5 mm before the focus is represented in green. A contour representing the spatial cut-off of the 25th harmonic for experimental conditions used in this work is also plotted to aid in understanding.

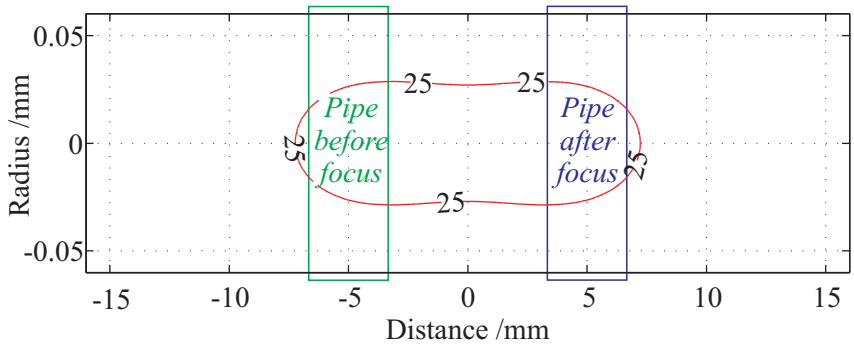

Figure 4.6: Plot of the relative position of the pipe with respect to the laser propagation axis. A contour plot of the spatial cut-off of the 25th harmonic is also plotted. The data are calculated using Equation 2.4.

4.2.3 XUV Spectrum

As demonstrated in the previous chapter, when a highly intense ultrashort pulsed laser is focused into argon gas, high harmonic XUV radiation will be generated. For generation from an argon-filled pipe, the output high harmonic spectrum for an input pressure of 40 mbar was obtained every 1 mm position that laser focus was translated. The high harmonic spectra were recorded using an XUV spectrometer. Each spectrum was integrated for 30 seconds (though the data in the plots have been normalised to 1 second for ease of quantifying). The radially summed intensity of the XUV harmonic spectra for pipe positions -10, 0 and 10 mm with respect to the laser focus is shown in Fig. 4.7. It is clear that at the three positions displayed, there is a difference between the spectra. More harmonics are observed at 10 mm and at 0 mm than at -10 mm. In addition, the intensity of the harmonics is greater at -10 mm than at 0 and 10 mm. There is also little spectral broadening and spectral splitting in the harmonics.

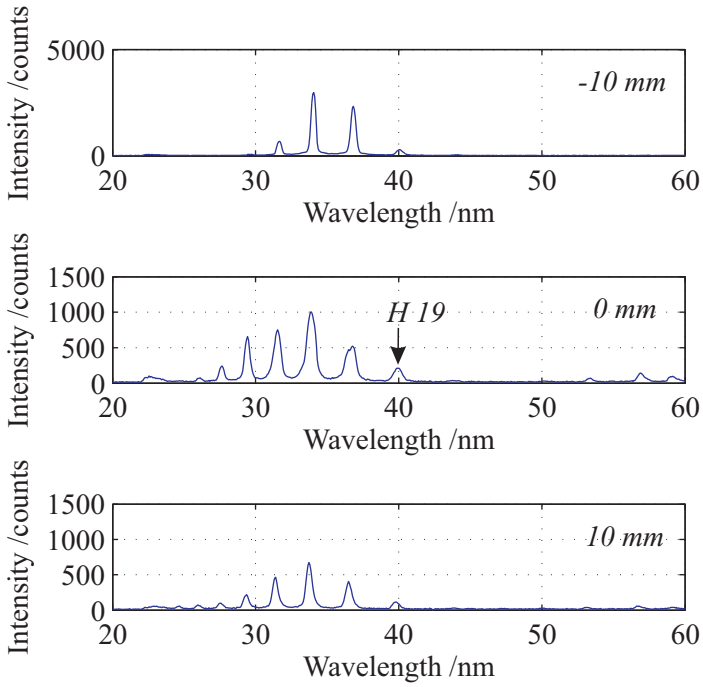

Figure 4.7: Intensity of harmonic spectrum between 20 and 60 nm at an input pressure of 40 mbar for pipe positions -10, 0 and 10 mm with respect to the laser focus. The data have been normalised to 1 second.

The spectra displayed in Fig. 4.7 have been summed spatially along the radius of the XUV beam. However, the spatial intensity profile of the XUV beam is important in CDI and so it is necessary to examine the spatial profile of the harmonics. Figure 4.8 shows the far-

field spatial intensity of the harmonic spectrum at an input pressure of 40 mbar for pipe positions -10, 0 and 10 mm. As discussed in the background chapter, harmonics generated from long trajectories electrons will be more divergent than short trajectories electrons. Therefore when viewing the output spectrum as a function of radius, it is possible to see the contributions from the two paths. Although there is no clear boundary between contributions from long and short trajectories, generally, the signal at the spatial centre of the XUV beam and harmonics will be mainly from short trajectories and the outer regions will be mainly from long trajectories [97,98].

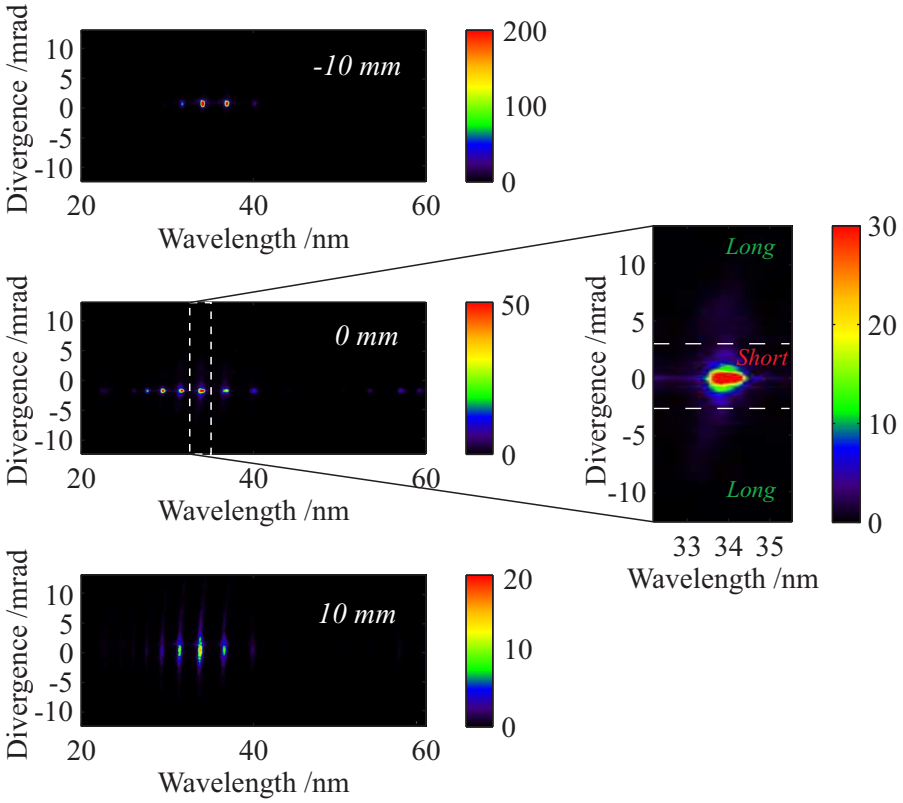

Figure 4.8: Far-field spatial intensity of the harmonic spectrum between 20 and 60 nm at an input pressure of 40 mbar for pipe positions -10, 0 and 10 mm with respect to the focus. Inset: spatial intensity of the 25th harmonic for an input pressure of 40 mbar and pipe position of 0 mm. The data have been normalised to 1 second.

From examination of the spectra displayed in Fig. 4.8, the harmonics can be separated into three approximate sections: the top and lower correspond to generation mainly from long trajectories and the middle corresponds to generation mainly from short trajectories. This is shown in the inset of Fig. 4.8, which displays the spatial intensity of the 25th harmonic at a pipe position of 0 mm. In this inset, the short trajectories contribute most to the output harmonic intensity. It is evident from Fig. 4.8 that the spectra throughout the

focus are dominated by short trajectories. However, the contribution from long trajectories is greater when the pipe is positioned after the focus. As the lens focus is translated through the pipe, the contribution from short trajectories increases significantly more than the contribution from long trajectories.

The result of the increase in contribution from short trajectories causes a decrease in the spatial FWHM of the harmonics. This narrowing of the beam can be seen in Fig. 4.9, which displays the summed spatial intensity of the 25th harmonic as a function of radius for pipe positions -10, 0 and 10 mm. It is also evident that the spatial intensity of the harmonic fluctuates significantly less when the pipe is positioned 10 mm before the laser focus due to the greater contribution from short trajectories and a higher signal-to-noise. Such behaviour is also observed for other harmonics. Note that minimal fluctuation in harmonic spatial intensity and thus spatial beam profile is desired for nanoscale imaging.

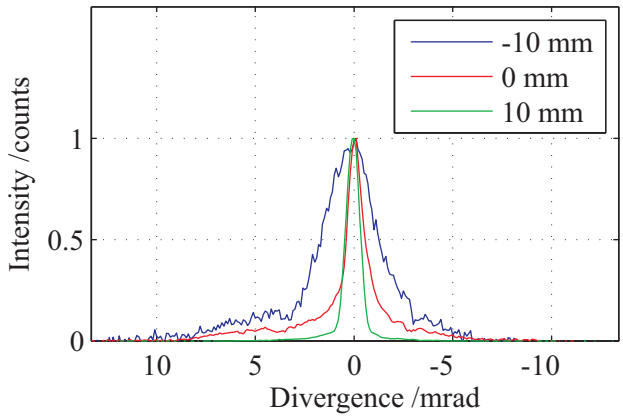

Figure 4.9: Intensity of the 25th harmonic as a function of radius for an input pressure of 40 mbar for pipe positions -10, 0 and 10 mm along the laser focus. The data have been normalised to 1.

To get a clear understanding of the generated XUV harmonics through the whole focus, the peak intensity of harmonics 15 to 27 as a function of distance through the laser focus is plotted in Fig. 4.10. Although the gas density profile in the setup is symmetric about the pipe, the XUV output is not symmetric about the focus. Indeed, the harmonic intensity of most harmonics is much higher when the pipe is positioned before the laser focus. For most positions throughout the focus (-10 mm to 10 mm), the three harmonics, H 23, H 25 and H 27 are the most intense. The maximum harmonic intensity at an input pressure of 40 mbar is nearly five times that when the pipe is positioned 7 mm before the laser focus than 7 mm after. This is the case for the 25th harmonic when the pipe is -7 mm. Much less intensity and variation in intensity is observed for the lower harmonics in the XUV spectra.

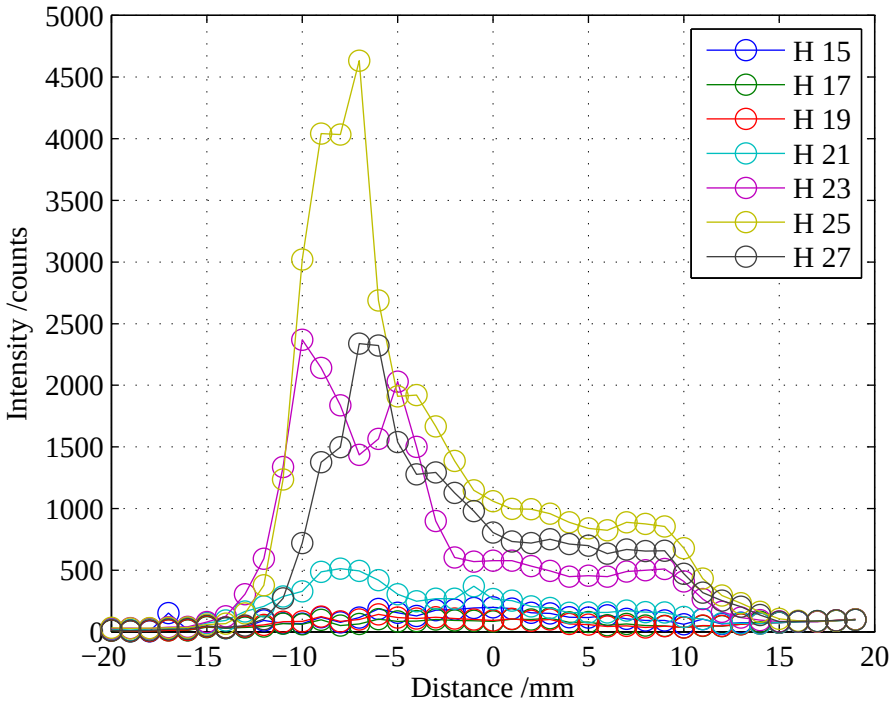

Figure 4.10: Peak intensity of harmonics as a function of pipe position with respect to the laser focus at an input pressure of 40 mbar. The data have been normalised to 1 second.

4.2.4 Phase Matching Considerations and Analysis

The coherence length (the length over which coherent buildup of high harmonic signal will occur), $L_{coh} = \pi/|\Delta \boldsymbol{k}|$, of the 25th harmonic at the laser as a function of radius and distance for long and short trajectory phase components at 40 mbar is displayed in Fig. 4.11. The coherence length is calculated from the wavevector mismatch, $\Delta \boldsymbol{k}$, between the fundamental and the harmonics resulting from the Gouy phase, atomic phase, neutral gas dispersion and the plasma dispersion.

Upon looking at the plots, it is clear that the phase matching is slightly asymmetric about the laser focus for both long and short trajectories. For both long and short trajectories, due to the high level of ionization, the coherence length is shortest at the focus. From the coherence lengths plot, it is evident that for the 25th harmonic, the contribution from long trajectories will be greater when the pipe is placed after the focus than before. Contributions from long trajectories have coherence lengths that are shorter than those of short trajectories, especially before the focus. With coherence lengths of < 0.5 mm throughout most of the generation region, significant coherent buildup is not achieved, even with the long generation region. This is observed experimentally (see Fig. 4.8). For short trajectories,

regions with coherence length over 1 mm exist both before and after the focus. The longer region of generation of the argon-filled pipe means that short trajectories which have coherence lengths ≥ 0.5 mm can achieve greater coherent buildup than with the argon gas jet. Indeed, the harmonic signal is significantly greater than generating using the 500 μm wide argon gas jet. Note that generally, the coherence lengths of both long and short trajectory phase components are longer for lower harmonics. This can be seen in Fig. 4.12, which shows that the coherence length for short trajectories of the 17th harmonic at 40 mbar is as long as 8 mm.

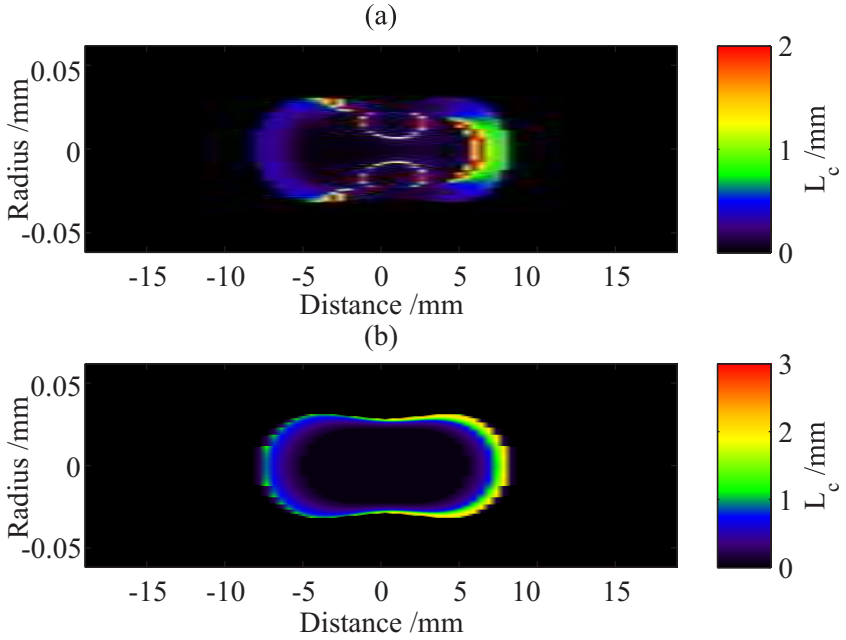

Figure 4.11: Coherence length of the 25th harmonic as a function of radius and distance along the laser propagation axis for (a) long trajectories and (b) short trajectories at a pressure of 40 mbar. The data are calculated using Equation 2.21.

The difference in the XUV spectra before and after the focus is due to absorption. A plot of the absorption length in argon for the 15th to 35th harmonic is displayed in Fig. 4.13 as a function of pressure. As seen from the plot, absorption is greater at higher pressures and lower harmonics. At a pressure of 2 mbar (the estimated pressure in the zone of silence), most of the harmonics have an absorption length > 2 mm. However, at a pressure of 10 mbar (the estimated pressure in the Mach disc), the absorption length of harmonics 15 to 23 has decreased to < 4 mm. For the 25th harmonic and above, the absorption length is > 5 mm at 10 mbar, which is greater than the maximum coherence length and so is not a limiting factor in the cumulative buildup for such a harmonic. The absorption is even greater at 40 mbar (the pressure of the gas inside the pipe). At such pressure, the absorption length has decreased to < 0.5 mm for the 19th to 23rd harmonic, thus limiting the buildup of harmonic signal.

Although the absorption length has decreased for the higher harmonics (H 25 and above), the length is still longer than the coherence length and region of gas, meaning that maximum cumulative buildup can be achieved for such harmonics.

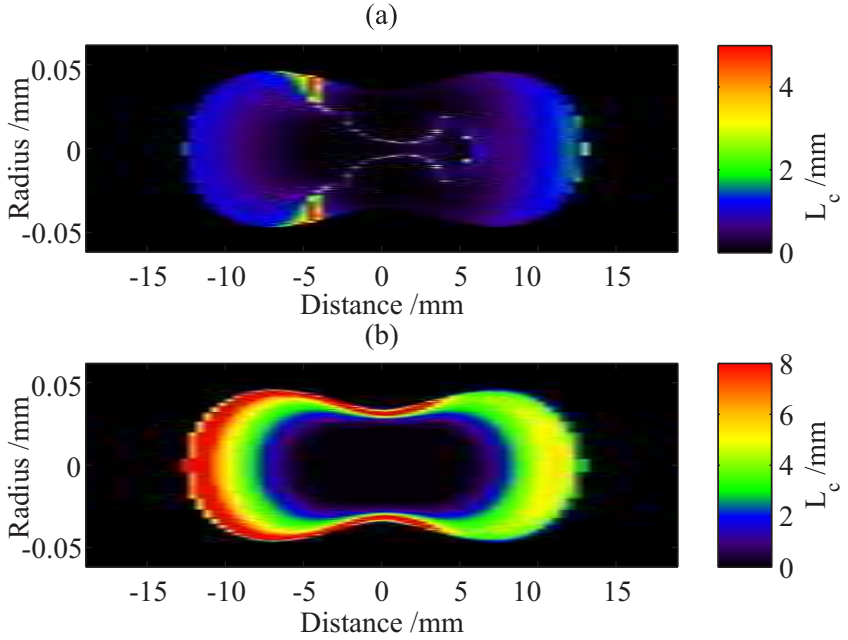

Figure 4.12: Coherence length of the 17th harmonic as a function of radius and distance along the laser propagation axis for (a) long trajectories and (b) short trajectories at a pressure of 40 mbar. The data are calculated using Equation 2.21.

However, as seen from the fluorescence image in Fig. 4.3, a significant amount of gas is present either side of the pipe where the gas jets are formed. Although signal will be generated from the Mach discs before the pipe when the pipe is after the focus, the gas after the pipe (further along the laser propagation axis) is outside the spatial cut-off where the laser intensity is high enough to generate XUV radiation and so does not contribute to the output signal. Any harmonics generated when the gas pipe is after the focus will therefore be strongly absorbed by the gas jet formed along the laser propagation axis which does not generate high harmonics. The absorption length in the each of the Mach discs is ~ 5 mm for the 25th harmonic, which is approximately the combined length of the Mach discs and the expansion region. As such, approximately 63 % of the harmonic's signal generated within the pipe will be absorbed by the time it has propagated through the non-generating gas. The harmonic intensity is therefore significantly reduced when the pipe is positioned after the laser focus (see Fig. 4.14 for a simple plot of the gas density profile from the argon-filled pipe positioned after the laser focus).

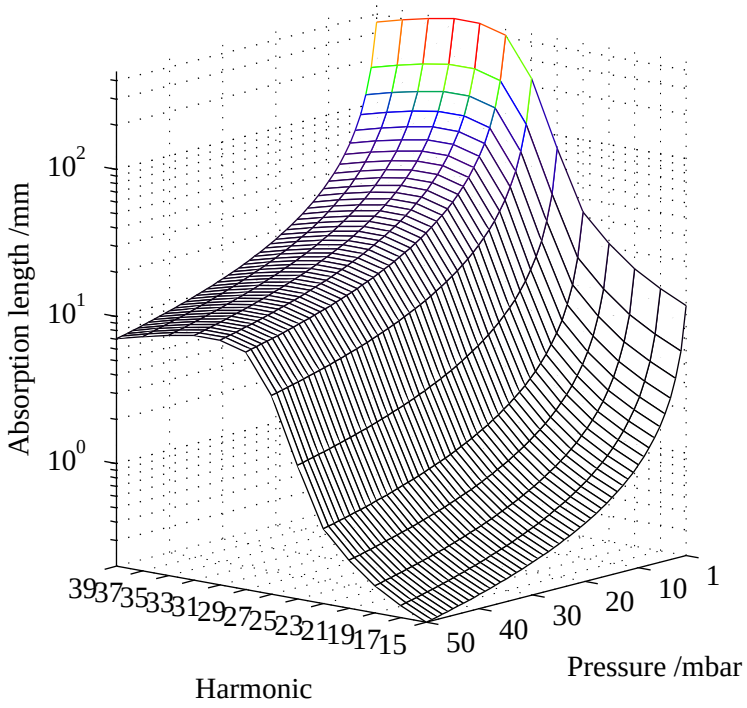

Figure 4.13: Absorption length in argon as a function of harmonic and pressure. The data are taken from reference [17].

It is only when the pipe is located before the laser focus that gas from both the pipe and the Mach discs further along the laser propagation axis will contribute to the generation. The harmonic intensity is greater when the pipe is before the focus since the amount of absorbing gas outside the generation region further along the laser propagation axis is significantly less. Although there is still gas further along the laser propagation axis which is outside the cut-off region, the density of the jet at this point is negligible. The absorption length of the background gas in the chamber is > 10 mm for XUV harmonics.

It is evident that from the spectra in Fig. 4.7, harmonics 29 to 35 are weaker than the other harmonics for all positions along the laser axis. Even though it is possible to generate harmonics with wavelengths as short as 20 nm (H 39), because of the Cooper minimum present in the photoionization cross-section of argon [91], harmonics close to 20 nm will be less intense than harmonics of much shorter or longer wavelengths [92,93]. In addition, due to a short coherence length and small region in which the intensity is high enough to generate harmonics 29 and above, the length over which significant coherent buildup can occur is therefore small for harmonics 29 and above. The output harmonic intensity is therefore less than for the lower harmonics. These high harmonics are more intense when the pipe is located after the focus due to better phase matching. The long absorption length (~ 10

mm) means that harmonics generated when the pipe is placed after the focus will still be transmitted through the non-generating gas further along the laser propagation axis.

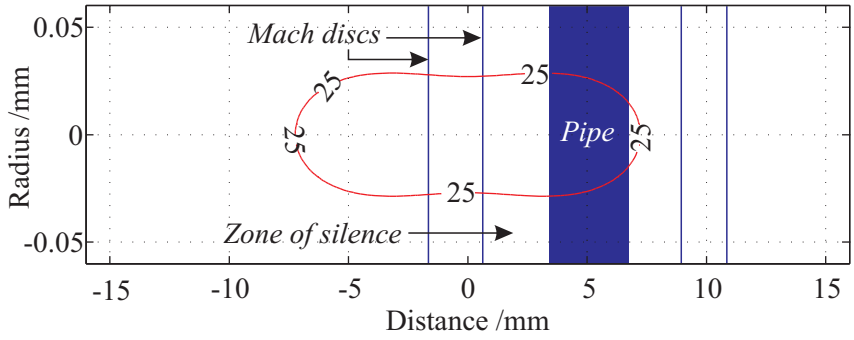

Figure 4.14: Plot displaying a simplified density profile of the gas from the argon-filled pipe positioned after the laser focus. A contour plot of the spatial cut-off of the 25th harmonic is also plotted. The data are calculated using Equation 2.4.

Although at both 10 mm and -10 mm the pipe is placed outside the spatial cut-off of many harmonics (see Fig. 4.15), such harmonics are still observed due to the width of the gas region extending into the cut-off regions. Eventually however, when the pipe position is far enough from the centre, the majority of gas from the pipe and jet expansions will be outside the cut-off for all harmonics between 20-60 nm, and so the XUV flux will drop to zero.

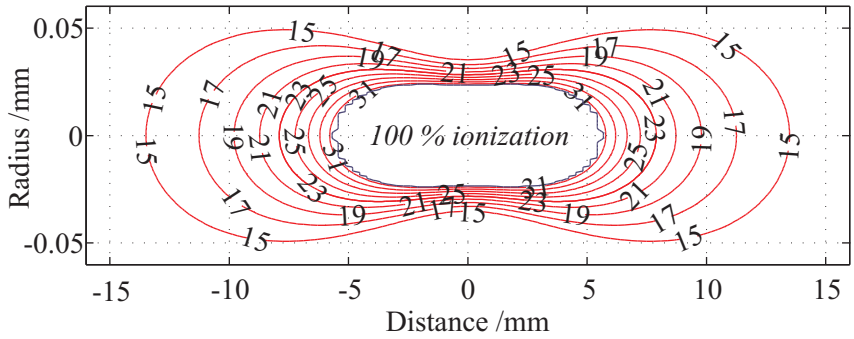

Figure 4.15: Contour plot of the spatial cut-off at the laser focus for various harmonics. Labelled on the plot is the region of 100 % ionization. The data are calculated using Equation 2.4.

Note that the slight modulation in the intensity of the harmonics through the focus seen in Fig. 4.10 is perhaps due to the profile of the gas region. The density of the gas along the laser axis is itself modulated due to the jet expansion either side of the pipe along. The

difference in these modulations between harmonics is due to the difference in the phase matching and spatial cut-off of the harmonics.

High peak laser intensities and high ionization fractions mean that nonlinear propagation may potentially occur [99]. However, there is no visible wavelength-shifting of harmonics and the nonlinear refractive index is small at the pressures used here. As such, nonlinear propagation effects are negligible in this work.

4.2.5 XUV Generation as a Function of Pressure

Due to the desire for a high flux monochromatic source, further investigation of the reduced spectral range and flux increase seen at -7 mm was undertaken. The spatial intensity of the fluorescence as well as the output XUV spectra were recorded at input pressures 1-50 mbar, in steps of 5 mbar. For reference, the spatial intensity of fluorescence from the argon gas inside the chamber (viewed perpendicular to the laser axis and jet flow axis) at various pipe input pressures is displayed in Fig. 4.16.

The laser is focused from left to right in the image and is centred at a distance of 7 mm. Since the pipe is located before the focus, the fluorescence intensity is greater after the pipe. At 50 mbar (Fig. 4.16 (e)), the peak in the fluorescence intensity at a distance ~ 4 mm either side of the pipe is due to the laser exciting and ionizing argon gas in the Mach discs. The subsequent dip in intensity at ~ 6 mm either side of the pipe is a secondary zone of silence that comes before a second Mach disc, which is visible at the edge of the image. It is evident from the image that the first zone of silence is much less dense than the second and is also longer.

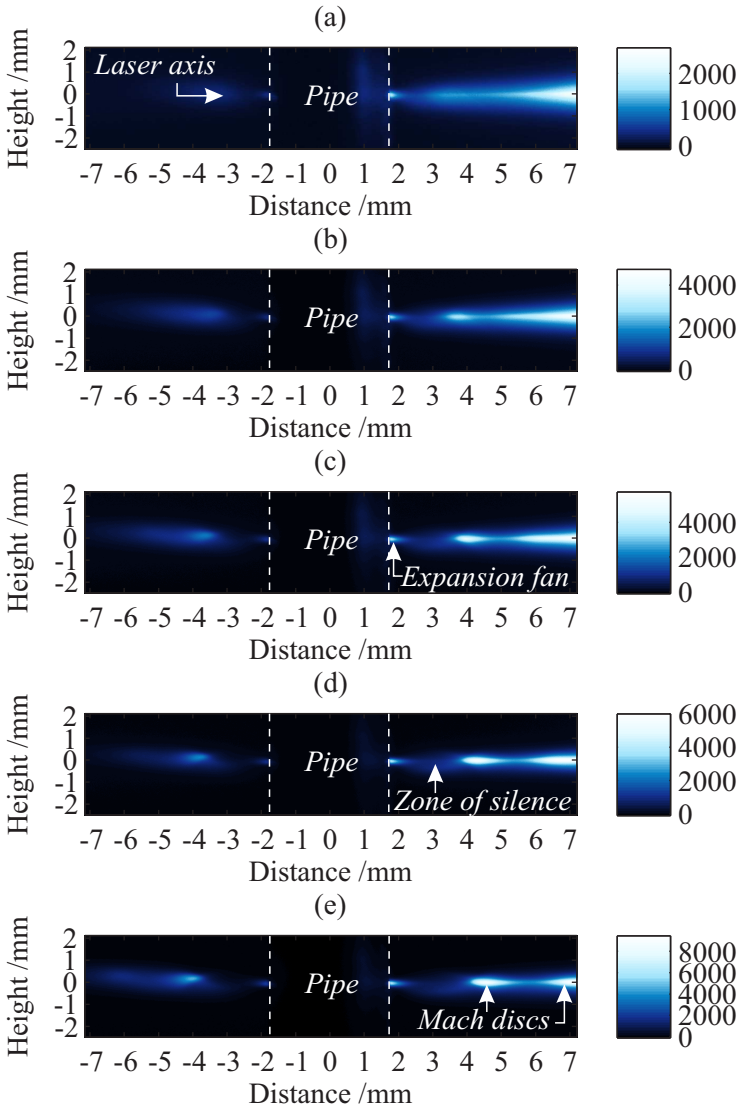

Figure 4.16: Spatial intensity of the fluorescence inside the chamber viewed perpendicular to the laser and pipe axes for an input pressure of (a) 10 mbar, (b) 20 mbar, (c) 30 mbar, (d) 40 mbar and (e) 50 mbar, when the pipe is at a distance of -7 mm with respect to the laser focus. The image is recorded using a 420 nm band-pass filter.

The intensity of the XUV spectra at various input pressures when the pipe is -7 mm from the laser focus is displayed in Fig. 4.17. Again, the spectra are summed along the radius of the beam. As the pressure increases, the peak harmonic flux increases and the number of observed harmonics decreases. At an input pressure of 10 mbar, six harmonics are clearly visible in the spectrum, but at 50 mbar, only three harmonics are visible.

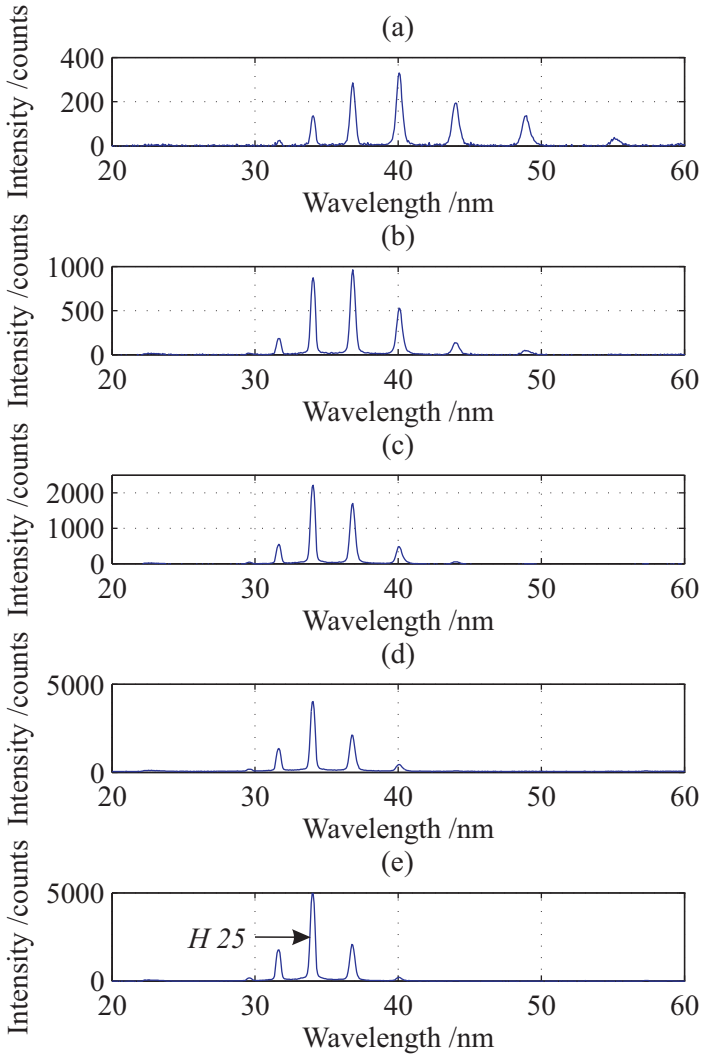

Figure 4.17: Intensity of the harmonic spectrum between 20 and 60 nm for an input pressure of (a) 10 mbar, (b) 20 mbar, (c) 30 mbar, (d) 40 mbar and (e) 50 mbar. The data have been normalised to 1 second.

For input pressures above 30 mbar, the 23rd, 25th and 27th harmonics become significantly more intense than the other harmonics. At 50 mbar, the 25th harmonic is at least twice as intense as the other harmonics. The peak intensity of the harmonics as a function of input pressure is displayed in Fig. 4.18. It is evident from the figure that most harmonics have peaked in intensity before 50 mbar. Only the 25th and 27th harmonics continually increase in intensity as the pressure is increased to 50 mbar.

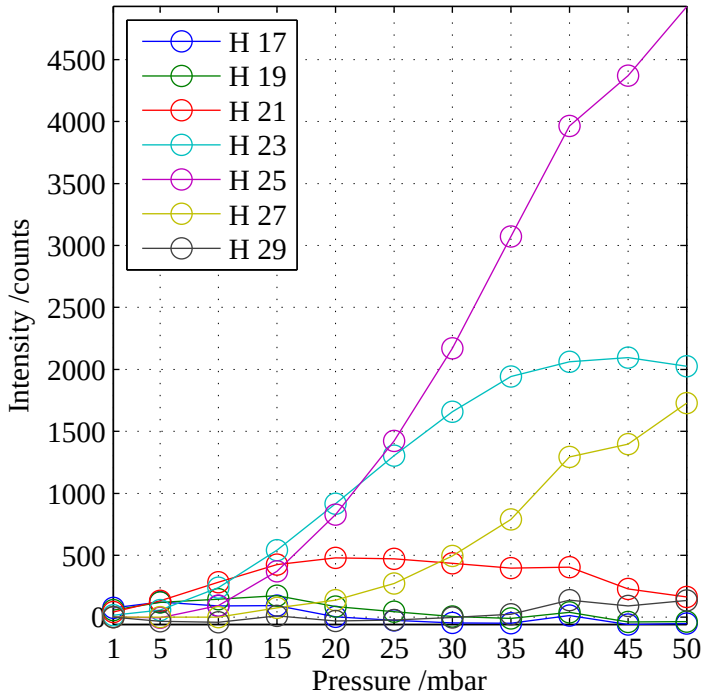

Figure 4.18: Peak intensity of harmonics as a function of pressure when the pipe is at a distance of -7 mm with respect to the focus. The data have been normalised to 1 second.

4.2.5.1 Analysis

As stated in Chapter 2, the output intensity of the q^{th} harmonic can be written as [60],

$$\left|E_q\right|^2 \approx N^2 \left|\chi_{eff}^{(q)} E_0^s\right|^2 \left(\frac{1 + e^{-2\alpha L} - 2e^{-\alpha L} cos\Delta \boldsymbol{k} L}{\alpha^2 + \Delta \boldsymbol{k}^2}\right) \tag{4.2}$$

where N is the number density of atoms, $\chi^{(q)}_{eff}$ is the effective nonlinear susceptibility of the q^{th} harmonic, E_0 is the input electric field, s is the effective order of the nonlinearity (~ 5), α is the absorption coefficient and $\Delta \boldsymbol{k}$ is the total wavevector mismatch. The terms in the round brackets describes the contribution of phase matching to the output intensity of the q^{th} harmonic in the presence of absorption. It is evident from Equation 4.2 that the intensity of the harmonic signal increases quadratically with the number density of the atoms, as long as there is no change in the coherence length or absorption.

Figure 4.19 shows the intensity of the 23rd, 25th and 27th harmonic as a function of pressure with a quadratic plot fitted to each graph. Upon looking at the figure, it is clear that as the pressure is increased to 25 mbar, the intensity of all three harmonics increases

quadratically. This is because the buildup of harmonic signal at such pressures is not limited by the absorption (the absorption length is longer than the coherence length) and the coherence length does not change significantly with pressure. As seen in Fig. 4.14, absorption is greater for longer wavelength XUV radiation than shorter wavelength XUV radiation and the absorption length decreases with increasing pressure. Indeed, the intensity of the 23rd harmonic deviates below the quadratic after 25 mbar since the pressure has increased to a magnitude that the absorption limits the buildup of signal. The absorption length at 25 mbar is ~ 1 mm, while the maximum coherence length is ~ 3 mm. As the pressure is increased further, the absorption length of the 25th harmonic decreases to a point that it significantly limits the buildup of output signal. The intensity of the 25th harmonic deviates below the quadratic at 45 mbar. At such high pressure, the absorption length is ~ 1 mm, which is shorter than the longest coherence length for the harmonic (~ 3 mm). For the 27th harmonic, the absorption is not limiting the output XUV signal for pressures used in the experiment and so the intensity continues to increase quadratically with increasing pressure.

Since the absorption is greater for longer wavelengths than shorter wavelengths, the intensity of the lower harmonics is significantly less at high input pressures. The Cooper minimum and the short generation and coherence lengths of very high harmonics (H 29 and above) limit the intensity for such harmonics. The combination of these effects means that the envelope of the harmonic spectrum narrows with increasing pressure. Hence, the intensity of the 25th harmonic is much greater than the neighbouring harmonics.

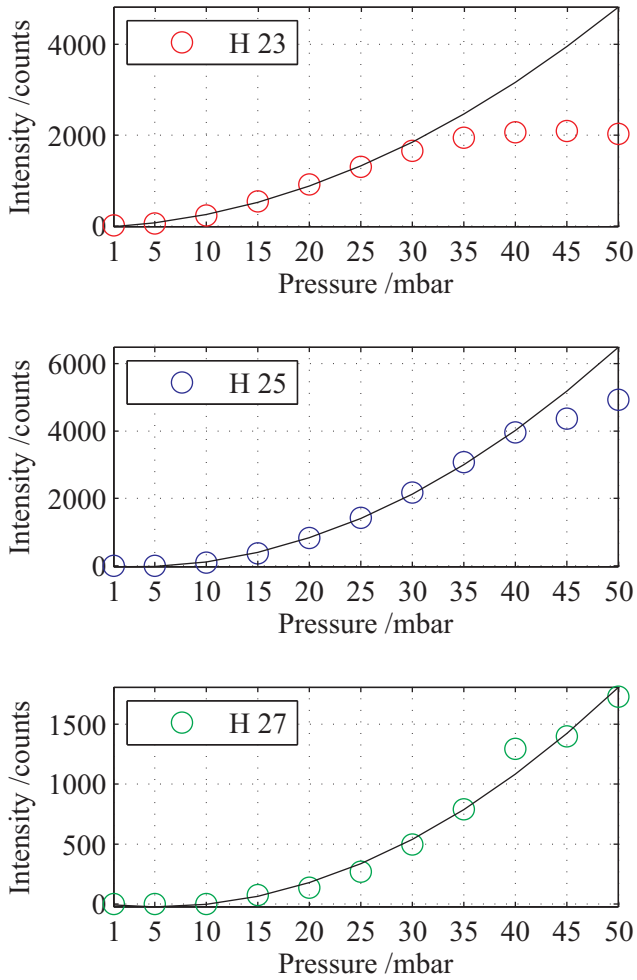

Figure 4.19: Peak intensity of 23rd, 25th and 27th harmonic as a function of pressure when the pipe is at a distance of -7 mm with respect to the focus. A quadratic plot is fitted to each graph. The data have been normalised to 1 second.

4.2.6 Discussion

Although an increase in XUV flux has been achieved by generating from an argon-filled pipe compared with an argon gas jet, the limiting factors on the overall yield are absorption and ionization. Due to the high levels of ionization creating a large phase mismatch, a significant amount of generation has negligible contribution to the output harmonic flux. To avoid this, a much longer focal length lens should be used so that the beam spot is larger and the beams energy is spread over a larger area. In addition, a shorter duration pulse or a pulse with a steeper front should also be used so that a significant amount of generation can occur before high levels of ionization are present.

The limitations of the vacuum setup meant it was not possible to increase the input pressure further to obtain higher flux at shorter wavelengths. The introduction of differential

pumping should enable higher input pressures and therefore allow potentially higher flux to be achieved.

Although absorption limited the overall XUV yield at high pressures, absorption aided in the reduction in the number of harmonics generated, which is desired for CDI. The presence of the Cooper minimum in the spectrum also aided in the reduction of the number of harmonics. However, such effects limited the output of shorter wavelength XUV radiation, which is desired for high resolution imaging. An alternative inert gas, such as neon or helium, should be used as the generation medium and an alternative method should be developed to produce high flux short wavelength monochromatic radiation. As detailed in the background chapter, neon and helium are also more transmissive than argon for XUV radiation.

4.3 Work in Progress

One way to improve the flux of short wavelength radiation beyond intensities already obtained is to use QPM. Such a method enables a cumulative buildup of output signal by using a periodic structure to suppress the intensity of the signal when the fundamental and harmonics are out of phase, and not when they are in phase. As discussed in Chapter 2, QPM can be achieved by using a generation region that has a modulated density [67,68]. Techniques to obtain a modulated density include using a single gas pipe or multiple gas pipes, multiple gas jets, as well as acoustic waves within a gas cell. Note that to significantly improve flux of radiation at wavelengths near 20 nm, it is advisable to use an alternative gas to argon, such as neon or helium as the generation medium so that the Cooper minimum is avoided and shorter cut-off wavelengths can be generated. Using such gases will also reduce the absorption of generated XUV radiation. For initial experiments however, argon is chosen due to strong emission lines which allow viewing of the gas geometry during HHG.

4.3.1 Multiple Gas Regions

It is evident that from the fluorescence images of excited argon atoms and ions from a single argon-filled pipe in Section 4.2, a modulated density region along the laser axis can be created by a sequence of Mach discs. Depending on the desired period of modulation for QPM, the separation and density of the Mach discs can be varied by changing the input and background pressure. Alternatively, multiple gas jets can be used to create a generation region of modulated density. Figure 4.20 shows a diagram of free jet expansion from two gas jets that are moved close together. At a distance when the barrel shocks touch, they merge. When the jets are even closer together, they merge and a larger jet is formed with an

ineraction disc that is larger and further away than that for a single jet [100]. By altering the distance between the jets, the density modulation through the jets will vary at different distances along the jet flow.

In a similar setup demonstrated in reference [68], a jet cell has been developed with the aim of creating a modulated region of pressure along the confocal length of the focused laser beam by using a sequence of jets.

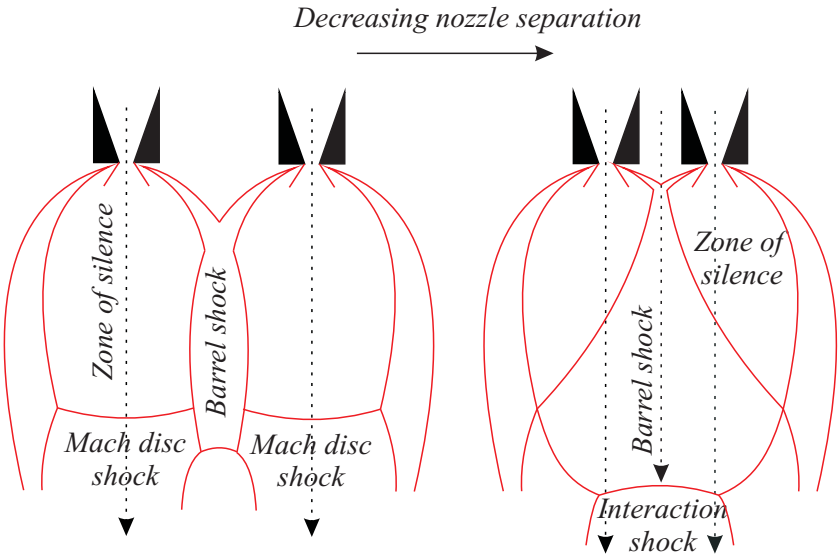

Figure 4.20: Shock interaction between two adjacent jets. Adapted from reference [101].

The same gas cell design as described in Section 3.2 is used. On this occasion however, argon gas is supplied into the top of the cell and passed through a 1.5 cm square, 2 mm thick, interchangeable aluminium plate with holes with a diameter and half pitch of 0.5 mm. The plate is placed just above the laser entrance and exit holes so that when jets of gas are formed, a region of modulated pressure is created along the laser axis. Figure 4.21 shows the spatial intensity of fluorescence from a multiple jet configuration when the laser is focused into the cell. This image was taken using a 1024 x 1024 pixel CCD camera with a 488 nm band-pass filter to select out 488 nm Ar^{+}* (4s-4p) emission. The input pressure behind the plate was 30 mbar and the integration time for the image is 30 seconds. The colour scale is saturated to aid in viewing of the jets.

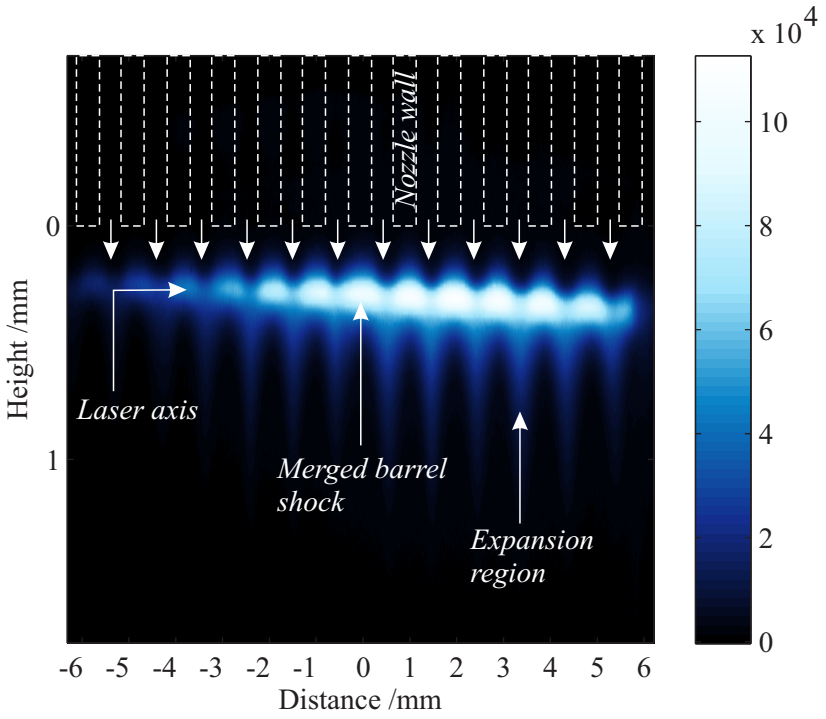

Figure 4.21: Spatial intensity of the fluorescence inside the jet cell with an input pressure of 30 mbar, laser power of 1 W and laser pulse length of 40 fs. The plate contained 500 μm diameter holes on a 1 mm pitch. The image is recorded using a 488 nm band-pass filter. The integration time of the image is 30 seconds. The colour scale is saturated to aid in viewing of the jets.

In the image, the laser is focused from left to right at a height 250 μm below the plate and is centred at distance of 0 mm. The peaks in the intensity of fluorescence along the laser axis are where the barrel shocks have merged. The fluorescence that extends down the image is from atoms and ions in long-lived states moving in the expansion region. Since the dominant emission has a lifetime of ~ 10 ns and the maximum velocity is ~ 500 m s^{-1}, such particles do not travel far during fluorescence. Therefore the observed fluorescence along the laser axis is essentially an indication of the instantaneous density. The slight curvature and slope of the fluorescence along the laser axis is due a lens defect and the laser beam being focused at a slight angle with respect to the base of the plate. Plotted in Fig. 4.22 is a single pixel slice taken along the laser axis showing the modulation in the intensity of fluorescence and therefore density that can be achieved using multiple jets.

Using various jet nozzle sizes and separation, different modulations can be created along the laser axis at different distances along the jet flow axis, thus potentially allowing QPM for different harmonics (since different harmonics will have different coherence

lengths). Such variability in an XUV source is desired for developing a nanoscope suitable for imaging a variety of objects.

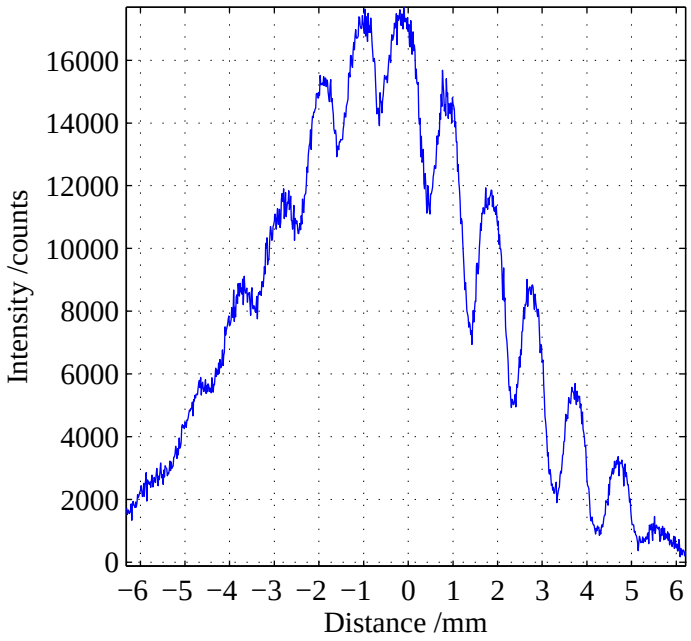

Figure 4.22: Single pixel slice taken along the laser axis of the intensity of fluorescence displayed in Fig. 4.21.

4.3.2 Acoustic Quasi-Phase Matching

If QPM can be demonstrated using multiple jets and high flux short wavelength radiation obtained, then the next step is to develop a more versatile setup so that the period of modulation of the gas density could be varied with ease. This could be achieved using acoustic waves. If a setup can be constructed so that an acoustic wave is coupled into a gas cell, then a region of modulated gas along the laser axis at the laser focus could be created within the cell. With the use of a signal generator, the period of modulation can be easily changed.

An acoustic cell that periodically modulates the gas density along the laser focus is proposed. A schematic of the proposed acoustic cell is shown in Fig. 4.23. The beam is focused into a transparent acrylic gas cell that is 1 cm long, 8 cm high and has walls 5 mm thick. Acrylic is chosen because it is easier to engineer than glass. The cell has 500 μm diameter holes drilled through its walls to allow the laser in one side of the cell and out the other. Argon gas is supplied into the cell through a 6 mm plastic hose. Attached to one wall of the cell is a piezoelectric ceramic (lead zirconate titanate) disc. This transducer is

connected to an amplifier and a signal generator so that its signal can be amplified and its operating frequency varied. The transducer is placed at an angle of 10 degrees to ensure the acoustic wave it generates travels across the beam. The two small chambers either side of the generating cell are there to enable differential pumping so that high pressure inside the cell can be achieved with as little gas as possible outside the generation region. This will therefore reduce absorption of XUV radiation and overloading of the turbomolecular pumps.

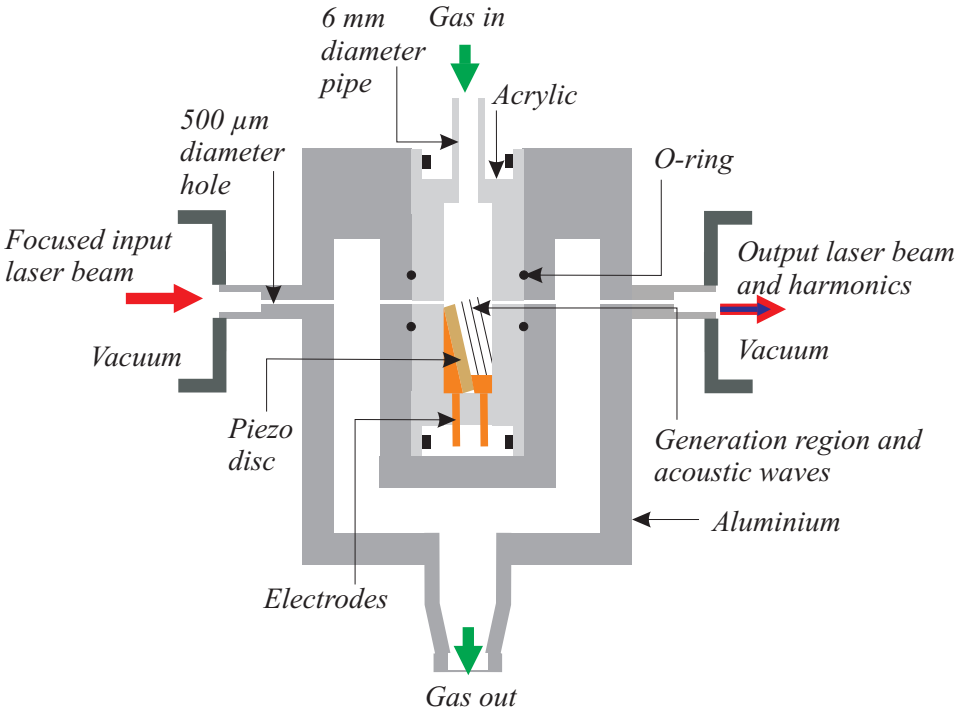

Figure 4.23: Acoustic gas cell setup used for acoustic QPM of high harmonics.

The desired period of modulation (Λ) for QPM is the coherence length, such that $\Lambda = \pi/|\Delta \boldsymbol{k}|$, where $\Delta \boldsymbol{k}$ is the total wavevector mismatch. However, since acoustic waves are to be generated at an angle inside the gas cell, this angle must be taken into account when determining the modulation period to be used. As a point of note, the transducer will still work at frequencies other than its resonance, but it will be less efficient. Due to the geometrical design of the cell, an appropriate standing wave will not be produced in the setup. The piezo should therefore be pulsed in synchronization with the laser so that the same modulation is present every time a laser pulse is present.

In order to successfully generate an acoustic wave across the length of the gas cell setup, the attenuation of sound must be considered. However, depending on the pressure, wavelength and gas used, the attenuation will vary. As displayed in Fig. 4.24, the shorter the wavelength of an acoustic wave and the lower the pressure of the gas, the greater the

attenuation of the acoustic wave by the gas (see [102]). In argon, the attenuation of an acoustic wave, α, can be calculated using the relationship [103],

$$\alpha = \frac{1.83 \times 10^{-11} \left(\frac{T}{T_0}\right)^{1/2} f^2}{\left(\frac{P}{P_0}\right)} \times \frac{8.686}{1000} \tag{4.3}$$

where T is the experimental temperature, T_0 is the reference temperature (293.15 K), P is the experimental pressure, P_0 is the reference pressure (1 bar) and f is the frequency of the acoustic wave. Here, α is in dB mm^{-1}.

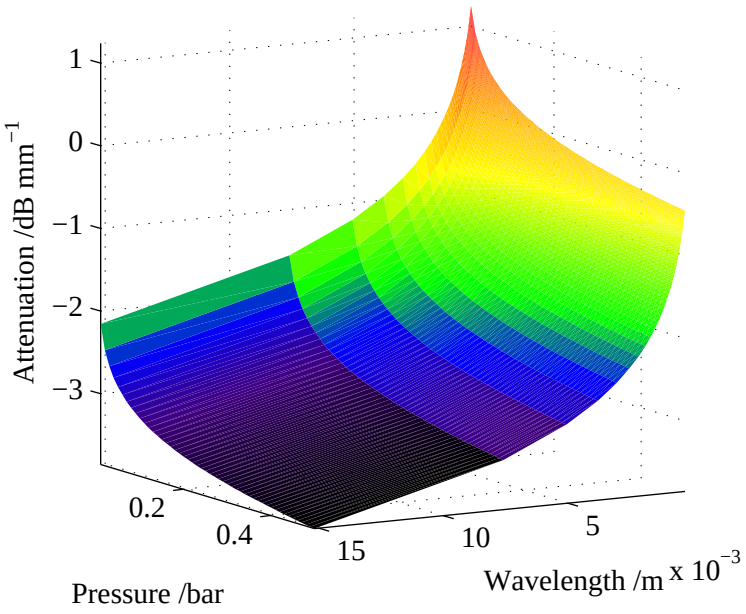

Figure 4.24: Attenuation of sound in argon at 20 °C as a function of gas pressure and acoustic wavelength. The data are calculated using Equation 4.3.

The range of wavelengths that can be used for successful acoustic QPM will be limited by the attenuation of an acoustic wave. As seen from Fig. 4.24, it is necessary to operate at as high pressure as possible to reduce attenuation of an acoustic wave. However, due to the short absorption lengths of XUV radiation in argon at high pressures, an alternative gas such as neon should be used. In addition, to verify the propagation of the acoustic wave, the beam focus should be made as large as possible for ease of observation of any modulation in the fluorescing gas. As long as a balance between acoustic wavelength, pressure and XUV radiation absorption can be found, acoustic QPM should be possible.

4.4 Summary

A nearly fiftyfold increase was achieved by using a 3 mm argon-filled pipe as the generation medium, instead of a 500 μm argon jet. The peak XUV flux was observed for the 25^{th} harmonic at an input pressure of 40 mbar when the pipe was placed -7 mm from the focus. This peak XUV flux is two orders of magnitude greater than that observed from HHG using an argon gas jet. In addition, a spectrum consisting of a smaller number of output harmonics was obtained by careful positioning of the pipe (again at -7 mm) and by using high input gas pressure. The spectrum consisted primarily of three harmonics, with the 25^{th} harmonic twice as intense as the other two most intense harmonics.

Although additional techniques to increase the XUV flux have been proposed, the results obtained so far indicate that an argon-filled pipe as an HHG source is potentially suitable for CDI of nanoscale structures. In the next chapter, XUV scattering using radiation generated from such a source is discussed and the development of a table-top XUV nanoscope is realised.

5 XUV Scattering

5.1 Introduction

Scattering of light occurs when a region of a wavefront's electric field is changed in phase or amplitude by a medium. Information about the medium is contained in the amplitude and phase of the electric field of scattered light. Hence, the scattering pattern from an object can potentially be used to determine its structure.

When light is scattered from an object and imaged using a lens, the phase information is retained in the refracted waves and the electric field distribution is an image of the object. For XUV wavelengths and shorter, it is not feasible to use lenses due to the weak refraction and strong absorption of such radiation in most materials. By using a technique called coherent diffractive imaging (CDI), the need for a lens is removed. The function of the lens is instead replaced by software.

An algorithm is used to reproduce the amplitude and phase of the electric field close to that directly after the object. The algorithm works by applying various constraints whilst iterating between real and Fourier space domains. Although the method was invented in the 1970s, it has only recently been employed due to the increase in speed of computer processing. The limitation on the resolution of the reconstructed object depends on the angular acceptance of the camera and the convergence of the algorithm.

While the work done in this thesis so far has been focused on the optimization of the generation of extreme-ultraviolet (XUV) radiation, the results presented in this chapter are obtained from the scattering of such light from micron-sized objects (though detail on the reconstructed objects can be discerned down to a dimension of ~ 300 nm).

5.1.1 Motivation

The ability to produce coherent high harmonic radiation using a laboratory based table-top source has allowed progress in CDI using XUV radiation. To date, CDI using a high harmonic source has been demonstrated using both single wavelength scattering and more recently, multiple wavelength scattering. In 2008, a resolution of 94 nm was achieved using narrow-bandwidth mirrors to single out a single wavelength from the source before

scattering [23], while in 2009, Chen *et al.* [104] obtained 165 nm resolution using the whole harmonic spectrum. In the foreseeable future, CDI using high harmonics generated at wavelengths in the water-window will allow imaging of a variety of nanostructures.

5.1.2 Coherence

High spatial coherence is needed for obtaining a well defined scattering pattern since high spatial coherence implies stationary interference between waves. The XUV radiation produced by HHG can possess high spatial coherence as demonstrated by Bartels *et al*. [105] who used a double slit to show well defined interference fringes. The degree of spatial coherence can be defined by how visible a set of interference fringes are. Strong modulation will only occur when the light incident on the two slits is spatially coherent.

Although the spatial coherence of the radiation is high, the temporal coherence is low because the pulse length is short. The beat frequency between harmonics is of the order of femtoseconds (a time much shorter than the readout time of the detector) and so no interference is observed between different harmonics. Every scattering pattern recorded in this work is therefore the incoherent sum of the scattering patterns from each harmonic.

5.1.3 Fresnel and Fraunhofer Diffraction

The spatial profile of light scattered from an object depends on the distance between the object and the camera. The type of diffraction observed is defined by the Fresnel number [106],

$$F = \frac{a^2}{L\lambda} \tag{5.1}$$

where a is the radius of the aperture (or object), L is the distance from the object to the camera and λ is the wavelength of the light. When the camera is placed close to the object ($F \geq 1$), Fresnel diffraction is observed. At large distances away from the object, when $F \ll 1$ (far-field), Fraunhofer diffraction is observed.

Computationally, it is faster to work in the Fraunhofer region since the electric field in the far-field is the Fourier transform of the electric immediately after the object. As such, the scattering patterns discussed in this work are obtained in the Fraunhofer region of diffraction.

5.2 Experimental Setup

5.2.1 XUV Source

The XUV source used in the setup is the same as that described in the previous chapter. A 50 cm lens is used to focus a 1.1 W, 1 kHz, 43 fs laser beam into a 3 mm wide argon-filled copper pipe. 500 µm diameter holes drilled through the walls allow the focused laser to pass through the pipe and generate high harmonics from argon gas in the process. The aluminium chamber that contains the pipe is 4 cm in diameter and 15 cm high. As indicated in the diagram in Fig. 5.1, the exit holes of the aluminium chamber are 1 mm in diameter and gas is passed out through the base so as not to overload the turbomolecular pumps at high backing pressures. This setup has already been characterised in the previous chapter, and in this work, the focus is placed in a region of gas 7 mm after the pipe to produce spectra with high flux and reduced harmonic range. This is to increase the chance of successful CDI.

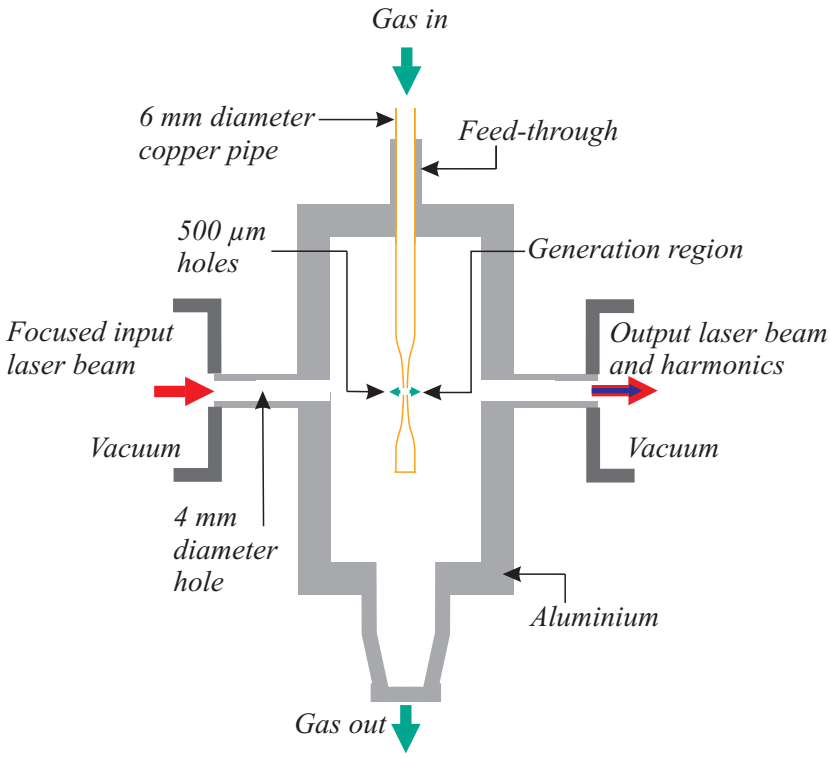

Figure 5.1: Cross-section schematic of vacuum chamber containing an argon-filled copper pipe. The pipe's walls have 500 µm diameter holes so that the focused laser beam can pass through and generate high harmonics from the argon.

5.2.2 XUV Scattering Vacuum Chamber

The setup used takes advantage of the extension to the vacuum system already in place. In this way, the overall setup remains the same and the camera can be moved to allow the XUV beam to pass through to the spectrometer. A charged coupled device (CCD) camera is bolted to an aluminium bracket that is attached to a vacuum end plate. This plate is water cooled to 12.5 ºC to assist in the cooling of the CCD camera and thus reduce the noise on recorded images. A KF40 vacuum port is used to enable a sample holder (see next subsection) to be attached through a feed-through to a two-axis stage that allows alignment of a sample with respect to the XUV beam. On the front of the CCD camera is a black baffle that has a 5 mm diameter hole. This baffle is designed to block any laser scatter that may leak into the chamber. An additional aluminium filter was also added to the setup to reduce laser scatter.

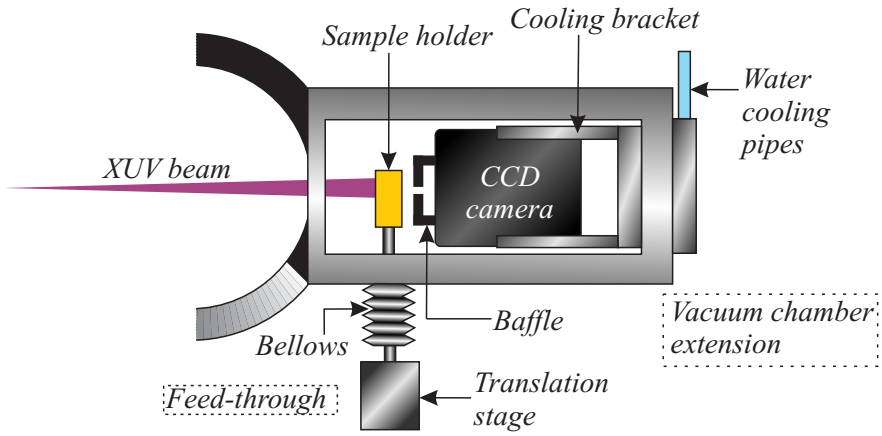

Figure 5.2: Schematic of the experimental setup used in CDI.

5.2.3 Sample Holder

A photograph of the sample holder manufactured by Aaron Parsons is displayed for reference in Fig. 5.3. The sample holder is 3 cm high, 7 cm long and 7 mm thick and made out of brass. It consists of four holes: one hole for alignment, one hole to allow the attachment of a feed-through and two holes for mounting samples.

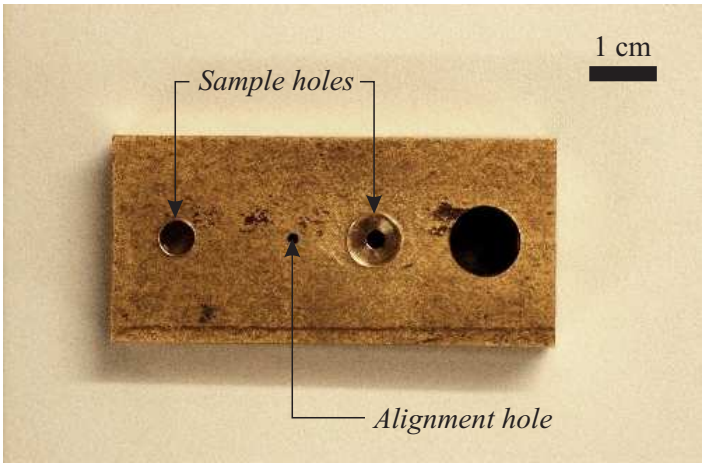

Figure 5.3: Photograph of sample holder.

5.2.4 XUV CCD Camera

The XUV detector used in this work is an Andor DX-434 CCD camera, which is suitable for use inside vacuum chambers. It has an active image sensor size of 13.3 mm with 13 μm pixel resolution in a 1024 x 1024 array. The pixels have a quantum efficiency of ~ 60 % for XUV wavelengths. These pixels are photodiodes that collect a charge that is proportional to the number of photons incident them. This charge will buildup until a specified integration time when the pixels pass the charge to the edge of the CCD camera where it is recorded. The minimum readout time for an image consisting of 1024 x 1024 pixels is 2 ms.

It is desirable to record scattering patterns using as short an integration time as possible to avoid saturation of the CCD camera which can lead to signal from saturated pixels leaking to unsaturated pixels. However, as the central region of a scattering pattern is usually considerably more intense than that at larger angles, it may not be possible to measure information at both small and large angles using a single CCD camera exposure. This is because high spatial frequency information may be below the CCD camera noise level. The scattering patterns are therefore recorded for different sets of integration times. By taking images at short exposures and splicing these to long exposure images, a scattering pattern that contains both high spatial frequencies and low spatial frequencies can be obtained. The splicing works by replacing the saturated pixels of the long exposure image with the unsaturated pixels from the short exposure image. Although shifts can occur in the scattering pattern and any random noise will not be the same for the two images, a similar method has proved successful in work carried out by Chen *et al.* [104].

5.2.4.1 Nonlinearity

Since a scattering pattern from an object will vary in intensity, the linearity of the CCD camera must be measured. The linear response corresponds to the range in which the CCD camera signal is proportional to photon flux. However, when a pixel exceeds its saturation level, electrons will overflow from the pixel's potential well to other pixels. This means that pixels around the region of saturation will have an incorrect intensity. A set of XUV images, taken for different exposure times, were used to determine the relationship between recorded flux and real flux. Figure 5.4 shows the recorded pixel count verses relative incident intensity. Data was taken for 10, 50, 100, 500, 750, 1000 and 1250 milliseconds, and a best fit was plotted. Plotted also on the image is the maximum possible CCD camera count. It is clear that as long as the incident intensity is below the maximum, then the relationship between pixel count and incident intensity is linear and so no adjustments to the intensity of a scattering pattern needs to be made.

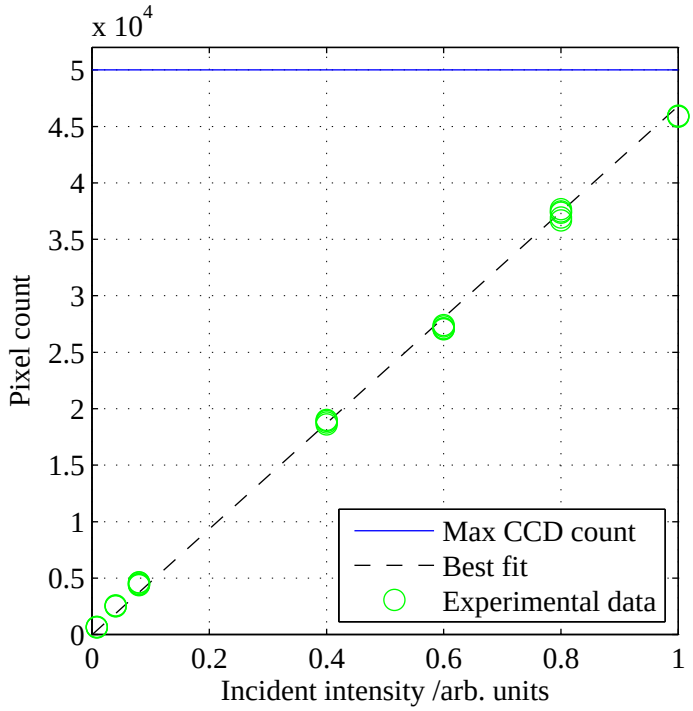

Figure 5.4: Pixel count vs. relative incident intensity.

5.2.4.2 Noise

Noise will degrade the quality of recorded images and therefore must be reduced. Even when there is no incident light on a CCD camera, there will still be signal from readout noise and thermal noise. The readout noise is the result of the imperfect operation of the

electronics converting an analogue signal into digital output. This noise is independent of the integration time and the temperature of the CCD camera. The thermal noise on the other hand is the result of thermally exciting electrons into the conduction band and thus producing signal. Since the thermal noise is dependent on temperature and integration time, it can be reduced by cooling the CCD camera.

It is therefore important to determine at what temperature the thermal noise is significantly small. Figure 5.5 shows the standard deviation of 1024 pixel counts when there is no incident light on the CCD camera for temperatures -30 ºC to 20 ºC in steps of 5 ºC. For each temperature, a signal was recorded for four different integration periods, 0.1, 1, 10 and 60 seconds. The plots show that thermal noise is dependent on integration time and is reduced at lower temperatures.

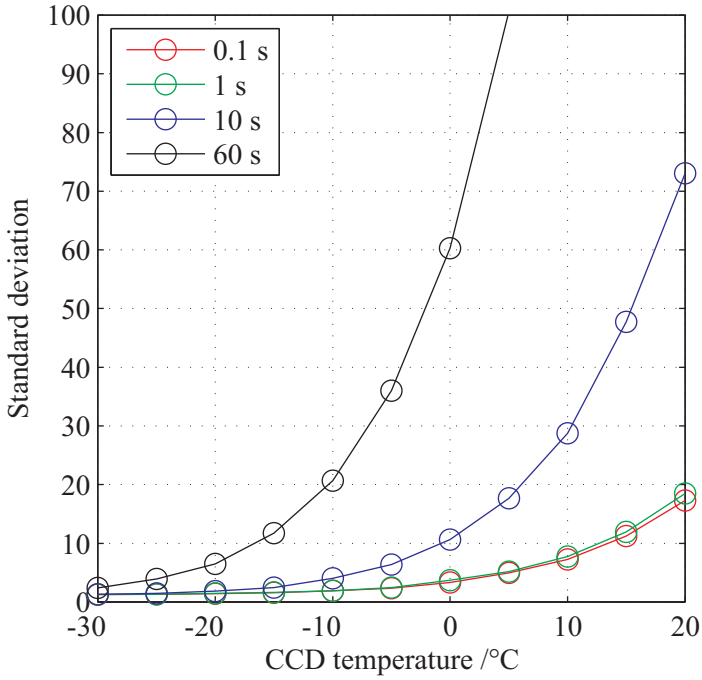

Figure 5.5: Standard deviation of background photon counts on the CCD camera for 0.1 (red), 1 (green), 10 (blue) and 60 (black) seconds.

For temperatures below -15 ºC, the standard deviation is less than 15 counts and reaches less than 5 counts by -30 ºC for all integration times plotted. By reducing this thermal noise, the scattering pattern will be more readable. Due to the limitation of the cooling mechanism, it is not possible to hold the CCD camera at -30 ºC for periods longer than an hour, as the efficiency will decrease significantly. Therefore, throughout this thesis the temperature is held at -25 ºC. The DC offset accumulated during integration is removed from all images.

5.3 XUV Beam

Using the CCD camera, the spatial intensity profile of the XUV beam was recorded five times at four different pressures. Each image was recorded for an exposure time of 25 milliseconds. From Fig. 5.6, it is clear that the beam is elliptical in shape. This is due to the focused laser beam having a smaller M^2 in x than y. This is not a concern since any CDI will be done using samples that are < 20 µm and are therefore much smaller than the beam. As expected from the results of the XUV spectra discussed in the previous chapter, as the input pressure increases, so does the intensity of the beam. The round dark patches on the images are the result of oil deposited on the camera (see Fig. 5.6 (d)).

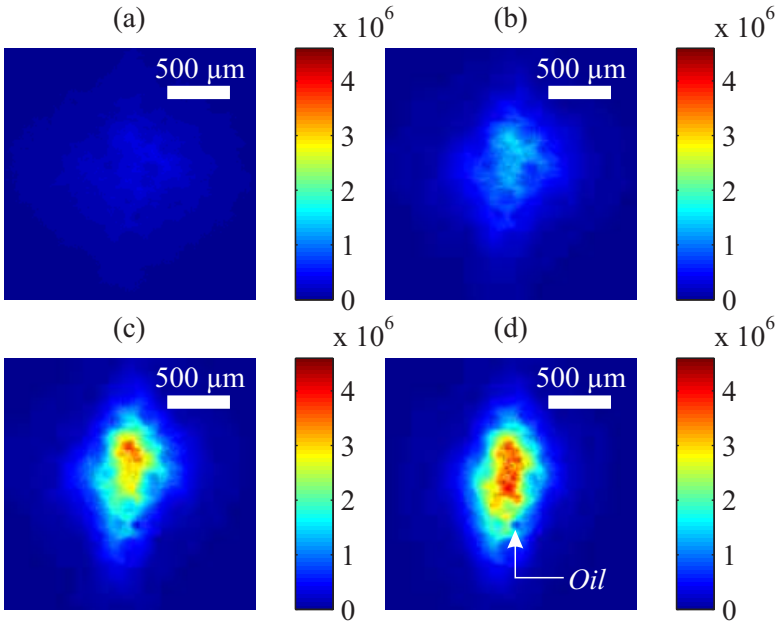

Figure 5.6: Spatial intensity profile of the XUV beam at four different pressures (a) 10 mbar (b) 20 mbar, (c) 30 mbar and (d) 40 mbar. Labelled on the figure is an oil deposit.

5.3.1 Flux Though an Aperture

In order to minimise the time taken to record a scattering pattern, it is necessary to understand how much flux is going through a sample. By using the estimated value of the beam waist from previous work [107] and flux values at 40 mbar input pressure from Section 5.3, the propagation of a Gaussian XUV beam from the cell was calculated to estimate the number of photons passing through different diameter pinholes, for different XUV source to sample distances. Upon looking at Fig. 5.7, there is potentially a factor of sixteen less flux when using a 5 µm diameter sample compared to a 20 µm diameter sample

at a distance of 60 cm. Since it is desirable to obtain a scattering pattern in the Fraunhofer region of diffraction, samples greater than 50 μm cannot be used at the current sample to camera distance of 46 mm. The Fresnel number for a 50 μm diameter pinhole at 46 mm is ~ 0.5.

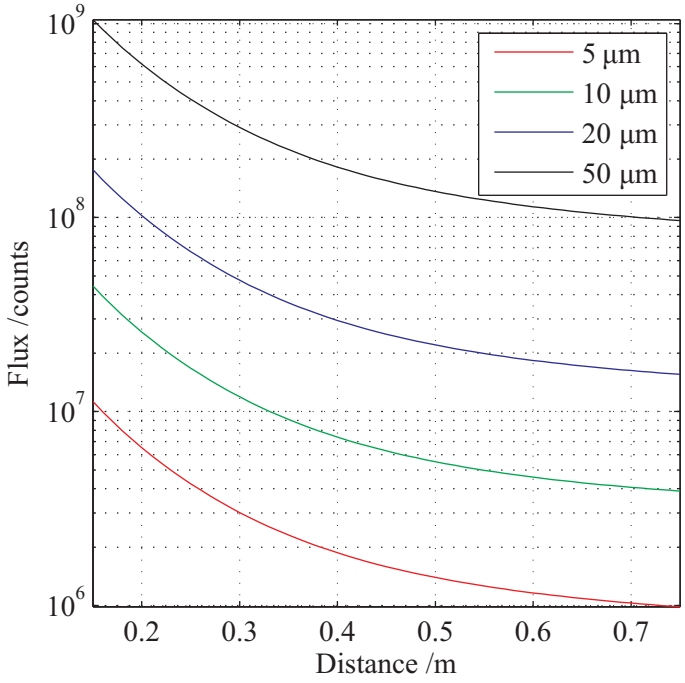

Figure 5.7: Estimated flux through various size pinholes placed at varying distances from the XUV source.

5.4 XUV Spectrum

Understanding the harmonics generated is necessary in determining the sample to use as well as the constraints. Shorter wavelengths will diffract to smaller angles, so the distance between the sample and the camera needs to be carefully determined.

Since the same generation setup and the same input parameters were used as in Section 4.2.5, then the spectrum produced is the same as measured previously (see Fig. 5.8). The intensity of the spectrum increases with increasing pressure, while the number of harmonics decreases.

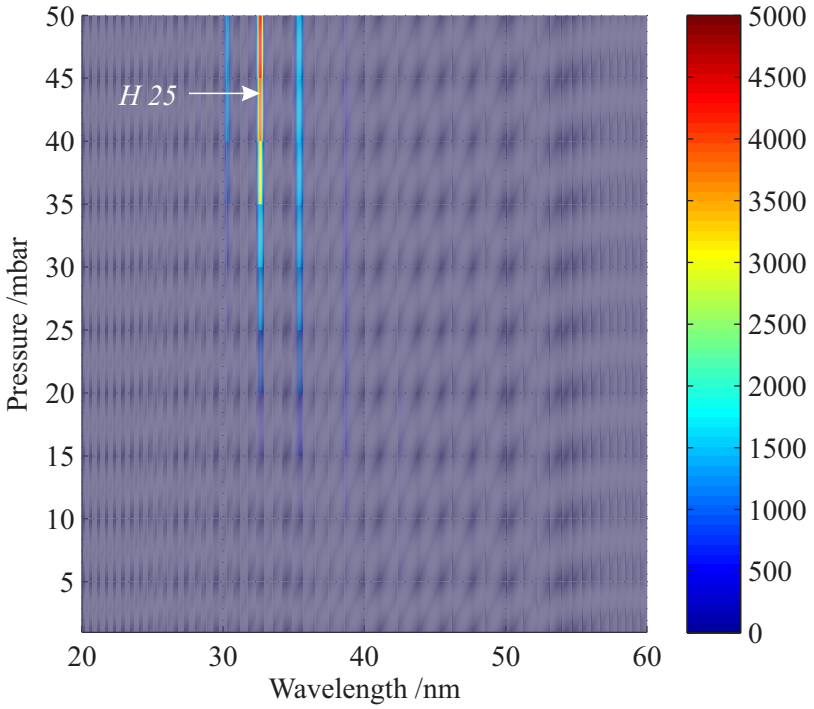

Figure 5.8: Output XUV spectrum as a function of pressure.

At 15 mbar, the 21st harmonic (~ 38 nm) is more intense than the other harmonics. However, the flux at this pressure is relatively low and so subsequent scattering experiments will take longer to obtain the same signal-to-noise as that obtained at higher pressures. As the pressure increases above 25 mbar, the 25th harmonic (~ 32 nm) becomes the most intense harmonic, with the peak being over twice as intense as the two next most intense harmonics.

5.4.1 Multiple Wavelength CDI

When multiwavelength radiation is scattered from an object, the observed scattering pattern is the incoherent sum of the individual patterns from each harmonic. This is demonstrated in Fig. 5.9, where successive wavelength scaled 1-dimensional scattering patterns from a 5 μm Young's slit experiment have been added together. The first plot represents the scattering pattern from one harmonic, the 21st harmonic (H 21), the second is the addition of 2 different harmonics (H 21 and H 23) and the third is the addition of three harmonics (H 21, H 23 and H 25). Visible from the plots is the reduction in modulation with increasing harmonic addition. The variation in the spatial intensity profile between the patterns means that the reconstructed object will differ when using a multiple wavelength source compared to a monochromatic source. It is therefore necessary to use radiation with as narrow a spectrum as possible for successful reconstruction.

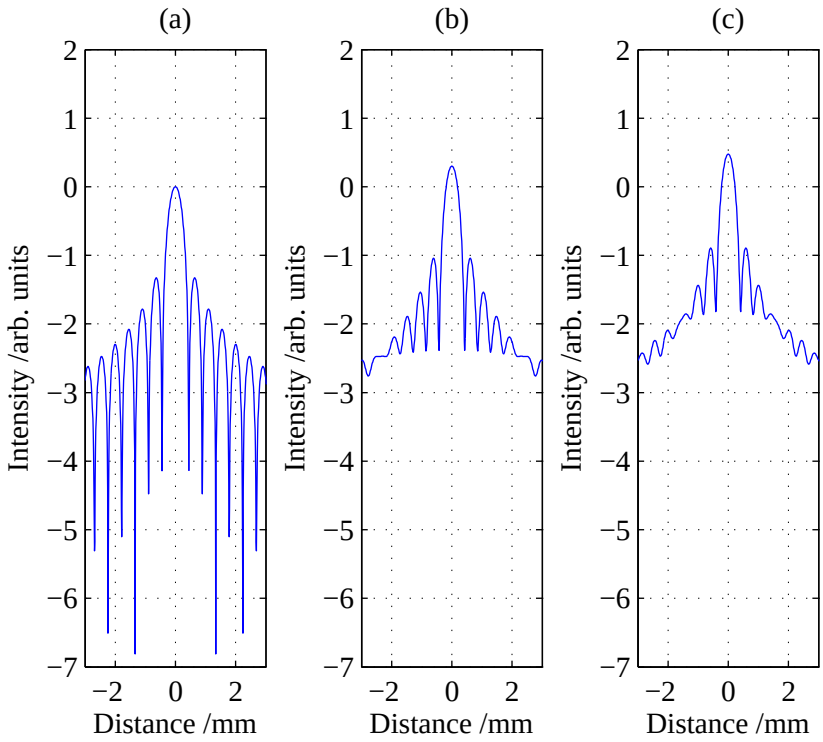

Figure 5.9: Addition of 1-dimensional scattering patterns from a single 5 μm slit using (a) one harmonic (H 21), (b) two harmonics (H 21 and H 23) and (c) three harmonics (H 21, H 23 and H 25). The intensity is displayed on a $\log_{10}$ scale.

5.5 Phase Retrieval

Although the intensity of a scattering pattern is recorded on a CCD camera, the phase information is lost. This prevents direct image replication of an object. Phase retrieval algorithms were first proposed by Gerchberg and Saxton [19], while further improvements were made by Fienup [20], who developed the error-reduction (ER) algorithm and the hybrid-input-output (HIO) algorithm. Since the HIO algorithm is faster at converging than the ER, the HIO algorithm was therefore employed in the work discussed in this chapter.

The HIO algorithm consists of the following steps:

a) Create a first estimate for the solution's electric field, $g_k(x)$, by creating an object electric field $g_k(x)$ with random phase θ_k within a defined support. The field is then Fourier transformed to give an estimate of the electric field of the scattering pattern, $G_k(u)$,

$$G_k(u) = |G_k(u)|e^{i\phi_k(u)} = \mathcal{F}\{g_k(x)e^{i\theta_k(x)}\} \tag{5.2}$$

where k is the iteration number, x is an N-dimensional spatial coordinate and u is an N-dimensional spatial frequency coordinate.

b) Replace the amplitude of the guess with the square root of the measured intensity of the experimental scattering pattern (the modulus of F) to obtain an altered electric field, $G'_k(u)$,

$$G'_k(u) = |F(u)|e^{i\phi_k(u)} \tag{5.3}$$

An apostrophe indicates an altered term.

c) Inverse Fourier transform to give the electric field in object space,

$$g'_k(x) = |g'_k(x)|e^{i\theta'_k(x)} = \mathcal{F}^{-1}\{G'_k(u)\} \tag{5.4}$$

d) Apply constraints to the object, i.e. force the density towards zero for all points x in the support region γ to obtain a new estimate of the object. For everywhere except the support region, the field is unchanged,

$$g_{k+1}(x) = \begin{cases} g_k(x) - \beta g'_k(x), & x \in \gamma \\ g'_k(x), & x \notin \gamma \end{cases} \tag{5.5}$$

Here, β is a constant between 0 and 1.

Initially, there is assumed to be a non-zero intensity region in object space which contains the object. This is known as the mask. The initial guess of the object, which contains both amplitude and phase, is Fourier transformed to generate the first estimate of the scattering pattern. Once in image space, the amplitude of the scattering pattern is replaced with the square root of the experimentally observed intensity, so that the spatial information of the object is obtained. The phase is left unchanged and the result is then inverse Fourier transformed. Once in object space, the intensity outside of the mask is reduced. Since there is no object outside of the mask, no spatial information about the object is lost. The cycle is repeated for a number of iterations until the error between the reconstructed scattering pattern and the experimental scattering pattern has reached a certain value.

The phase retrieval can be further accelerated by employing the Shrinkwrap method developed by Marchesini *et al.* [108]. Instead of using a support that is only constructed by an estimate of the object's size, the Shrinkwrap method uses a blurred version of the autocorrelation function as its first mask. Further to this, the Shrinkwrap method refines the support periodically by thresholding the intensity of a blurred version of the current estimate

of the object. The Shrinkwrap attempts to reduce the size of the mask by combining pixels that have intensities greater than a defined value to form a smaller mask. This mask is still bigger than the object so no spatial information about the object is lost. The HIO algorithm used in this thesis employs Shrinkwrap. It is displayed schematically in Fig. 5.10.

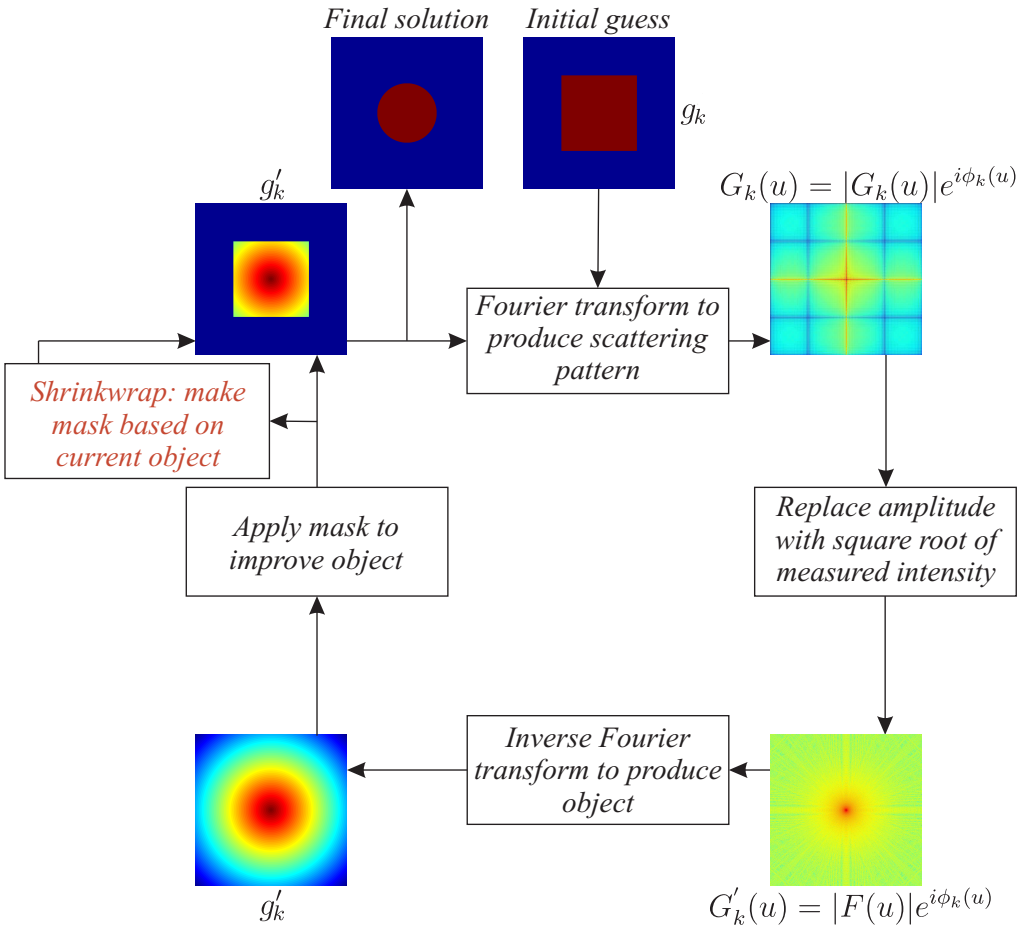

Figure 5.10: HIO phase retrieval algorithm employing the Shrinkwrap.

5.5.1 Geometric Requirements

In order to achieve successful CDI, there are two geometrical requirements that must be considered. The first is that the highest resolution image (the smallest reconstructed image pixel size) obtained occurs when the object is closest to the camera. However, contradictory to this requirement is the convergence of the algorithm to a solution which favours the camera being as far away from the object as possible. This is known as the oversampling ratio and corresponds to the ratio between the area of the mask and the zero density area outside the mask, and the area of mask itself. Oversampling ratios of 2 are required to obtain a reconstructed solution. However, ideally this value should be at least 5 [109] since a larger

oversampling ratio as possible will improve convergence. Figure 5.11 shows a schematic of the imaging setup.

The oversampling ratio, defined as $O = D_{pixel}/D_{object}$, can be derived from the diagram using the small angle approximation and is defined geometrically as [110],

$$O = \frac{z\lambda}{pD_{object}} \tag{5.6}$$

where z is the sample to CCD camera distance, λ is the wavelength, p is the CCD camera pixel size and D_{object} is the size of the sample. The image pixel size is also derived from Fig. 5.11 and is given by,

$$D_{image} = \frac{z\lambda}{pN} \tag{5.7}$$

where N is the number of CCD camera pixels. Upon looking at the two equations, it is clear that although increasing z will increase the oversampling ratio O, this will increase the image pixel size D_{image} and therefore decrease resolution of the reconstructed object. Since z, λ and p are present in both equations and N is a constant in Equation 5.7, then D_{object} must be reduced in order to obtain as high oversampling ratio and resolution as possible.

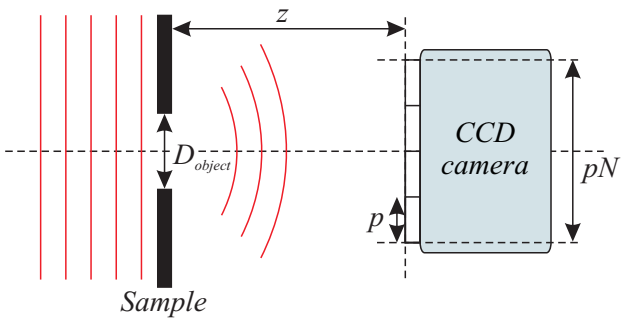

Figure 5.11: Schematic of CDI imaging setup.

The two equations above are plotted in Fig. 5.12, displaying (a) the oversampling ratio and (b) the image pixel size as a function of the sample to CCD camera distance. Due to the shape of the camera, the minimum distance at which an object can be placed is 17 mm. This is represented by a black dashed line in the plots. In view of this fact, objects that are no larger than 5 μm must be used at this distance for an oversampling ratio of 5. It is possible to use an object as large as 10 μm to obtain 100 nm resolution, but it must be placed approximately 50 mm away from the CCD camera. Since the oversampling ratio for 50 μm

and even 20 µm diameter samples does not increase sufficiently above 5 for pixel resolution below 100 nm, such sized objects are not considered in this work.

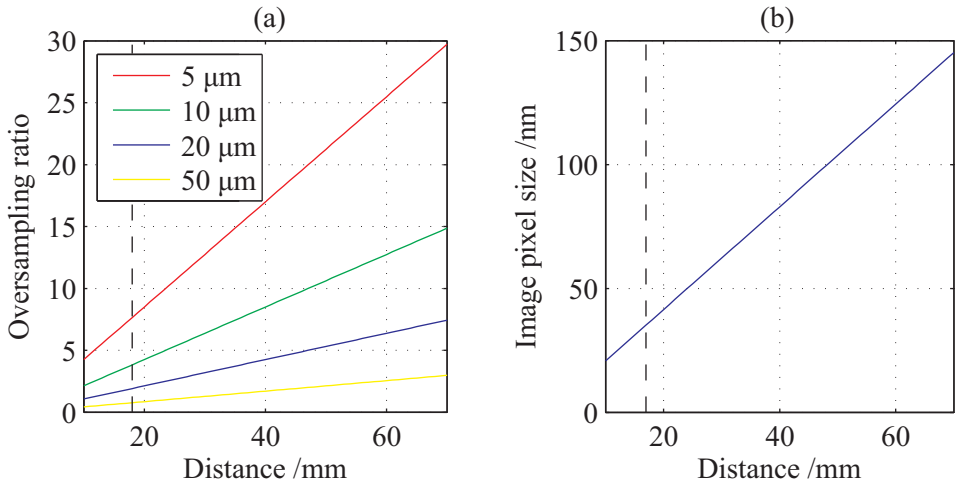

Figure 5.12: (a) The oversampling ratio for 5 µm (red), 10 µm (green), 20 µm (blue) and 50 µm (yellow) diameter samples as a function of sample to CCD camera distance. The data are calculated using Equation 5.6. (b) Reconstructed image pixel size as a function of sample to CCD camera distance. The data are calculated using Equation 5.7. The vertical dashed line represents the minimum possible CCD camera to sample distance due to the experimental setup.

5.6 Coherent Diffractive Imaging of an Aperture

In this section, experimental results that demonstrate the imaging of a symmetric micron-sized object using the technique of CDI are discussed. The object used as the sample in the experiment is a 5 µm diameter pinhole. The purpose of using such a sample is that it is a simple shape of known size and thus any object reconstruction can be compared easily. This will aid in the understanding of the imaging process before moving to more complex objects. The size of the pinhole is chosen so that not only will a Fraunhofer diffraction pattern be obtained on the CCD camera, but also so that the oversampling ratio is much greater than 2. Since future work will involve objects of approximately this size, experimenting with such an object is a good starting point.

5.6.1 5 µm Pinhole Sample

An optical transmission microscope image of the 5 µm pinhole is shown in Fig. 5.13. The pinhole is made in an aluminium disc that is 50 µm thick and 1 cm in diameter and is attached to the sample mount using vacuum compatible carbon tape. The image is unfocused

due the limitation of the microscope. For objects with smaller structure, SEM images are used for comparison.

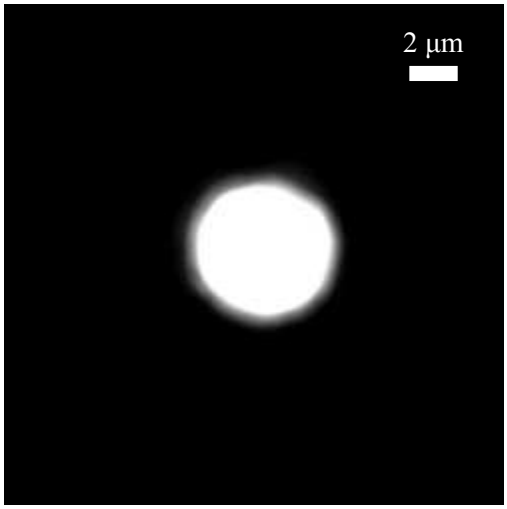

Figure 5.13: Optical transmission microscope image of the 5 μm pinhole.

5.6.2 Experimental Results

The data was recorded at a sample to CCD camera distance of 46 mm. This corresponds to a Fresnel number of ~ 0.04, and hence the recorded scattering pattern is in the Fraunhofer regime. A set of six scattering patterns at 35 mbar backing pressure were recorded for 5 seconds each and a single image was recorded for 30 seconds at the same pressure. The 5 second images are unsaturated and thus contain low spatial frequencies information. However, due to the short integration time, the high spatial frequencies are below the noise and are therefore not readable. A longer exposure of 30 seconds was necessary to obtain high spatial frequency signal that was above the noise. By replacing the oversaturated pixels of the 30 second integration image with 6 lots of unsaturated pixels, a scattering pattern that contains both the high and low spatial frequencies is obtained. The two sets of scattering patterns are displayed in Fig. 5.14. The saturated pixels (red pixels) in the left image are replaced by the unsaturated pixels from the right image.

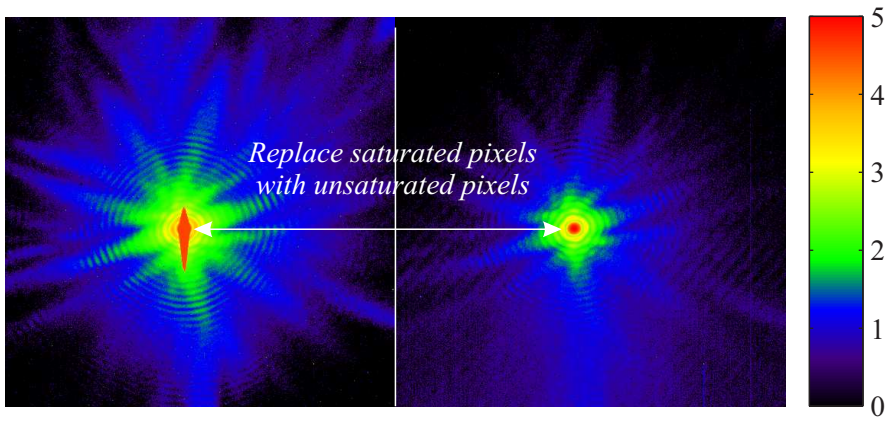

Figure 5.14: Experimentally observed scattering pattern of the 5 µm pinhole. The pattern on the left is a 30 seconds integrated pattern and the pattern on the right is a 5 seconds integrated pattern. The saturated pixels of the left image are replaced with unsaturated pixels from the right. The intensity scale is log_{10} and the images are 1024 x 1024 pixels in size.

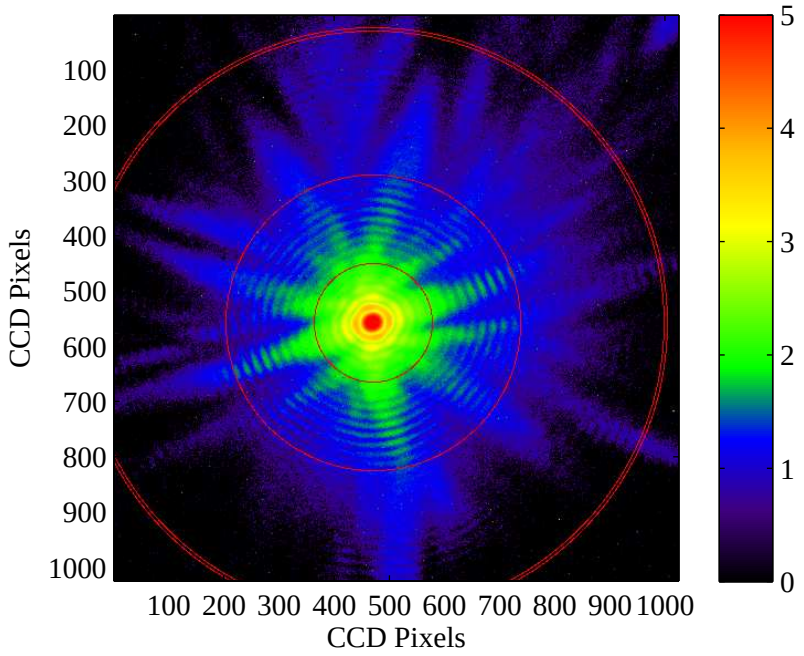

Figure 5.15: Experimentally observed scattering pattern of the 5 µm pinhole. The pattern consists of a 30 second integrated pattern with the saturated pixels replaced by unsaturated pixels. The red rings indicate potential reconstructed object resolution. The inner ring corresponds to 500 nm, the next ring corresponds to 200 nm and the outer double ring corresponds to 100 nm.

Figure 5.15 shows the spliced image displayed on a $\log_{10}$ scale. Labelled on the plot are rings that indicate the potential resolution of the reconstructed object. The inner ring corresponds to 500 nm, the next ring corresponds to 200 nm and the outer double ring corresponds to 100 nm. Figure 5.16 shows the average signal versus potential resolution obtained by taking the mean of the intensity in circles about the image centre. Due to the diffraction limit, the maximum possible resolution of reconstruction is that at the corner of the CCD camera. In this instance, it is ~ 70 nm. The most likely resolution attainable corresponds to the highest spatial frequency that has signal above the noise. The highest possible resolution can therefore be increased by recording the scattering pattern over a longer period so that a higher signal-to-noise is obtained at high spatial frequencies.

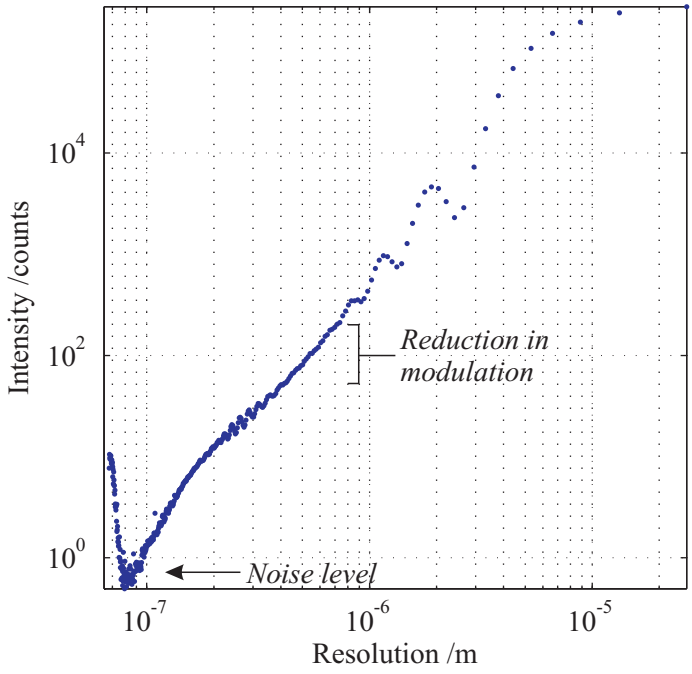

Figure 5.16: Intensity vs. resolution obtained by calculating the average intensity in circles of the scattering image. The most likely highest resolution possible from reconstruction corresponds to where the signal drops to the noise level.

It is evident that a resolution between 100 nm and 200 nm could be achieved if the algorithm converges correctly. The increase in the peak at below 100 nm is a consequence of the scattering pattern being off centre and the way in which the resolution is calculated. For resolution below 100 nm, the circles contain signal above the noise in the top right of the image in Fig. 5.15, but contain no data for the regions where the circle is outside the pattern.

Since regions of potentially low signal are therefore not taken into account in the averaging, the average intensity below 100 nm is relatively high.

Also from the resolution plot, it is possible to see the effect of multiple wavelength scattering. Reduction in modulation between 400 nm and 900 nm is visible.

5.6.3 Algorithmic Process

The algorithm ran for 4000 iterations with a new mask and Shrinkwrap being employed initially every 500 iterations for the first two uses and then 1000 iterations thereafter. The initial guess is formed from the autocorrelation of the observed scattering pattern and is displayed in Fig. 5.17, where (a) is the starting intensity and (b) is the starting phase in radians.

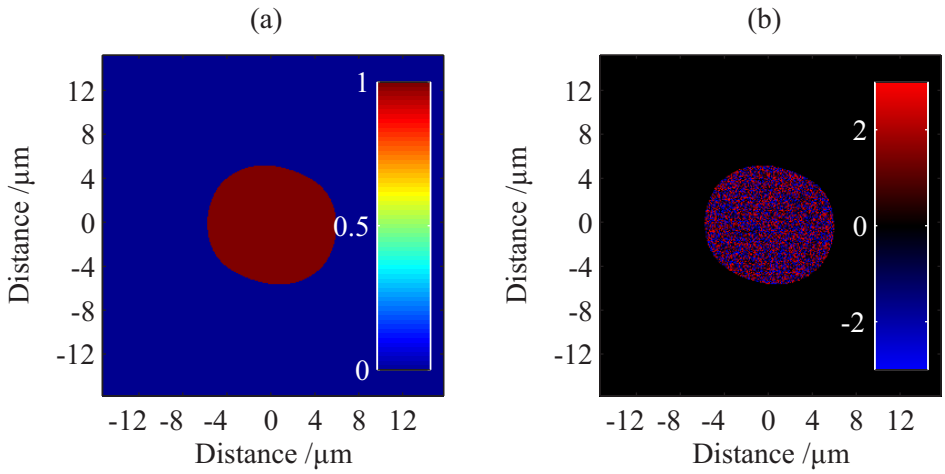

Figure 5.17: Initial guess for (a) the sample intensity and (b) the sample phase (in radians).

Various stages of the algorithmic process are shown in Fig. 5.18, displaying both the reconstructed intensity (LHS) and preceding mask (RHS). On the 500th iteration, a circle is already being reconstructed. On the subsequent iterations, the mask shrinks down as the algorithm tends towards a solution. Both the mask and the intensity profile of the object shrink to a size of ~ 5 µm by the 3000th iteration.

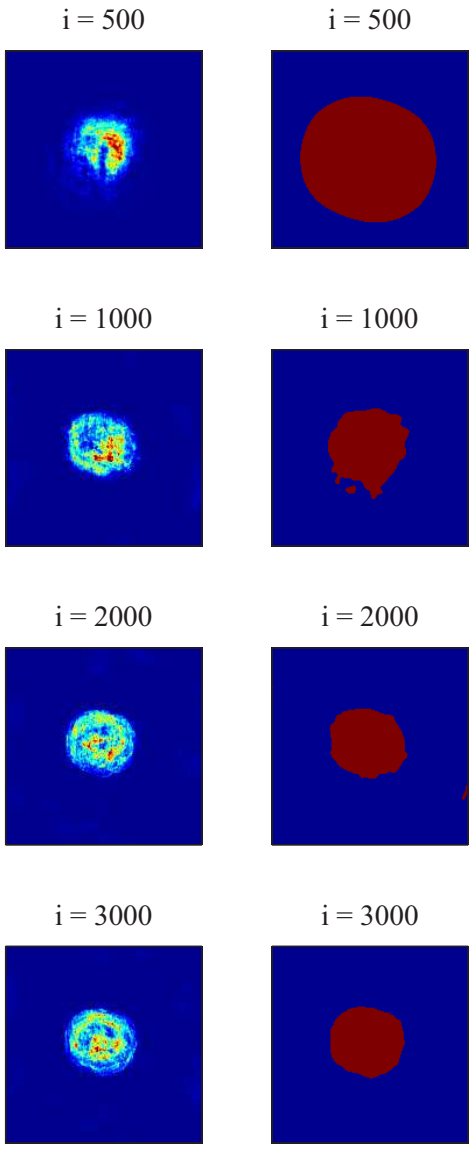

Figure 5.18: Intensity (LHS) and preceding mask (RHS) for iteration steps 500, 1000, 2000 and 3000.

The final solution of the intensity and phase is displayed in Fig. 5.19. A pinhole has been reconstructed and is of approximately the correct size, though the intensity is not as uniform as expected from a small fraction of the incident XUV beam. Although the phase of the XUV beam should be relatively flat at this distance from the source, the reconstruction shows that a slope across the beam. This is because the scattering pattern is off-centre on the CCD camera. The algorithm attributes this offset to a phase shift caused by a scattered beam being incident on a CCD camera at an angle. As such, the phase shift across the reconstructed object will be greater for a larger scattering pattern offset.

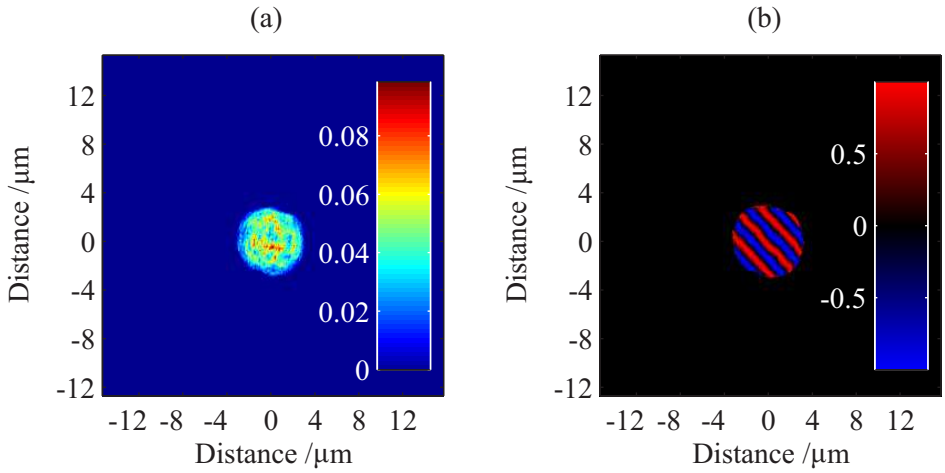

Figure 5.19: Final solution for (a) the intensity and (b) the phase (in radians) displayed in the form cos(φ) in order to illustrate the phase modulations. The non-uniform reconstructed intensity is due to the observed scattering pattern containing signal from multiple wavelength radiation.

The Fourier error is the difference between the reconstructed scattering pattern and the observed scattering pattern [111],

$$error^2 = \frac{\sum\left||G_k| - |F|\right|^2}{\sum|F|^2} \tag{5.8}$$

The final error per Shrinkwrap cycle is displayed in Fig. 5.20 (a). The figure shows that the error starts to plateau by the fourth implementation of the Shrinkwrap. The Fourier error for the final 1000 iterations, displayed in Fig. 5.20 (b), shows that after an initial drop the error increases slightly and then flattens. The initial high error and then sharp decrease in Fig. 5.20 (b) is due to the effect of Shrinkwrap having just taken place. The error increases thereafter because the algorithm is converging to a solution for a single wavelength scattering pattern but the observed pattern contains signal from multiple wavelengths.

Although the algorithm does not work by using the error to improve the solution (it is merely a by-product of the iterations), from the error it is still possible to tell whether the algorithm has stagnated and found a solution, as with this reconstruction of the 5 µm pinhole.

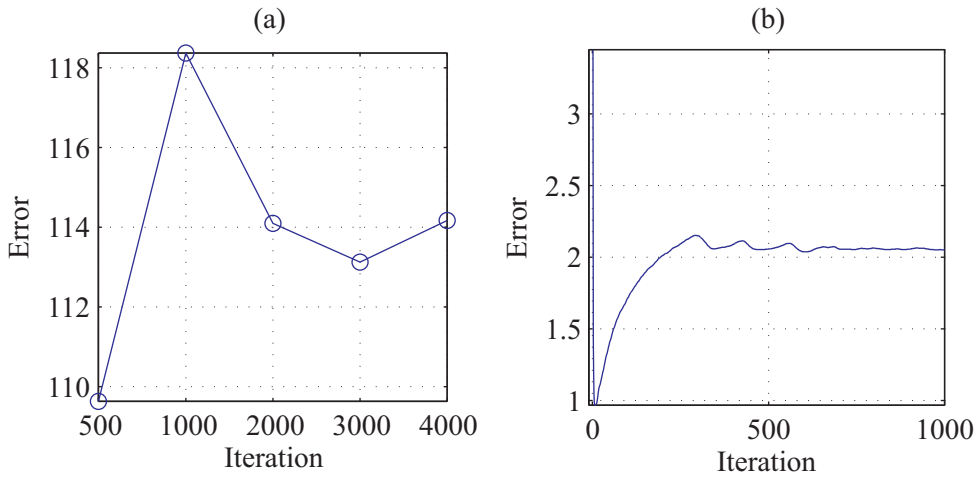

Figure 5.20: (a) Final Fourier error per Shrinkwrap cycle and (b) Fourier error displayed on a $\log_{10}$ scale for the final 1000 iterations of reconstruction of the 5 μm pinhole. The data are calculated using Equation 5.8.

5.7 Coherent Diffractive Imaging of a FIB Sample

Although a 5 μm pinhole has been imaged, it was necessary that a less symmetric shape be explored in order to further understand the CDI process. By choosing a sample that was non-symmetric, a better grasp of the algorithmic constraints would be obtained. In addition, an object consisting of a variety of shapes and sizes would test the resolution of the nanoscope. The letters *ORC* in Georgian font at a size < 7.5 μm were therefore chosen as the object. The reconstruction of a sample of this size and shape is the next step towards a sub-micron sample.

5.7.1 ORC FIB Sample

A 500 x 500 μm square, 50 nm thick, silicon nitride window was chosen as the canvas for the sample. The window can survive gas pressure differentials present in the vacuum setup and can be coated in substrates suitable for etching [112]. For the XUV wavelengths used in this work, the 50 nm silicon nitride transmits ~ 10 % of the radiation. The window was coated with a 110 nm thick gold layer that transmits ~ 5 x 10^{-3} of the radiation. In this way, significant contrast in transmission is achieved between regions that have been etched all the way through the coated window and regions that have not been etched at all.

The sample is shown in Fig. 5.21. The drilling was done by Jun-Yu Ou using a focused ion beam (FIB). The *O* of the *ORC* is about 2.5 μm wide, the legs of the *R* are less than a micron wide and the tips and tails of the *R* and *C* are < 300 nm wide.

The faint square shape that can be seen on the window is the result of using ions to image the sample during alignment for drilling. This however is not deep enough to allow significant transmission of XUV. As with the 5 μm pinhole, the distance between the CCD camera and the sample is 46 mm. In this instance, the Fresnel number is ~ 0.08.

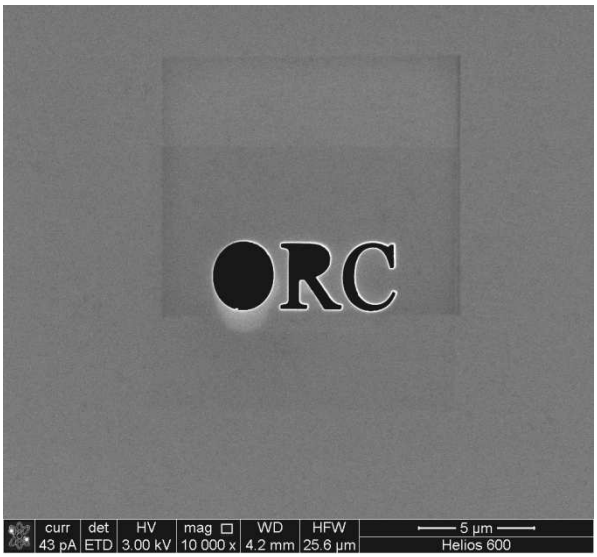

Figure 5.21: SEM image of the ORC FIB sample.

5.7.2 Experimental Results

Scattering patterns were recorded at 35 mbar for two different integration times, 60 seconds and 300 seconds, corresponding to unsaturated and oversaturated images respectively. Figure 5.22 shows two sets of scattering patterns. The 300 second integrated scattering pattern is on the left and the 60 second integrated scattering pattern is on the right. The images were then spliced together so that an image containing signal above the noise for both high and low spatial frequencies is obtained. The red pixels in the centre of the pattern in left image are saturated and were replaced by the unsaturated pixels from the right image.

The result of replacing the saturated pixels of the 300 seconds with five lots of 60 second data is shown in Fig. 5.23. Once again, rings indicating the potential resolution of the reconstructed object are marked on the figure. The maximum resolution attainable due to the diffraction limit is ~ 70 nm. From the image, there is some signal that is near the 100 nm resolution ring (the outer ring). However, the signal is small and the average signal is not above the noise. Such resolution of the reconstructed object is therefore unlikely.

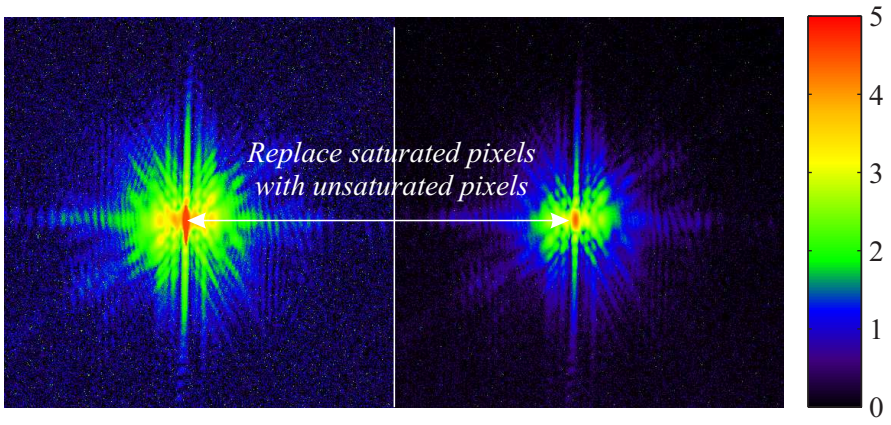

Figure 5.22: Experimentally observed scattering pattern of the ORC FIB sample. The pattern on the left is a 300 second integrated pattern and the pattern on the right is a 60 second integrated pattern. The saturated pixels of the left image are replaced with unsaturated pixels from the right. The intensity scale is $\log_{10}$ and the images are 1024 x 1024 pixels in size.

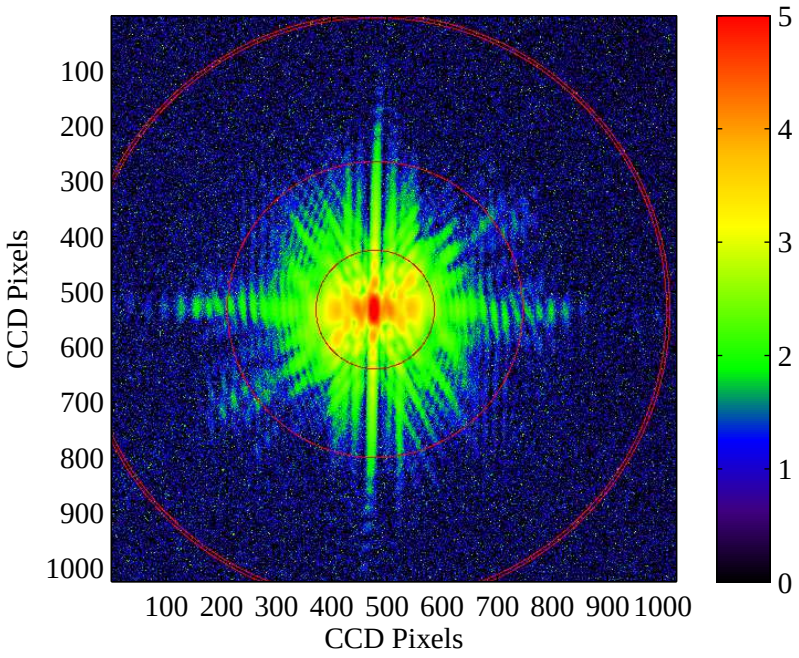

Figure 5.23: Experimentally observed scattering pattern of the ORC FIB sample. The pattern consists of a 300 second integrated pattern with the saturated pixels replaced by unsaturated pixels. The red rings indicate potential reconstructed object resolution. The inner ring corresponds to 500 nm, the next ring corresponds to 200 nm and the outer double ring corresponds to 100 nm.

Indeed, from Fig. 5.24, the most likely highest spatial resolution attainable for the reconstructed object is ~ 200 nm, since this is the highest spatial resolution above the noise.

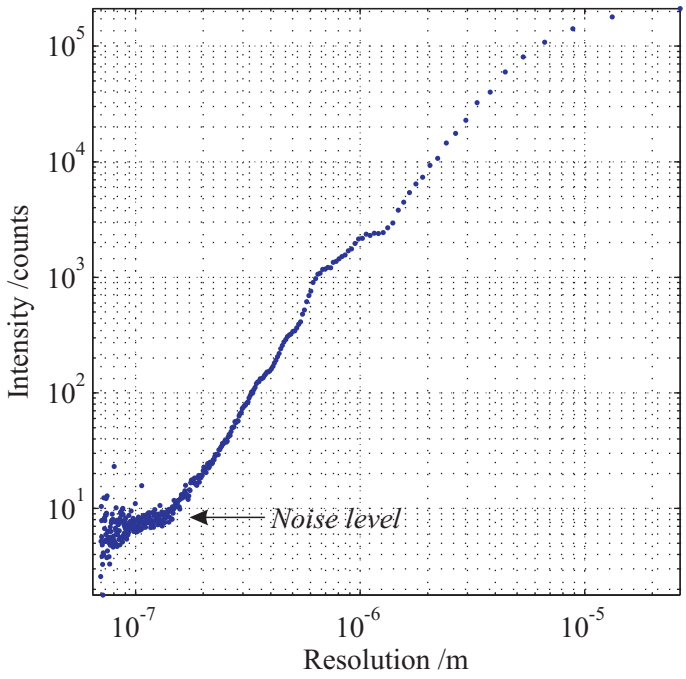

Figure 5.24: Intensity vs. resolution obtained by calculating the average intensity in circles of the scattering image. The most likely highest resolution possible from reconstruction corresponds to where the signal drops to the noise level.

5.7.3 Algorithmic Process

Again, the autocorrelation of the experimentally observed scattering pattern was used as the initial guess for the sample mask. Figure 5.25 shows the initial starting guess for the algorithm. The algorithm ran for 6500 iterations and employed the Shrinkwrap initially every 250 iterations for the first two uses, then every 1000 iterations for the next three, before finally employing it every 500 iterations.

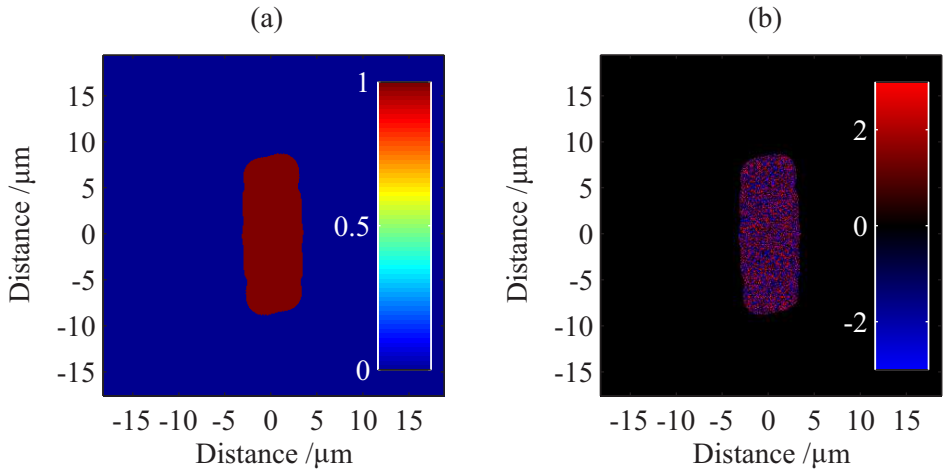

Figure 5.25: Initial guess for (a) the sample intensity and (b) the sample phase (in radians).

The 250th, 1000th, 2000th and 4000th iterative steps are displayed in Fig. 5.26. As with the iterative steps for the pinhole, the reconstructed intensity is on LHS and the mask used to reconstruct that intensity is on the RHS. After 250 iterations, an oblong shaped object has been reconstructed. By the 1000th iteration, the mask has shrunk and the object intensity has split into three. On the 2000th iteration, a reconstructed *O* and *C* are visible (albeit mirrored due to sample's orientation in the setup). After a further 2000 iterations, the object and mask have separated into three letters and the letter *R* is produced.

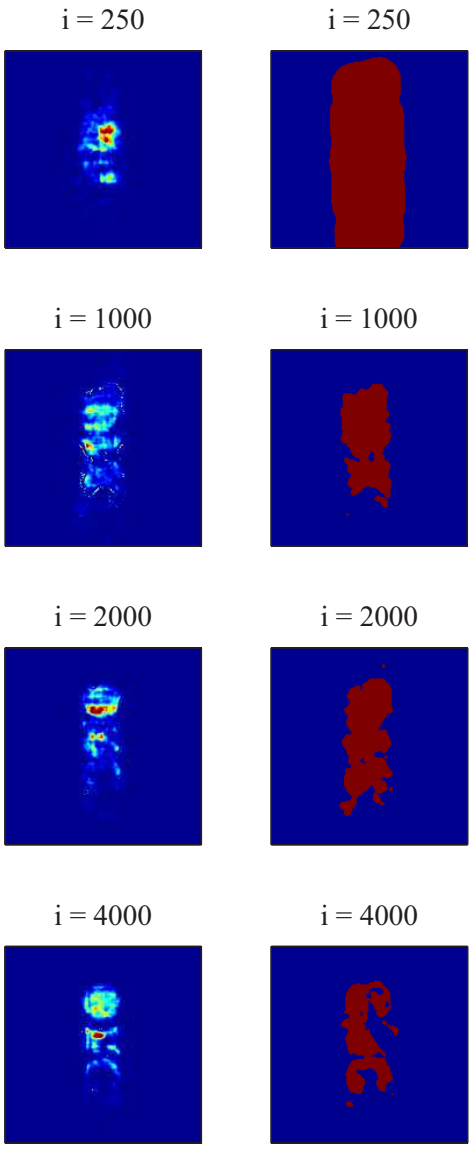

Figure 5.26: Intensity (LHS) and preceding mask (RHS) for iteration steps 250, 1000, 2000 and 4000.

The final solution, displayed in Fig. 5.27, shows that the algorithm has been able to converge to a solution after 6500 iterations. All three letters in order, *ORC*, have been reconstructed. As displayed in Fig. 5.28 (a) and (b), the error reaches a plateau for both the final Fourier error per Shrinkwrap cycle and the Fourier error for the final 500 iterations. At this point, further iterations did not improve object reconstruction.

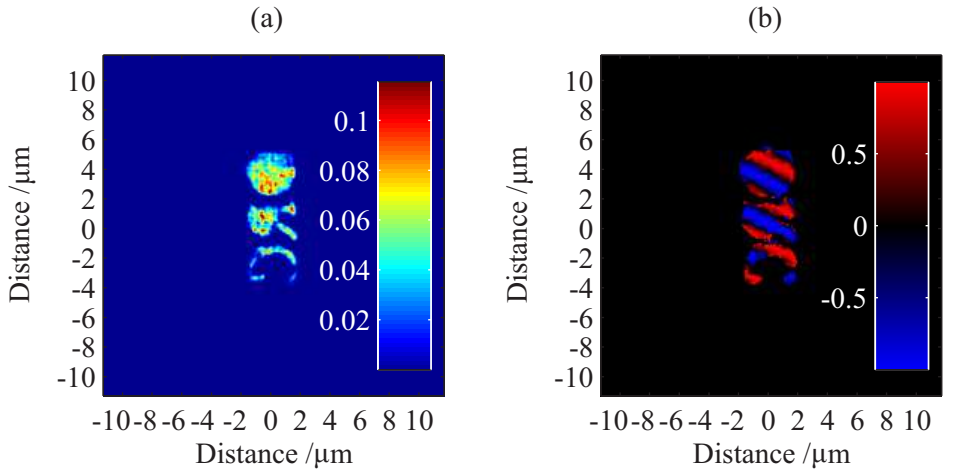

Figure 5.27: Final solution for (a) the intensity and (b) the phase (in radians) displayed in the form cos(φ) in order to illustrate the phase modulations. The letters are mirrored due to sample's orientation in the setup.

Comparing Fig. 5.27 (a) with the SEM image in Fig. 5.21, it is evident that the tails of the *C* and the *R* have been reconstructed. These are ~ 300 nm wide. Upon looking at Fig. 5.27 (b), the phase is sloped across the sample. However, the gradient is not as large as with the pinhole. Indeed, on comparing the two scattering patterns, Fig. 5.15 and Fig. 5.23, the offset of the *ORC* scattering pattern from the centre of the CCD camera is significantly less than that of the 5 µm pinhole.

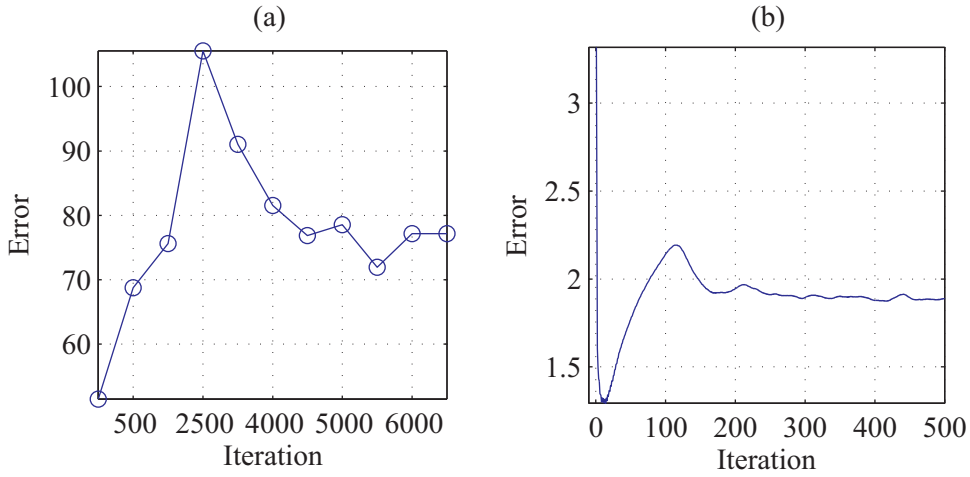

Figure 5.28: (a) Final Fourier error per Shrinkwrap cycle and (b) Fourier error displayed on a $\log_{10}$ scale for the final 500 iterations of reconstruction for the ORC FIB sample. The data are calculated using Equation 5.8.

5.8 Coherent Diffractive Imaging of a Biological Sample

In the previous section, the imaging of a non-symmetric object with resolution of ~ 300 nm was demonstrated. In this section, a biological sample known as a diatom is imaged. A diatom is a type of algae with walls made of silica. Each species has its own unique shape and has structure consisting of interconnected pores [113]. In the experiment described in this section, a non-symmetric dehydrated diatom fragment that has complex features on both the micron and nanometre scale is used. Not only is imaging a diatom an important step in the development of the nanoscope, but understanding its structure at nanoscale dimensions has potential uses in both biology and photonics [114,115].

5.8.1 Diatom Sample

The diatom used in this experiment was from flea powder (DE-Sign of Nature). The flea powder is diatomaceous earth made from the fossilized skeletal remains of diatoms. The sample was made by adding diatoms to methanol (1 part diatoms to 5 parts methanol) and then evaporating the solution on a 500 x 500 μm square, 50 nm thick, silicon nitride window. So that only one diatom was to be imaged and so that Fraunhofer diffraction would be observed on the CCD camera, a 10 μm diameter aluminium pinhole was used to aperture a diatom (see Fig 5.29). Carbon tape was used to attach the window to the pinhole.

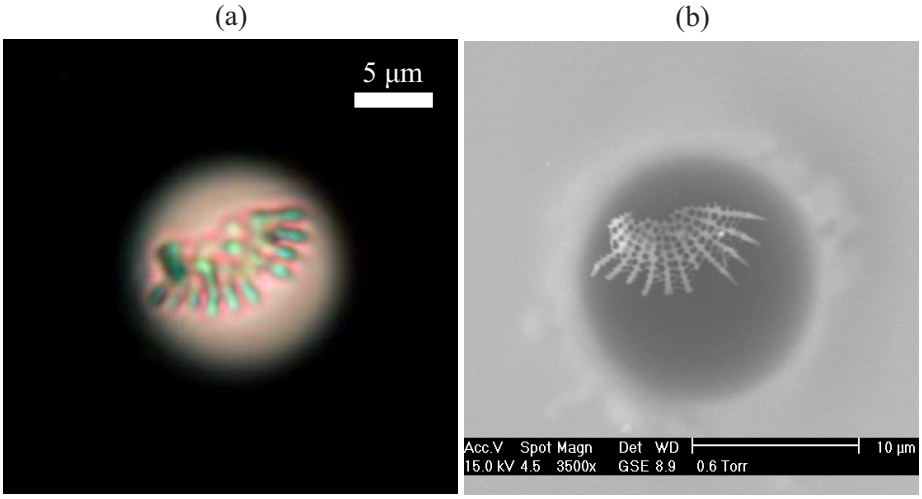

Figure 5.29: (a) Optical transmission microscope image and (b) SEM image of the diatom in a 10 μm pinhole.

It is clear that when looking at the microscope image in Fig. 5.29 (a), ~ 500 nm ridges are present in the structure of the diatom. Visible from the SEM image in Fig. 5.29 (b) are

also ~ 100 nm diameter holes in the diatom. Structure of such size is potentially resolvable using CDI with XUV radiation.

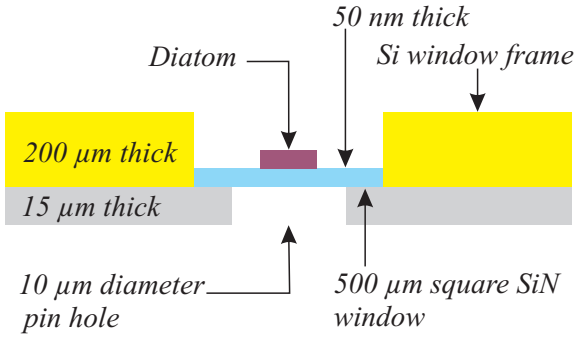

Figure 5.30: Cross-section schematic of the diatom sample setup.

A cross-section schematic of the sample setup is shown in Fig. 5.30. Since the diatom is made from SiO_2 with walls of estimated thickness of at least ~ 100 nm, the transmission of XUV radiation through though the diatom is $< 1 \times 10^{-3}$. As such, with the wall of the pinhole being 15 μm thick and therefore blocking XUV radiation, only radiation passing inside the pinhole and around and through the open structure of the diatom will be scattered to the CCD camera. Again, the 50 nm silicon nitride transmits ~ 10 % of the XUV radiation.

5.8.2 Experimental Results

In order to improve the resolution of the nanoscope, the filter system was adjusted so that higher pressures and thus radiation with fewer harmonics could be used. A series of scattering patterns were recorded at a pipe input pressure of 45 mbar for a variety of integration times. The minimum integration time of the images was 5 seconds and the maximum integration time was 1440 seconds. Simply splicing 5 second images to 1440 second images would not work because the saturation in the latter pattern had spread to high spatial frequencies that were below the noise for the unsaturated scattering pattern (see Fig. 5.31). Therefore, it was necessary to also splice using data from images integrated for 30 seconds, 60 seconds, 120 seconds and so on. Figure 5.32 shows the spliced scattering pattern. Again, rings are plotted to indicate the potential resolution of the reconstructed object.

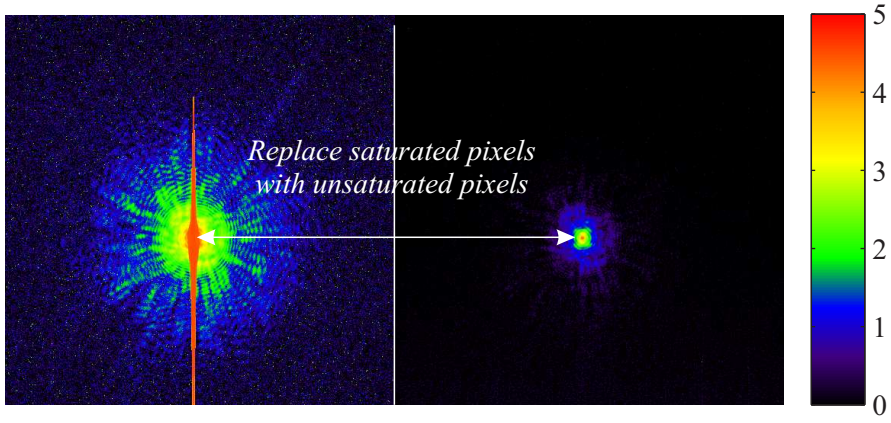

Figure 5.31: Experimentally observed scattering pattern from the diatom sample. The pattern on the left is a 1440 second integrated pattern and the pattern on the right is a 5 second integrated pattern. The saturated pixels of the left image are replaced with unsaturated pixels from the right. The intensity scale is $\log_{10}$ and the images are 1024 x 1024 pixels in size.

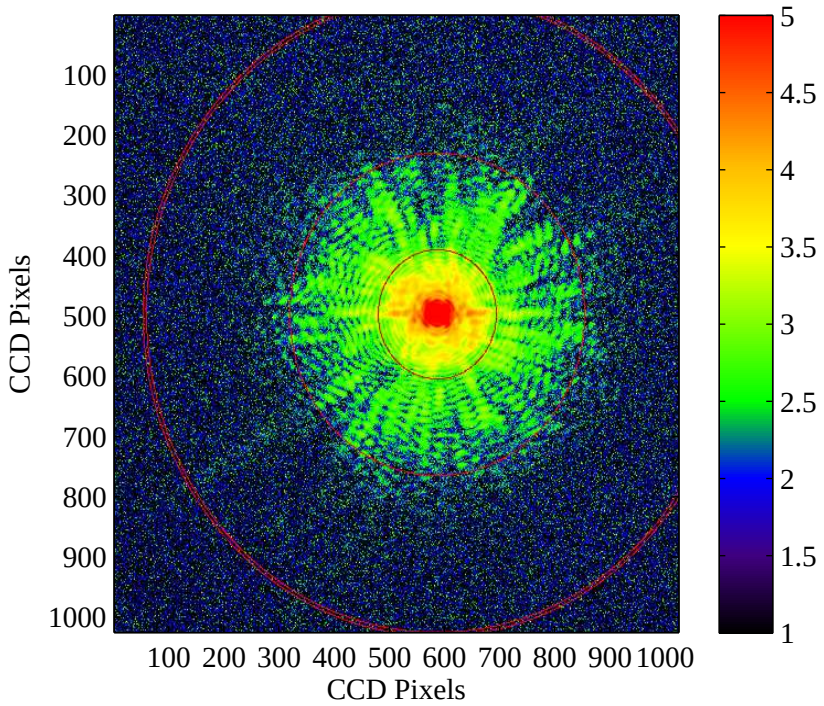

Figure 5.32: Experimentally observed scattering pattern from the diatom sample. The pattern consists of four 1440 second integrated pattern with the saturated pixels replaced by unsaturated pixels. The red rings indicate potential reconstructed object resolution. The inner ring corresponds to 500 nm, the next ring corresponds to 200 nm and the outer double ring corresponds to 100 nm.

Due to the diffraction limit, the maximum possible resolution of object reconstruction is ~ 70 nm. However, it is clear that from both Fig. 5.32 and Fig. 5.33 the signal drops to the noise at a resolution of ~ 200 nm. This is therefore the most likely highest resolution attainable for the reconstructed object.

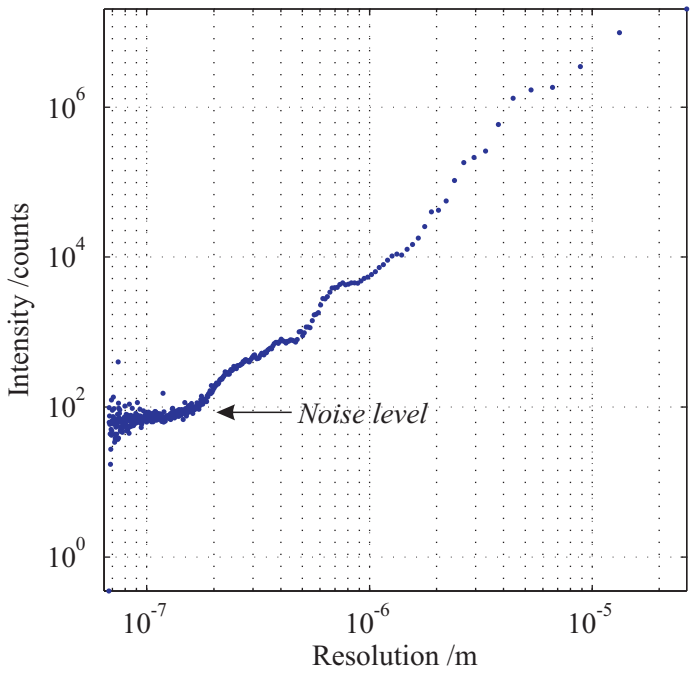

Figure 5.33: Intensity vs. resolution obtained by calculating the average intensity in circles of the scattering image. The most likely highest resolution possible from reconstruction corresponds to where the signal drops to the noise level.

5.8.3 Algorithmic Process

The initial guess for the diatom is displayed in Figure 5.34. Fig. 5.34 (a) shows the starting intensity and Fig. 5.34 (b) shows the starting phase.

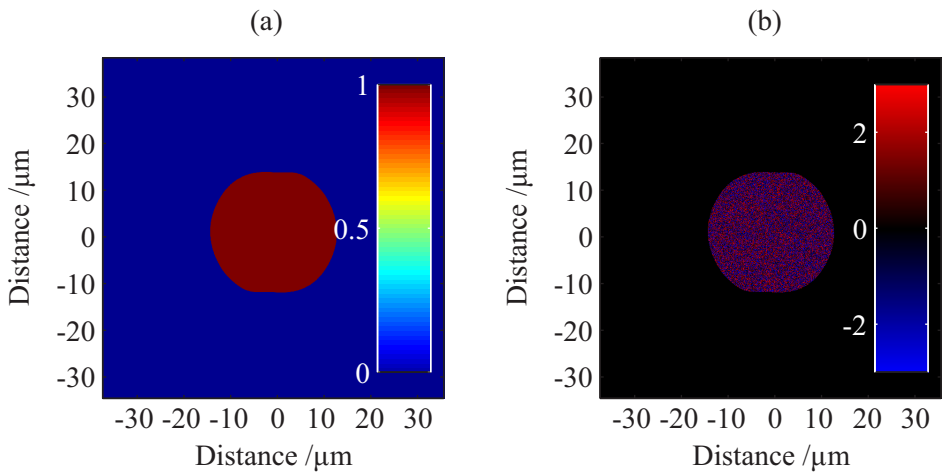

Figure 5.34: Initial guess for (a) the sample intensity and (b) the sample phase (in radians).

The algorithm ran for 6000 iterations and the Shrinkwrap algorithm was employed every 500 iterations. Various stages displaying the reconstructed intensity and preceding mask are shown in Fig. 5.35. For the 500th iteration, the mask has shrunk to the approximate size of the pinhole. By the 1500th iteration, a large region of zero intensity inside the pinhole has formed. A further 1000 iterations produces the crescent shape of the diatom inside the pinhole and by the 4500th iteration, the edges of the pinhole have become more defined.

The final solution, displayed in Fig. 5.36, shows the object reconstruction after 6000 iterations. Although the crescent shape and orientation is the same as that in the microscope and SEM image, no structure on the scale below ~ 500 nm was reconstructed. The algorithm was run for longer, but the reconstruction worsened. The inability to reconstruct to a resolution close to the ORC FIB sample implies that even with a spectrum consisting of fewer harmonics, the signal-to-noise on the scattering pattern is too low at high spatial frequencies. On comparing the scattering patterns of the diatom and the ORC FIB sample, the signal-to-noise at the higher spatial frequencies is less for the diatom. In addition, the oversampling ratio for the diatom is only 10, whereas the oversampling ratio for the ORC FIB sample was 21.

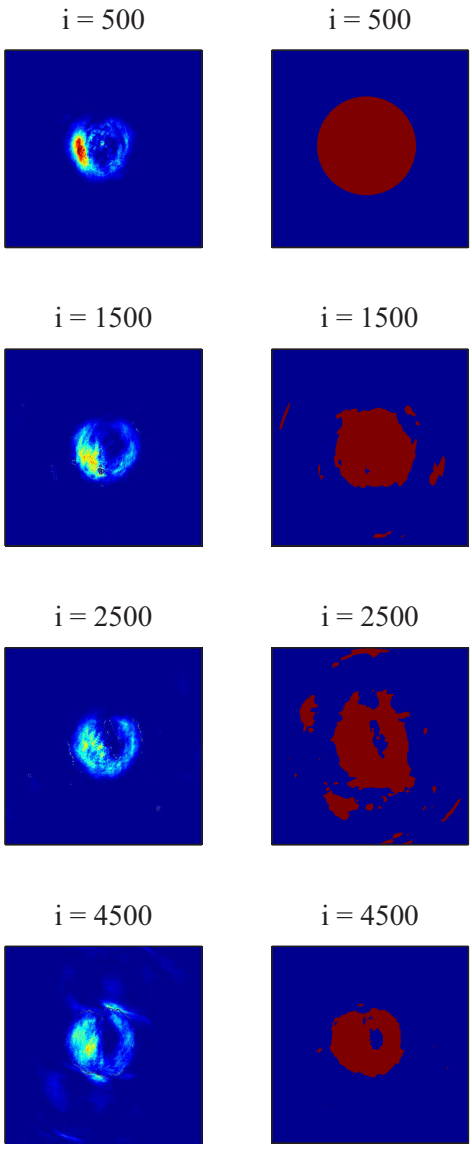

Figure 5.35: Intensity (LHS) and preceding mask (RHS) for iteration steps 500, 1500, 2500 and 4500.

The reconstructed phase displayed in Fig. 5.36 (b) has a significant slope, specifically in one direction with significantly greater gradient than that observed with the other two samples. Indeed, the scattering pattern is more offset from the centre of the CCD camera in the *x*-direction.

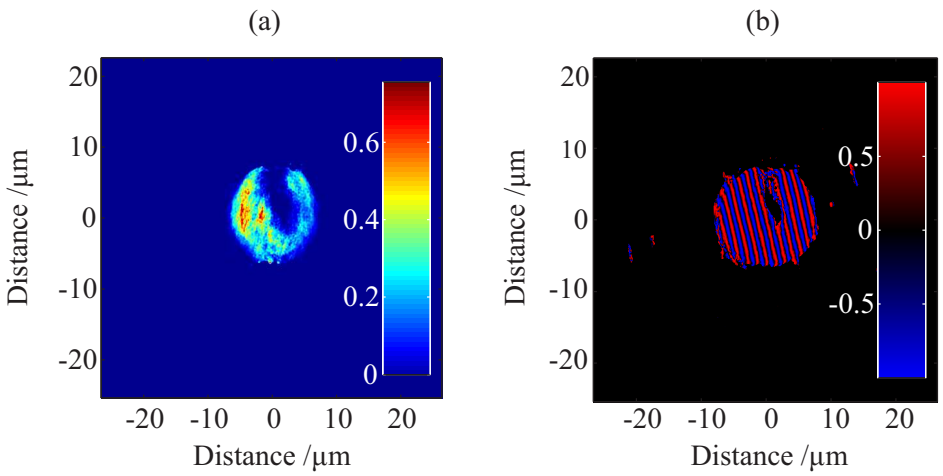

Figure 5.36: Final solution for (a) the intensity and (b) the phase (in radians) displayed in the form cos(φ) in order to illustrate the phase modulations.

Figure 5.37 (a) shows that the final Fourier error eventually gets worse with iteration. This is due to the inability of the algorithm to find a solution. The Fourier error for the final 500 iterations is shown in Fig. 5.37 (b). After an initial drop, the error increases to a plateau where a solution appears to be obtained for the Shrinkwrap cycle.

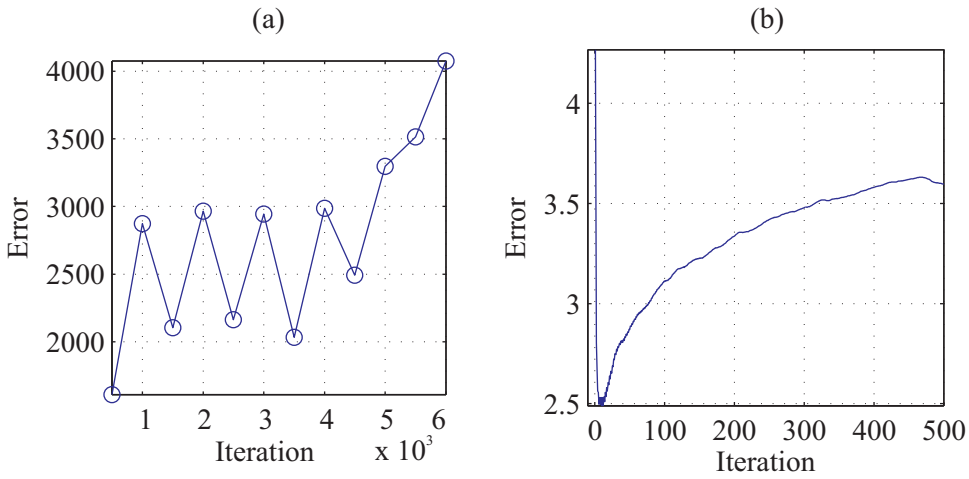

Figure 5.37: (a) Final Fourier error per Shrinkwrap cycle and (b) Fourier error displayed on a $\log_{10}$ scale for the final 500 iterations of reconstruction for the diatom sample. The data are calculated using Equation 5.8.

5.9 Discussion

To increase the resolution of the reconstructed samples, the scattering patterns should be recorded over a longer period of time so that high signal-to-noise is obtained for high spatial frequencies. Since successful imaging of the 5 μm pinhole and ORC FIB sample was achieved with an oversampling ratio of ~ 20, future samples should also have an oversampling ratio of at least this value.

To further improve the image reconstruction, the radiation must be monochromated. This can potentially be done at the XUV source by implementing quasi-phase matching or done after the source by using a mirror with a narrow reflecting bandwidth. In the case of the latter, the XUV beam will reflect off the mirror before being incident on the sample. In addition, the CCD camera needs to be closer to the sample in order to capture higher spatial frequencies and thus enable reconstruction of the object to a higher resolution. This can only be done when using smaller samples so that the oversampling requirement is fulfilled.

With integration times of nearly half an hour when obtaining a scattering pattern from the diatom, work should be done to improve the generated flux to reduce the timescale of the experiments. Although splicing unsaturated images to saturated images proved successful, there are other ways of obtaining scattering patterns containing both high and low spatial frequencies. One option to avoid leaking of the central pixels would be to block the centre of the scattering pattern [23,116].

If the centre of the scattering pattern cannot be placed at the centre of the CCD camera, then a linear phase term could be added to the reconstructed phase. Alternatively, the scattering pattern should be cropped accordingly to avoid reconstruction of phase attributed to the offset of the centre of scattering pattern. However, the drawback of cropping is that it will remove high spatial frequency signal from the scattering pattern and will therefore reduce the resolution of the reconstructed object.

These suggestions will move the project towards its objective of developing a table-top XUV nanoscope.

5.10 Summary

This chapter has demonstrated the imaging of a 5 μm pinhole, a 7.5 μm FIB sample and a biological sample using a table-top XUV nanoscope. The maximum reconstructed object resolution achieved was ~ 300 nm from the ORC FIB sample. Even though generation conditions were changed to decrease the number of harmonics of the source, due to the low oversampling ratio of ~ 10 and the recorded scattering pattern having low signal-to-noise at

high spatial frequencies, the algorithm failed to reconstruct any detail below ~ 500 nm on the diatom.

6 Conclusions and Future Work

This thesis has documented the development of a table-top extreme-ultraviolet (XUV) nanoscope capable of coherent diffractive imaging (CDI), at the Optoelectronics Research Centre.

The structure of an argon gas jet during HHG was determined by focusing a highly intense femtosecond laser into the gas jet and imaging the subsequent fluorescence from excited argon atoms and ions. An increase in XUV yield of ~ 350 % was achieved by using the observed fluorescence to position the laser focus into the Mach disc of the gas jet. The maximum recorded flux from high harmonic generation (HHG) using an argon gas jet is relatively low. As such, in the experimental setup, an argon gas jet was not suitable as a source of XUV radiation for nanoscale imaging.

HHG from an argon-filled pipe has also been demonstrated. Using the observed fluorescence from the argon gas to position the laser focus with respect to the argon-filled pipe, a hundredfold increase in high harmonic flux compared with the gas jet was achieved. Such flux is comparable to that observed from HHG using an argon-filled capillary under similar experimental conditions. Although the phase mismatch was approximately symmetric about the focus for high harmonics generated in this work (H 25 etc.), due to the high absorption and the Cooper minimum present in argon, the position for generating maximum flux and reducing the number of observed harmonics was achieved when the pipe was before the focus. From the results, an argon-filled gas pipe is a potentially viable medium for generating XUV radiation suitable for CDI, due to the algorithmic requirement of a narrow bandwidth.

Using the high harmonics generated from an argon-filled pipe, this thesis has demonstrated the imaging of a 5 μm pinhole, a 7.5 μm FIB sample and a biological sample. The maximum spatial resolution obtained with the table-top XUV nanoscope was ~ 300 nm. Due to the multiwavelength nature of the radiation, the low oversampling ratio and the recorded diatom scattering pattern having a low signal-to-noise at high spatial frequencies, the algorithm failed to reconstruct any detail below 500 nm on the diatom.

The aim of this work was to develop a spatially coherent XUV source and use the radiation for imaging of nanoscale structures. To achieve this, a high flux high harmonic source and an experimental setup suitable for CDI were desired. Generation of XUV

radiation from an argon gas jet and argon-filled pipe was achieved, and successfully imaging of a pinhole, FIB sample and diatom has been demonstrated. However, further research is required to accomplish the ultimate goal of single-shot nanoscale imaging of a whole range of objects and sizes.

Such research should concentrate on increasing the flux and monochromating the radiation. In addition, in order to image nanoscale structures below a size of ~ 20 nm, due to the diffraction limit, the generation of shorter wavelength light needs to be explored [30]. Other research should focus on obtaining high signal-to-noise high spatial frequency scattering patterns without oversaturating the centre of the charge coupled device (CCD) camera. Potential solutions are discussed in the following paragraphs.

An increase in high harmonic flux can be achieved by focusing the fundamental beam with a longer focal length optic and by using larger gas region. By spreading the beams energy over a larger spot size to reduce the peak intensity and ionization contribution to the phase mismatch, the coherence length can be increased. Provided the coherence length and absorption length are longer than the generation medium, the harmonic flux will increase with square of the medium's length and the gas pressure. Takahashi *et al.* [117] achieved a tenfold increase in flux of the 27^{th} harmonic when generating from argon by increasing the focal length and medium length by a factor of ten.

The high harmonic flux at shorter wavelengths can also be increased by using new table-top laser systems with shorter pulses and higher pulse energies [118]. Some of the latest laser systems commercially available can produce < 25 fs pulses with pulse energies of 3.5 mJ at 1 kHz repetition rate. The higher peak pulse intensities will enable higher electron pondermotive energies and thus shorter cut-off wavelengths, while the shorter pulses will reduce the ionization fraction and increase the coherence length.

Generation of shorter wavelengths will also be possible by generating from gases such as neon or helium, which have higher ionization energies than argon. By using a gas which has a higher ionization potential, the cut-off energy of the harmonics will increase since the cut-off energy is the sum of the ionization potential (I_p) and the pondermotive energy of the electron (U_p), $E_{max} = I_p + 3.17U_p$. Hüve *et al.* [119] show that by focusing a highly intense ultrashort pulsed laser into a variety of gases, the highest harmonic generated in argon was 33^{rd} harmonic, while the highest harmonics generated in neon was the 65^{th} harmonic.

An increase in cut-off energy can also be obtained by using a fundamental beam with a longer wavelength since the pondermotive energy (U_p) is proportional to the square of the wavelength of the fundamental laser (λ_0). Colosimo *et al.* [120] document the result of argon atoms ionized by ultrashort pulses with fundamental wavelengths of at 0.8 μm and 2 μm. It was shown that the while the cut-off for a fundamental wavelength of 0.8 μm was 50 eV, the cut-off for a fundamental wavelength of 2 μm was 220 eV.

Narrow-bandwidth multilayer mirrors will enable monochromation of the harmonic source. Generally, single layer mirrors are poor at reflecting XUV radiation at normal incidence. A larger reflectivity by a mirror can be accomplished by using multiple layers of alternating materials so that the reflected waves will interfere constructively. A reflectivity of 70.5 % at 13.3 nm and 70.15 % at 13.5 nm has been demonstrated experimentally using molybdenum/silicon layers [121]. CDI using narrow-bandwidth multilayer mirrors to monochromate the radiation from a HHG source has been shown to produce images with a resolution of 94 nm [23].

A suitable method of blocking intense low spatial frequencies will allow long exposures to obtain high spatial frequency scattering patterns with high signal-to-noise. Indeed, Sandberg *et al.* [110] demonstrated CDI with the aid of circular beam blocks of different sizes placed at the centre of the scattering pattern. These blocks were supported by a thin wire. Large beam blocks were used for long exposures in order to record scattering patterns with high spatial frequencies, while small beam blocks were used to acquire scattering patterns with low spatial frequencies. The scattering patterns were spliced together to increase the dynamic range of the CCD camera images by 8 orders of magnitude.

Although the technology is still in its infancy, the development of a table-top nanoscope that will enable routine imaging of nanostructures may well become as beneficial to science as the invention of optical microscope.

A XUV Spectrometer

A.1 Introduction

This appendix provides details of the optical design and wavelength calibration of the XUV spectrometer introduced in Chapter 2 and used in experiments documented in this thesis. The XUV spectrometer is a Rowland circle grazing incidence spectrometer and is manufactured by Schulz Scientific Instruments (LPS-VUV-NG1).

A.2 Optical Design

The optical design of the XUV spectrometer is illustrated in Fig. A.1. The XUV beam passes through a 100 μm entrance slit and is incident on a concave gold grating placed on the tangent of a circle, known as a Rowland circle, which has a radius that is half the radius of curvature of the grating. In this way, the grating disperses the XUV beam across a curved microchannel plate (MCP) detector positioned along the circle [122].

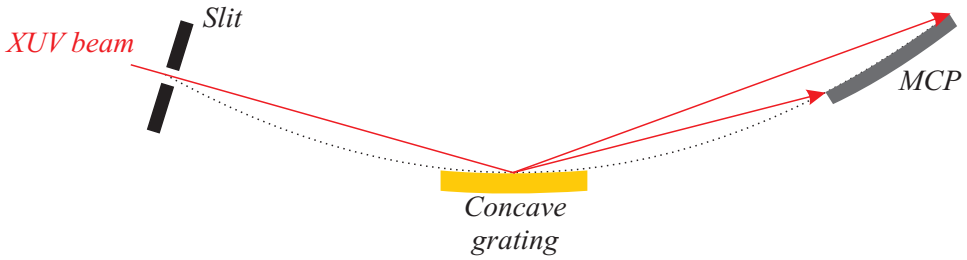

Figure A.1: Rowland circle grazing incidence XUV spectrometer. The dashed line indicates the Rowland circle.

Because the MCP is curved along the Rowland circle, a linear wavelength calibration and sharp spectral lines are produced on its face. The MCP consists of an array of 12 μm channels that produce a cascade of electrons when XUV photons are incident on them. These electrons cascade within the channels and are then accelerated by a potential difference of > 1 kV that is applied across the plate. The amplified electrons are then imaged

onto a phosphor plate to produce visible light which is imaged using a CCD camera (Pixis 400).

A.3 Wavelength Calibration

The wavelengths are calculated from the positions of the spectral lines on the Rowland circle,

$$\lambda = \frac{10^7}{N}\left[\sin\alpha - \cos\left(\frac{x}{\rho}\right)\right] \tag{A.1}$$

where λ is the wavelength of the spectral line, N is the grating ruling (grooves per mm), α is the angle of incidence, ρ is the radius of curvature of the grating and x is the length of the arc between the centre of the grating and the position of the harmonic along the Rowland circle [123].

Since it is not possible to measure x directly, only the relative positions of spectral lines can be measured. For work in this thesis, calibration of the spectrum was performed numerically. Since the wavelength separation between harmonics exists in a unique ratio, by measuring these ratios, the harmonic wavelengths can be determined. If the theoretical position x of each harmonic on the detector is calculated using Equation A.1 and a least squares fit is performed between the measured positions, it is possible to determine the harmonic sequence of the radiation that the data represents. The technique is performed on spectra that are acquired at low intensities and pressures so that the harmonic centre wavelength is well defined and there is no blue-shifting of the harmonics caused by ionization. This technique has been successfully cross-correlated with helium emission on the spectrometer in work done by Froud [124].

B Papers, Talks and Posters

- J. Grant-Jacob, B. Mills, T. J. Butcher, R. T. Chapman, W. S. Brocklesby and J. G. Frey. *Gas jet structure influence on high harmonic generation.* Optics Express, **19**, 9801-9806 (2011).

- J. Grant-Jacob, B. Mills, T. J. Butcher, R. T. Chapman, W. S. Brocklesby and J. G. Frey. *Imaging an Argon Gas Jet Using a Femtosecond Laser.* (Paper in preparation).

- J. Grant-Jacob, B. Mills, T. J. Butcher, R. T. Chapman, W. S. Brocklesby, J. G. Frey. *Influence of gas jet structure on high harmonic generation.* Photon 10, University of Southampton, 23-26 Aug 2010 (Talk).

- J. Grant-Jacob, B. Mills, T. J. Butcher, R. T. Chapman, W. S. Brocklesby, J. G. Frey. *Investigating an Argon Gas Jet Using a Femtosecond Laser.* Southern Universities Graduate Symposium on Spectroscopy and Dynamics, University of Oxford, 4 June 2009 (Talk).

- J. Grant-Jacob, B. Mills, T. J. Butcher, R. T. Chapman, W. S. Brocklesby, J. G. Frey. *Gas jet structure influence on high harmonic generation.* Photonics 09, University of Southampton, 15 Dec 2009 (Poster).

Bibliography

1. Ash, E. A. & Nicholls, G., Super-resolution Aperture Scanning Microscope. *Nature* **237**, 510-512 (1972).

2. Hell, S. W., Dyba, M. & Jakobs, S., Concepts for nanoscale resolution in fluorescence microscopy. *Current Opinion in Neurobiology* **14**, 599-609 (2004).

3. Betzig, E., Patterson, G. H., Sougrat, R., Lindwasser, O. W., Olenych, S., Bonifacino, J. S., Davidson, M. W., Lippincott-Schwartz, J. & Hess, H. F., Imaging Intracellular Fluorescent Proteins at Nanometer Resolution. *Science* **313**, 1642-1645 (2006).

4. Goodhew, P. J., Humphreys, F. J. & Beanland, R., *Electron microscopy and analysis* (Taylor & Francis, London, 2001).

5. Morgan, J., Notte, J., Hill, R. & Ward, B., An Introduction to the Helium Ion Microscope. *Microscopy Today* **14**, 24-31 (2006).

6. Binnig, G., Rohrer, H., Gerber, C. & Weibel, E., Surface Studies by Scanning Tunneling Microscopy. *Physical Review Letters* **49**, 57-61 (1982).

7. Binnig, G., Quate, C. F. & Gerber, C., Atomic Force Microscope. *Physical Review Letters* **56**, 930-933 (1986).

8. Bragg, W. L., The Structure of Some Crystals as Indicated by Their Diffraction of X-rays. *Proceedings of the Royal Society of London. Series A, Containing Papers of a Mathematical and Physical Character* **89**, 248-277 (1913).

9. Dauter, Z., Current state and prospects of macromolecular crystallography. *Acta Crystallographica D* **62**, 1-11 (2006).

10. Myers, H. P., *Introductory solid state physics* (Taylor & Francis, London, 1989).

11. Pusey, M. L., Liu, Z. J., Tempel, W., Praissman, J., Lin, D., Wang, B. C., Gavira, J. A. & Ng, J. D., Life in the fast lane for protein crystallization and X-ray crystallography. *Progress in Biophysics and Molecular Biology* **88**, 359-386 (2005).

12. Sayre, D. & Chapman, H. N., X-ray microscopy. *Acta Crystallographica* **51**, 237-252 (1995).

13. Chao, W., Harteneck, B. D., Liddle, J. A., Anderson, E. H. & Attwood, D. T., Soft X-ray microscopy at a spatial resolution better than 15 nm. *Nature* **435**, 1210-1213 (2005).

14. Howells, M. R., Beetz, T., Chapman, H. N., Cui, C., Holton, J. M., Jacobsen, C. J., Kirz, J., Lima, E., Marchesini, S., Miao, H., Sayre, D., Shapiro, D. A., Spence, J. C. H. & Starodub, D., An assessment of the resolution limitation due to radiation-damage in X-ray diffraction microscopy. *Journal of Electron Spectroscopy and Related Phenomena* **170**, 4-12 (2009).

15. Neutze, R., Wouts, R., van der Spoel, D., Weckert, E. & Hajdu, J., Potential for biomolecular imaging with femtosecond X-ray pulses. *Nature* **406**, 752-757 (2000).

16. Chapman, H. N., Barty, A., Bogan, M. J., Boutet, S., Frank, M., Hau-Riege, S. P., Marchesini, S., Woods, B. W., Bajt, S., Benner, W. H., London, R. A., Plönjes, E., Kuhlmann, M., Treusch, R., Düsterer, S., Tschentscher, T., Schneider, J. R., Spiller, E., Möller, T., Bostedt, C., Hoener, M., Shapiro, D. A., Hodgson, K. O., van der Spoel, D., Burmeister, F., Bergh, M., Caleman, C., Huldt, G., Seibert, M. M., Maia, F. R. N. C., Lee, R. W., Szöke, A., Timneanu, N. & Hajdu, J., Femtosecond diffractive imaging with a soft-X-ray free-electron laser. *Nature Physics* **2**, 839-843 (2006).

17. Henke, B. L., Gullikson, E. M. & Davis, J. C., X-ray interactions - photoabsorption, scattering, transmission, and reflection at E=50-30000 eV, Z=1-92. *Atomic Data and Nuclear Data Tables* **54**, 181-342 (1993).

18. Barty, A., Boutet, S., Bogan, M. J., Hau-Riege, S., Marchesini, K., Sokolowski-Tinten, S., Stojanovic, N., Tobey, R., Ehrke, H., Cavlleri, A., Dustere, S., Frank, M., Bajt, S., Woods, B. W., Seibert, M. M., Hadju, J., Treusch, R. & Chapman, H. N., Ultrafast single-shot diffraction imaging of nano-scale dynamics. *Nature Photonics* **2**, 415-419 (2008).

19. Gerchberg, R. W. & Saxton, W. O., A practical algorithm for the determination of phase from image and diffraction plane pictures. *Optik* **35**, 237-246 (1972).

20. Fienup, J. R., Phase retrieval algorithms: a comparison. *Applied Optics* **21**, 2752-2769 (1982).

21. Key, M. H., Laboratory production of X-ray lasers. *Nature* **316**, 314-319 (1985).

22. Rocca, J. J., Shlyaptsev, V., Tomasel, F. G., Cortazar, O. D., Hartshorn, D. & Chilla, J. L., Demonstration of a discharge pumped table-top soft x-ray laser. *Physical Review Letters* **73**, 2192-2195 (1994).

23. Sandberg, R. L., Song, C., Wachulak, P. W., Raymondson, D. A., Paul, A., Amirbekian, B., Lee, E., Sakdinawat, A. E., La-O-Vorakiat, C., Marconi, M. C., Menoni, C. S., Murnane, M. M., Rocca, J. J., Kapteyn, H. C. & Miao, J., High numerical aperture tabletop soft x-ray diffraction microscopy with 70-nm resolution. *Proceedings of the National Academy of Sciences* **105**, 24-27 (2008).

24. Bilderback, D. H., Elleaumme, P. & Weckert, E., Review of third and next generation synchrotron light sources. *Journal of Physics B* **38**, 773-797 (2005).

25. Schoenlein, R. W., Chattopadhyay, S., Chong, H. H. W., Glover, T. E., Heimann, P. A., Shank, C. V., Zholents, A. A. & Zolotorev, M. S., Generation of femtosecond pulses of synchrotron radiation. *Science* **287**, 2237-2240 (2000).

26. Grimes, J. M., Burroughs, J. N., Gouet, P., Diprose, M., Malby, R., Zientara, S., Mertens, P. C. & Stuart, D. I., The atomic structure of the bluetongue virus core. *Nature* **395**, 470-478 (1998).

27. FLASH Web site, Available at http://flash.desy.de/ (2010).

28. Emma, P., Akre, R., Arthur, J., Bionta, R., Bostedt, C., Bozek, J., Brachmann, A., Bucksbaum, P., Coffee, R., Decker, F. J., Ding, Y., Dowell, D., Edstrom, S., Fisher, A., Frisch, J., Gilvech, S., Hastings, J., Hays, G., Hering, P., Huang, Z., Iverson, R., Loos, H., Messerschmidt, M., Miahnahri, A., Moeller, S., Nuhn, H. D., Pile, G., Ratner, D., Rzepiela, J., Schultz, D., Smith, T., Stefan, P., Tompkins, H., Tuner, J., Welch, J., White, W., Wu, J., Yocky, G. & Galayda, J., First lasing and operation of an ångstrom-wavelength free-electron laser. *Nature Photonics* **4**, 641-647 (2010).

29. Diamond Light Source Web site, Available at http://www.diamond.ac.uk/ (2010).

30. Spielmann, C., Burnett, N. H., Sartania, S., Koppitsch, R., Schnürer, M., Kan, C., Lenzner, M., Wobrauschek, P. & Krausz, F., Generation of coherent x-rays in the water window using 5-femtosecond laser pulses. *Science* **278**, 661-664 (1997).

31. Gibson, E. A., Paul, A., Wagner, N., Tobey, R., Backus, S., Christov, I. P., Murnane, M. M. & Kapteyn, H. C., High-order harmonic generation up to 250 ev from highly ionized argon. *Physical Review Letters* **92**, 033001 (2004).

32. Froud, C. A., Rogers, E. T. F., Praeger, M., Hanna, D. C., Brocklesby, W. S., de Paula, A. M., Baumberg, J. J. & Frey, J. G., Soft x-ray wavelength shift induced by ionization effects in a capillary. *Optics Letters* **313**, 374-376 (2006).

33. Zhang, X., Lytle, A. L., Popmintchev, T., Zhou, X., Kapteyn, H. C., Murnane, M. M. & Cohen, O., Quasi-phase-matching and quantum-path control of high-harmonic generation using counterpropagating light. *Nature Physics* **3**, 270-275 (2007).

34. Corkum, P. B., Plasma perspective on strong-field multiphoton ionisation. *Physical Review Letters* **71**, 1994-1997 (1993).

35. Lewenstein, M., Balcou, P., Ivanov, M. & Yu, L., Theory of high-harmonic generation by low frequency laser fields. *Physical Review A* **49**, 2117-2132 (1994).

36. Corkum, P. B. & Krauz, F., Attosecond Sceince. *Nature Physics* **3**, 381-387 (2007).

37. Lynga, C., Gaarde, M. B., Delfin, C., Bellini, M., Hansch, T. W., L'Huillier, A. L. & Wahlström, C. G., Temporal coherence of high-order harmonics. *Physical Review A* **60**, 4823-4830 (1999).

38. Paulus, G. G., Becker, W. & Walther, H., Classical rescattering effects in two-color above-threshold ionization. *Physical Review A* **52**, 4043-4053 (1995).

39. Lindner, F., Stremme, W., Schatzel, M. G., Grasbon, F., Paulus, G. G., Walther, H., Hartmann, R. & Struder, L., High-order harmonic generation at a repetition rate of 100 kHz. *Physical Review A* **68**, 013814 (2003).

40. Li, X. F., L'Huillier, A., Ferray, M., Lompre, L. A. & Mainfray, G., Multiple-harmonic generation in rare gases at high laser intensity. *Physical Review A* **39**, 5751-5761 (1989).

41. Krause, J. L., Schafer, K. J. & Kulander, K. C., High-order harmonic generation from atoms and ions in the high intensity regime. *Physical Review Letters* **68**, 3535-3538 (1992).

42. L'Huillier, A. & Balcou, P., High-Order Harmonic Generation in Rare Gases with a 1-ps 1053-nm Laser. *Physical Review Letters* **70**, 774-777 (1993).

43. Ferray, M., L'Huillier, A., Li, X. F., Lompre, L. A., Mainfray, G. & Manus, C., Multiple-harmonic conversion of 1064 nm radiation in rare gases. *Journal of Physics B: Atomic, Molecular and Optical Physics* **21**, 31-35 (1988).

44. Pfeifer, T., Spielmann, C. & Gerber, G., Femtosecond X-ray science. *Reports on Progress in Physics* **69**, 443-505 (2006).

45. Salières, P., L'Huillier, A. & Lewenstein, M., Coherence control of high-order Harmonics. *Physical Review Letters* **74**, 3776-3779 (1995).

46. Ganeev, R. A., High-order harmonic generation in a laser plasma: a review of recent achievements. *Journal of Physics B: Atomic, Molecular and Optical Physics* **40**, 213-253 (2007).

47. Chang, Z. H., Rundquist, A., Wang, H. W., Christov, I., Murnane, M. M. & Kapteyn, H. C., Generation of coherent, femtosecond, Xray pulses in the "water window". *IEEE Journal of Selected Topics in Quantum Electronics* **4**, 266-270 (1998).

48. Gaudiosi, D., Reagan, B., Popmintchev, T., Grisham, M., Berrill, M., Cohen, O., Walker, B. C., Murnane, M. M., Kapteyn, H. C. & Rocca, J. J., High-order harmonic generation from ions in a capillary discharge. *Physical Review Letters* **96**, 203001 (2006).

49. Seres, J., Wobrauschek, P., Streli, C., Yakvlev, V. S., Seres, E., Krausz, F. & Spielmann, C., Generation of coherent keV X-rays with intense femtosecond laser pulses. *New Journal of Physics* **8**, 251 (2006).

50. Popmintchev, T., Chen, M., Arpin, P., Gerrity, M., Seaberg, M., Zhang, B., Popmintchev, D., Andriukaitis, G., Balciunas, T., Mücke, O., Pugzlys, A., Baltuska, A., Murnane, M. & Kapteyn, H., *Bright Coherent Ultrafast X-rays from mid-IR Lasers*, presented at OSA Technical Digest, Turkey, (2011).

51. L'Huillier, A., Lewenstein, M., Salières, P., Balcou, P., Ivanov, M. Y., Larsson, J. & Wahlström, C. G., High-order harmonic-generation cutoff. *Physical Review A* **48**, R3433-R3436 (1993).

52. Zaïr, A., Holler, M., Guandalini, A., Schapper, F., Biegert, J., Gallmann, L., Keller, U., Wyatt, A. S., Monmayrant, A., Walmsley, I. A., Cormier, E., Auguste, T., Caumes, J. P. & Salières, P., Quantum Path Interferences in High-Order Harmonic Generation. *Physical Review Letters* **100**, 143902 (2008).

53. Bransden, B. H. & Joachain, C. J., *Physics of Atoms and Molecules* (Prentice Hall, Harlow, 2003).

54. Keldysh, L. V., Ionization in the field of a strong electromagnetic wave. *Soviet Physics*

JETP **20**, 1307-1314 (1965).

55. Popov, V. S., Tunnel and multiphoton ionization of atoms and ions in a strong laser field (Keldysh theory). *Physics - Uspekhi* **47**, 855-885 (2004).

56. Radzig, A. A. & Smirnov, B. M., *Reference Data on Atoms, Molecules, and Ions* (Springer-Verlag, Berlin, 1985).

57. Rundquist, A., Durfee III, C. G., Chang, Z., Herne, C., Backus, S., Murnane, M. M. & Kapteyn, H. C., Phase-Matched Generation of Coherent Soft X-rays. *Science* **280**, 1412-1415 (1998).

58. Lewenstein, M., Salières, P. & L'Huillier, A., Phase of the atomic polarization in high-order harmonic generation. *Physical Review A* **52**, 4747-4754 (1995).

59. Balcou, P., Salières, P., L'Huillier, A. & Lewenstein, M., Generalized phase-matching conditions for high harmonics: The role of field-gradient forces. *Physical Review A* **55**, 3204-3210 (1997).

60. Durfee III, C. G., Rundquist, A. R., Backus, S., Herne, C., Murnane, M. M. & Kapteyn, H. C., Phase Matching of High-Order Harmonics in Hollow Waveguides. *Physical Review Letters* **83**, 2187-2190 (1999).

61. Dalgarno, A. & Kingston, A. E., *The refractive indices and Verdet constants of the inert gases*, presented at Proceedings of the Royal Society of London, Series A, Mathematical and Physical Sciences, (1960).

62. Brabec, T. & Krausz, F., Intense few-cycle laser fields: Frontiers of nonlinear optics. *Reviews of Modern Physics* **72**, 545-591 (2000).

63. Armstrong, J. A., Bloembergen, N., Ducuing, J. & Pershan, P. S., Interactions between Light Waves in a Nonlinear Dielectric. *Physical Review* **127**, 1918-1939 (1962).

64. Gibson, E. A., Paul, A., Wagner, N., Tobey, R., Gaudiosi, D., Backus, S., Christov, I. P., Aquila, A., Gullikson, E. M., Attwood, D. T., Murnane, M. M. & Kapteyn, H. C., Coherent Soft X-ray Generation in the Water Window with Quasi-Phase Matching. *Science* **302**, 95-98 (2003).

65. Auguste, T., Carré, B. & Salières, P., Quasi-phase-matching of high-order harmonics using a modulated atomic density. *Physical Review A* **76**, 011802 (2007).

66. Shkolnikov, P. L., Lago, A. & Kaplan, A. E., Optimal quasi-phase-matching for high-

order harmonic generation in gases and plasmas. *Physical Review A*, 4461-4464 (1994).

67. Seres, J., Yakovlev, V. S., Seres, E., Streli, C. H., Spielmann, C. H. & Krausz, F., Coherent superposition of laser-driven soft-X-ray harmonics from successive sources. *Nature Physics* **3**, 878-883 (2007).

68. Pirri, A., Corsi, C. & Bellini, M., Enhancing the yield of high-order harmonics with an array of gas jets. *Physical Review A* **78**, 011801 (2008).

69. L'Huillier, A., Schafer, K. J. & Kulander, K. C., Higher-order harmonic generation in xenon at 1064 nm: The role of phase matching. *Physical Review Letters* **66**, 2200-2203 (1991).

70. Constant, E., Garzella, D., Breger, P., Mevel, E., Dorrer, C. & Le Blanc, C., Optimizing High Harmonic Generation in Absorbing Gases: Model and Experiment. *Physical Review Letters* **82**, 1668-1671 (1999).

71. Backus, S., Durfee III, C. G., Murnane, M. M. & Kapteyn, H. C., High power ultrafast lasers. *Review of Scientific Instruments* **69**, 1207-1223 (1998).

72. Spence, D. E., Kean, P. N. & Sibbett, W., 60-fsec pulse generation from a self-mode-locked Ti:sapphire laser. *Optics Letters* **16**, 42-44 (1991).

73. Brabec, T., Spielmann, C., Curley, P. F. & Krausz, F., Kerr lens mode locking. *Optics Letters* **17**, 1292-1294 (1992).

74. Kmetec, J. D., Macklin, J. J. & Young, J. E., 0.5-TW, 125-fs Ti:sapphire laser. *Optics Letters* **16**, 1001-1003 (1991).

75. Kane, D. & Trebino, R., Characterization of arbitrary femtosecond pulses using frequency-resolved optical gating. *IEEE Journal of Quantum Electronics* **29**, 571-579 (1993).

76. O'Shea, P., Kimmel, M., Gu, X. & Trebino, R., Highly simplified device for ultrashort-pulse measurement. *Optics Letters* **26**, 932-934 (2001).

77. Siegman, A. E., Defining, measuring, and optimizing laser beam quality. *Proceedings of SPIE* **1868**, 2-12 (1993).

78. Siegman, A., *How to (Maybe) Measure Laser Beam Quality*, presented at Optical Society of America Annual Meeting, California, (1997).

79. Butcher, T. J. (Manuscript in preparation).

80. Ashkenas, H. & Sherman, F. S., Structure and utilization of supersonic free jets in low desnity wind tunnels. *Rarefied Gas Dynamics* **2**, 1-28 (1965).

81. Pauly, H., *Atom, Molecule, and Cluster Beams I* (Springer, Berlin, 2003).

82. Creasey, D. J., Heard, D. E., Pilling, M. J., Whitaker, B. J., Berzins, M. & Fairlie, R., Visualisation of a supersonic free-jet expansion using laser-induced fluorescence spectroscopy: Application to the measurement of rate constants at ultralow temperatures. *Applied Physics B* **65**, 375-391 (1997).

83. van de Sanden, M. C. M., de Regt, J. M. & Schram, D. C., Recombination of argon in an expanding plasma jet. *Physical Review E* **47**, 2792-2797 (1992).

84. Tejeda, G., Maté, B., Fernández-Sánchez, J. M. & Montero, S., Temperature and Density Mapping of Supersonic Jet Expansions Using Linear Raman Spectroscopy. *Physical Review Letters* **76**, 34-37 (1996).

85. Adamson, T. C. & Nicholls, J. A., On the Structure of Jets From Highly Underexpanded Nozzles Into Still Air. *Journal of Aerospace Science* **26**, 16-24 (1959).

86. Scoles, G., *Atomic and Molecular Beam Methods VI* (Oxford University Press, New York, 1992).

87. Statz, H., Horrigan, F. A., Koozekanani, S. H., Tang, C. L. & Koster, G. F., Transition Probabilities for some Ar II Laser Lines. *Journal of Applied Physics* **36**, 2278-2286 (1965).

88. Penning, F. M., Über Ionisation durch metastabile Atome. *Die Naturwissenschaften* **15**, 818 (1927).

89. Arimondo, E., Clark, C. W. & Martin, W. C., Colloquium: Ettore Majorana and the birth of autoionization. *Review of Modern Physics* **82**, 1947-1958 (2010).

90. Hirakawa, Y., Nagai, A., Tatsuo, O., Maeda, M. & Muraoka, K., Absolute Density Measurement of a Pulsed H_2 Gas Jet Used for Extreme Ultraviolet Generation by Nonlinear Frequency Conversion. *Japanese Journal of Applied Physics* **33**, 183-185 (1994).

91. Cooper, J. W., Photoionization from Outer Atomic Subshells. A Model Study. *Physical Review* **128**, 681-693 (1962).

92. McFarland, B., Farrell, J., Guehr, M. & Bucksbaum, P., *High Harmonic Spectral*

Minimum and Phase in Argon and Nitrogen, presented at OSA Technical Digest, California, (2008).

93. Wörner, H. K., Niikura, H., Bertrand, J. B., Corkum, P. B. & Villeneuve, D. M., Observation of Electronic Structure Minima in High-Harmonic Generation. *Physical Review Letters* **102**, 103901 (2009).

94. Sakdinawat, A. & Attwood, D., Nanoscale X-ray imaging. *Nature Photonics* **4**, 840-848 (2010).

95. Mashiko, H., Suda, A. & Midorikawa, K., Focusing coherent soft-x-ray radiation to a micrometer spot size with an intensity of 10^{14} W/cm^2. *Optics Letters* **29**, 1927-1929 (2004).

96. Balcou, P. & L'Huillier, A., Phase-matching effects in strong-field harmonic generation. *Physical Review A* **47**, 1447-1459 (1993).

97. Bellini, M., Lyngå, C., Tozzi, A., Gaarde, M. B., Hänsch, T. W., L'Huillier, A. & Wahlström, C.-G., Temporal Coherence of Ultrashort High-Order Harmonic Pulses. *Physical Review Letters* **81**, 297-300 (1998).

98. Gaarde, M. B., Salin, F., Constant, E., Balcou, P., Schafer, K. J., Kulander, K. C. & L'Huillier, A., Spatiotemporal separation of high harmonic radiation into two quantum path components. *Physical Review A* **59**, 1367-1373 (1999).

99. Chiron, A., Lamouroux, B., Lange, R., Ripoche, J.-F., Franco, M. P. B., Bonnaud, G., Riazuelo, G. & Mysyrowicz, A., Numerical simulations of the nonlinear propagation of femtosecond optical pulses in gases. *The European Physical Journal D* **6**, 383-396 (1999).

100. Gidalevich, E., Boxman, R. L. & Goldsmith, S., Theory and modelling of the interaction of two parallel supersonic plasma jets. *Journal of Physics D: Applied Physics* **31**, 304-311 (1998).

101. Fritsching, U., *Spray Simulation* (Cambridge University Press, Cambridge, 2004).

102. Kinsler, L. E., *Fundamentals of Acoustics* (Wiley, New York, 1982).

103. Bond, L. J., Chiani, C.-H., Fortunko, C. M. & McColskey, J. D., *Absorption of sound in gases between 10 and 25 MHz: argon*, presented at Ultrasonics Symposium, 1991. Proceedings., IEEE 1991, Orlando, (1991).

104. Chen, B., Dilanian, R. A., Teichmann, S., Abbey, B., Peele, A. G., Williams, G. J., Hannaford, P., Dao, L. V., Quiney, H. M. & Nugent, K. A., Multiple wavelength diffractive imaging. *Physics Review A* **79**, 023809 (2009).

105. Bartels, R. A., Paul, A., Murnane, M. M., Kapteyn, H. C., Backus, S., Liu, Y. & Attwood, D. T., Absolute determination of the wavelength and spectrum of an extreme-ultraviolet beam by a young's double-slit measurement. *Optics Letters* **27**, 707-709 (2002).

106. Siegman, A. E., *Lasers* (University Science Books, United States of America, 1986).

107. Mills, B., *Focussing and Diffraction using a High Harmonic Source*. PhD Thesis, University of Southampton (2009).

108. Marchesini, S., He, H., Chapman, H. N., Hau-Riege, S. P., Noy, A., Howells, M. R., Weierstall, U. & Spence, J. C. H., X-ray image reconstruction from a diffraction pattern alone. *Physical Review B* **68**, 140101 (2003).

109. Miao, J., Ishikawa, T., Anderson, E. H. & Hodgson, K. O., Phase retrieval of diffraction patterns from noncrystalline samples using the oversampling method. *Physical Review B* **67**, 174104 (2003).

110. Sandberg, R. L., Paul, A., Raymondson, D. A., Hadrich, S., Gaudiosi, D. M., Holtsnider, J., Tobey, R. I., Cohen, O., Murnane, M. M. & Kapteyn, H. C., Lensless diffractive imaging using tabletop coherent high harmonic soft-x-ray beams. *Physical Review Letters* **99**, 098103 (2007).

111. Chapman, H. N., Barty, A., Marchesini, S., Noy, A., Hau-Riege, S. P., Cui, C., Howells, M. R., Rosen, R., He, H., Spence, J. C. H., Weierstall, U., Beetz, T., Jacobsen, C. & Shapiro, D., High-resolution ab initio three-dimensional x-ray diffraction microscopy. *Journal of the Optical Society of America A* **23**, 1179-1200 (2006).

112. Tong, H. D., Jansen, H. V., Gadgil, V. J., Bostan, C. G., Berenschot, E., Rijn, C. J. M. & Elwenspoek, M., Silicon nitride nanosieve membrane. *Nano* **4**, 283-287 (2004).

113. Round, F. E., Crawford, R. M. & Mann, D. G., *Diatoms: Biology and Morphology of the Genera* (Cambridge University Press, Cambridge, 1990).

114. Fuhrmann, T., Landwehr, S., El Rharbi-Kucki, M. & Sumper, M., Diatoms as living photonic crystals. *Applied Physics B* **78**, 257-260 (2004).

115. Gordon, R., Losic, D., Tiffany, M. A., Nagy, S. S. & Sterrenburg, F. A. S., The Glass

Menagerie: diatoms for novel applications in nanotechnology. *Trends in Biotechnology* **27**, 116-127 (2009).

116. Barty, A., Marchesini, S., Chapman, H. N., Cui, C., Howells, M. R., Shapiro, D. A., Minor, A. M., Spence, J. C. H., Weierstall, U., Ilavsky, J., Noy, A., Hau-Riege, S. P., Artyukhin, A. B., Baumann, T., Willey, T., Stolken, J., van Buuren, T. & Kinney, J. H., Three-Dimensional Coherent X-Ray Diffraction Imaging of a Ceramic Nanofoam: Determination of Structural Deformation Mechanisms. *Physical Review Letters* **101**, 055501 (2008).

117. Takahashi, E., Nabekawa, Y., Nurhuda, M. & Midorikawa, K., Generation of high-energy high-order harmonics by use of a long interaction medium. *Journal Optical Society America B* **20**, 158-165 (2003).

118. Coherent inc. Web site, Available at http://www.coherent.com/ (2010).

119. Hüve, J., Haarlammerta, T., Steinbrücka, T., Kutznera, J., Tsilimisa, G. & Zachariasa, H., High-flux high harmonic soft X-ray generation up to 10 kHz repetition rate. *Optics Communications* **266**, 261-265 (2006).

120. Colosimo, P. D. G., Blaga, C. I., Wheeler, J., Hauri, C., Catoire, F., Tate, J., Chirla, R., March, A. M., Paulus, G. G., Muller, H. G., Agostini, P. & DiMauro, L. F., Scaling strong-field interactions towards the classical limit. *Nature Physics* **4**, 386-389 (2008).

121. Yakshin, A. E., van de Kruijs, R. W. E., Nedelcu, I., Zoethout, E., Louis, E., Bijkerk, F., Enkisch, H. & Müllender, S., Enhanced reflectance of interface engineered Mo/Si multilayers produced by thermal particle deposition. *SPIE* **6517**, 65170I (2007).

122. Namioka, T., Theory of the concave grating. *Journal of the Optical Society of America* **49**, 446-460 (1959).

123. Samson., J. A. R., *Techniques of XUV spectroscopy* (Wiley and Sons, New York, 1967).

124. Froud, C. A., *Designing a Nanoscale Source: Towards Single Molecule X-Ray Scattering*. PhD Thesis, University of Southampton (2007).